Engineering Journal

Third Quarter 2019 | Volume 56, No. 3

Smarter. Stronger. Steel.

Engineering Journal

American Institute of Steel Construction

Dedicated to the development and improvement of steel construction, through the interchange of ideas, experiences and data.

Engineering Journal (ISSN 0013-8029) is published quarterly. Subscriptions: Members: one subscription, $40 per year, included in dues; Additional Member Subscriptions: $40 per year. Non-Members U.S.: $160 per year. Foreign (Canada and Mexico): Members $80 per year. Non-Members $160 per year. Published by the American Institute of Steel Construction at 130 E Randolph Street, Suite 2000, Chicago, IL 60601.

Periodicals postage paid at Chicago, IL and additional mailing offices. **Postmaster:** Send address changes to *Engineering Journal* in care of the American Institute of Steel Construction, 130 E Randolph Street, Suite 2000, Chicago, IL 60601.

Subscriptions: subscriptions@aisc.org, 312.670.2400

Archives: Search at **aisc.org/ej**. Article downloads are free for current members and are avaialable for a nominal fee for non-members.

Design for Gusset Plate Buckling with Variable Stress Trajectories

BO DOWSWELL

ABSTRACT

Gusset plates are used in steel buildings and bridges to connect diagonal members to other framing members in the structural system. Gusset plates subjected to compression loads are currently modeled as rectangular columns with an effective cross section defined by a 30° stress trajectory known as the Whitmore section. The buckling strength is calculated using the AISC column curve with empirical effective length factors. Previous research has shown local yielding allows the stresses to redistribute, increasing the effective width. Because the inelastic capacity decreases with gusset slenderness, a variable stress trajectory has been established which is dependent on the flexural buckling slenderness parameter. This paper describes a design method for the buckling strength of gusset plates using variable stress trajectory angles. The proposed effective length factors for the equivalent column were evaluated using data from existing research. The design model is valid for single- and double-plane corner gusset plates, including extended corner gusset plates commonly used for seismic design. Compared to the results of 162 specimens from 12 previously published research projects, the proposed design model is shown to be more accurate than the methods that are currently available.

Keywords: Gusset plate buckling, stress trajectory, AISC column curve.

INTRODUCTION

Figure 1(a) shows a typical vertical brace connection at a beam-to-column intersection, also known as a corner gusset plate connection. The gusset plate transfers axial load from the brace and distributes it to the beam and column. Figure 1(b) shows a double-plane truss connection that transfers axial load from the diagonal web member to the chord and the vertical web member. Double-plane gusset plates are commonly used to connect wide-flange truss members in long-span trusses. This configuration uses two side-by-side gussets connecting to each flange of the web and chord members.

In practice, gusset plates are treated as rectangular, axially loaded members with a cross section $L_w \times t$, where L_w is the effective width and t is the gusset plate thickness. The effective width is generally calculated with a constant 30° trajectory angle, as shown in Figure 2(a), which was based on the experimental stress trajectories in elastic gusset plates. In this case, the equivalent cross section is known as the Whitmore section (Whitmore, 1952).

Based on a proposal by Thornton (1984), gusset plates in compression are currently designed as rectangular columns with a cross section defined by the Whitmore section. The buckling strength is calculated with the column curve in AISC *Specification* Section E3 (AISC, 2016). For corner gusset plates, the column length, l_{avg}, is the average of l_1, l_2, and l_3 as shown in Figure 2(b).

AISC *Specification* Section E3 for flexural buckling was developed for designing main structural members with various cross-sectional shapes and residual stress patterns. Because connection elements have lower residual stresses and higher shape factors than main members, the buckling strength in the inelastic range is higher than predicted by the AISC *Specification* equations (Dowswell, 2016). To account for this behavior at low slenderness ratios in AISC *Specification* Section J4.4, the critical stress is equal to the specified minimum yield strength when the slenderness ratio is equal to or less than 25.

Effective lengths, $L_c = KL$, have been developed for several common gusset plate geometries. In most cases, the effective length recommendations were calibrated for use with a 30° trajectory angle; therefore, gusset plates are typically designed using an equivalent cross section defined by the Whitmore criterion. The equivalent column method is discussed further in AISC Design Guide 29, *Vertical Bracing Connections—Analysis and Design*, Appendix C (Muir and Thornton, 2014).

Dowswell (2006) summarized the available research on gusset plate stability and proposed effective length factors for various configurations. He also discussed several sources of inaccuracy in the design model, two of which are listed here:

1. Although the effective width is calculated at the last fastener near the end of the brace, the stress continues to spread out beyond the effective width.

Bo Dowswell, PhD, PE, ARC International, LLC, Birmingham, AL. Email: bo@arcstructural.com

Paper No. 2017-17R

2. Due to stress redistribution when the plate yields, the effective width in the inelastic range is larger than predicted using the 30° angle.

In an effort to develop a more accurate design model for gusset plates in compression, these issues are evaluated in this paper. A new design procedure, based on Thornton's equivalent column concept, has been developed. To evaluate the proposed design procedure, the available experimental and finite element results are compared to the predicted strength of each specimen.

Gusset plates are fabricated in many different configurations; however, only two are addressed in this paper: corner gusset plates and extended corner gusset plates. The corner and extended corner configurations have a single brace framing to the gusset plate at the intersection of two other orthogonal framing members. The gusset plate is connected to both members. For corner gussets, a line through the innermost bolts, perpendicular to the brace line of action, intersects one or both of the connected gusset boundaries as shown in Figure 3(a). For the extended corner configuration, the gusset plate is shaped so the free edges are cut at an angle to the connected edges as shown in Figure 3(b). In this case, a line through the innermost bolts, perpendicular to the brace line of action, intersects both of the gusset-free edges.

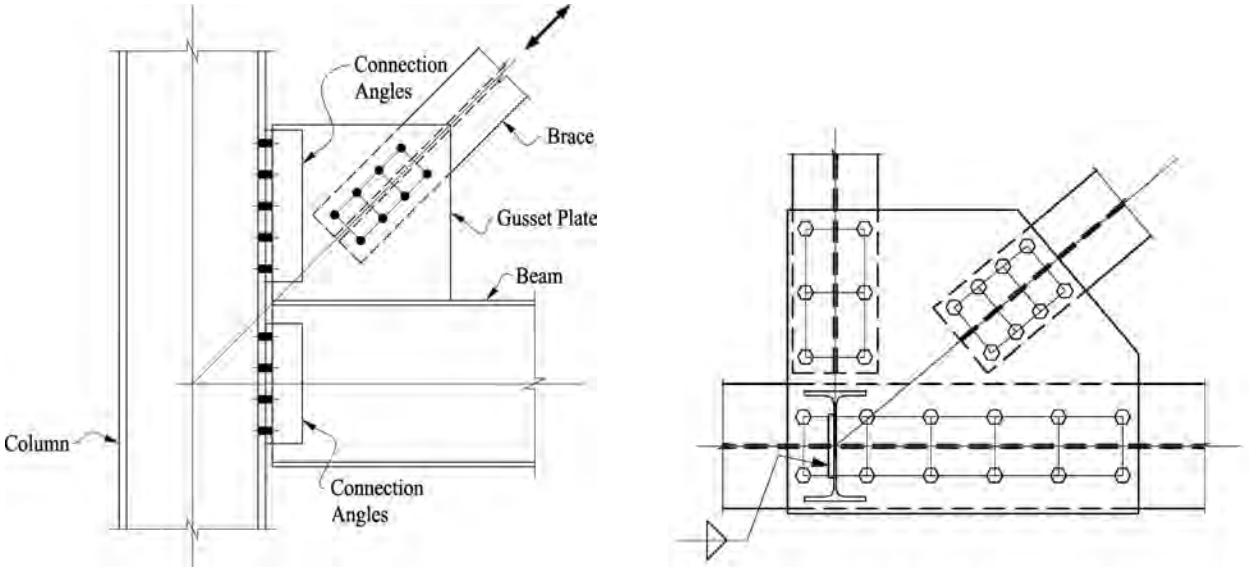

(a) vertical brace connection with a single-plane gusset plate *(b) truss connection with a double-plane gusset plate*

Fig. 1. Gusset plate connections.

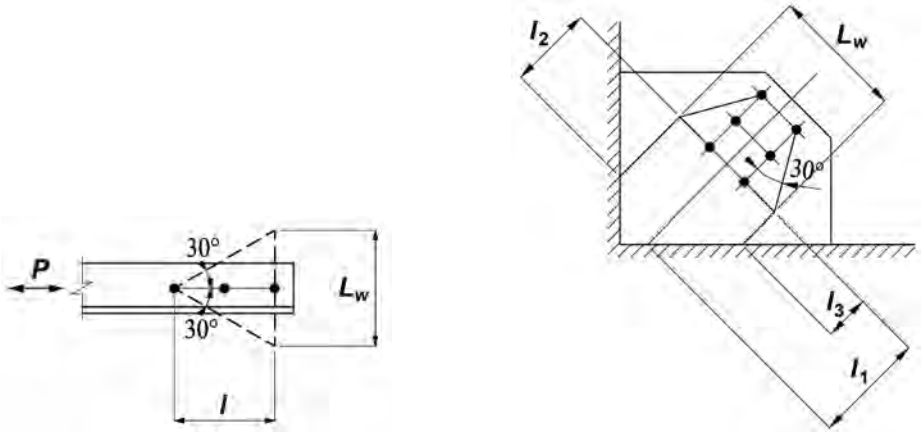

(a) effective width *(b) buckling length*

Fig. 2. Current design of gusset plates.

EXISTING RESEARCH

The existing research on stress trajectories was reviewed by Dowswell (2013). The early research by Wyss (1923), Sandel (1950), and Whitmore (1952) focused on the measurement of elastic stresses. The researchers generally agreed that the stress trajectories formed approximately 30° lines with the connected member. Additional research by Lavis (1967), Rabern (1983), Chakrabarti (1983), Bjorhovde and Chakrabarti (1985), Gross and Cheok (1988), and Girard et al. (1995) verified the 30° stress trajectories. However, the experimental observations of Yamamoto et al. (1985) and Cheng and Grondin (1999) showed that the stress dispersion angle increases with inelastic material behavior. Cheng and Grondin (1999) recommended a 45° dispersion angle.

Dowswell (2006) reviewed the literature on gusset stability prior to 2006, including research by Chakrabarti (1987), Brown (1988), Gross and Cheok (1988), Yam and Cheng (1993), Rabinovitch and Cheng (1993), Walbridge et al. (1998), Nast et al. (1999), and Sheng et al. (2002). For the current paper, the data from Dowswell (2006) was combined with newer data from the research of Hamedani et al. (2011), Mentes (2011), Higgins et al. (2013), Naghipour et al. (2013), and White et al. (2013). The research projects included single- and double-plane gusset plates as well as corner- and extended-corner gusset plates. This paper used the results of experimental testing and inelastic finite element models from 12 separate projects with a total of 162 specimens.

VARIABLE STRESS TRAJECTORIES

Using fracture mechanics, Dowswell (2013) showed that the dispersion angle, θ, is dependent on geometry, constraint, and inelastic deformation capacity. The model in Figure 4(a), based on the stress-free zone ahead of a crack, was used to develop Equation 1, which accounts for all variables affecting the dispersion angle. Equation 1 is plotted in Figure 4(b).

$$\tan\theta = \frac{4C(\alpha - ½)}{\pi\lambda\beta^2} \quad (1)$$

where

C = constraint factor
= 1.00 for uniaxial stress
= 1.32 for constraint in one direction
= 2.27 for constraint in two directions

α = factor accounting for inelastic potential
= 1.0 for gusset plates with no inelastic capacity
= 1.7 for gusset plates with full inelastic potential

β = geometry factor

λ = inelastic material parameter calculated with Equation 2

$$\lambda = 1 + 0.77(\alpha - 1) \quad (2)$$

To determine θ as a function of α, substitute $\beta = 1.0$ for corner gusset plates, $C = 1.0$ for plates with uniaxial stress, and λ from Equation 2 into Equation 1 to get Equation 3.

$$\tan\theta = \frac{\alpha - ½}{0.605\alpha + 0.181} \quad (3)$$

Equation 3 results in trajectory angles of 32.5° for plates with no inelastic capacity and 44.8° for plates with full inelastic potential. The effective width, shown in Figure 5(a), is

$$b_e = 2a = 2l\tan\theta \quad (4)$$

where

a = crack half-length, in.

l = length, parallel to the load, of the connection between outermost fasteners, in.

In some cases, the effective width can extend beyond the free boundaries of the plate as shown in Figure 5(b), causing a smaller effective width than calculated with Equation 4.

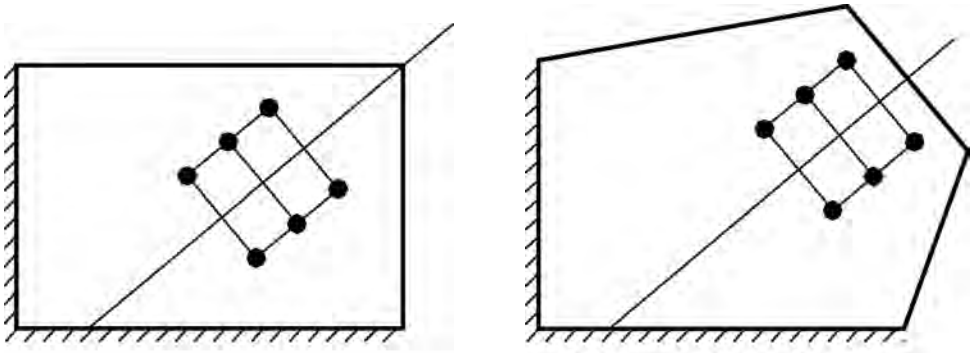

(a) corner gusset plate *(b) extended corner gusset plate*

Fig. 3. Gusset plate configurations.

The shaded portion of the stress trajectory is not effective, and the effective width is based on the actual plate width at the critical section. This effect was accounted for in the calculation of predicted strengths for validating the design procedure. For conditions where the effective width extended beyond the connected boundaries of the plate, the full effective width was used in the calculation of the predicted strength.

The trajectory angle for gusset plates subjected to tension is limited only by the rupture ductility, resulting in $\alpha = 1.7$ and $\theta = 45°$. For gusset plates in compression, α is dependent on the plate slenderness. Because the lateral buckling strength of the equivalent column is based on the AISC column curve, α can be calculated using AISC *Specification* Section E3. The column curve is in the inelastic range when $\lambda_c \le \lambda_r$, where $\lambda_r = 1.5$, and the slenderness parameter, λ_c, is calculated with Equation 5.

$$\lambda_c = \frac{KL}{\pi r}\sqrt{\frac{F_y}{E}} \tag{5}$$

where

E = modulus of elasticity, ksi
F_y = specified minimum yield strength, ksi
K = effective length factor
L = column length, in.
r = radius of gyration, in.
λ_c = slenderness parameter

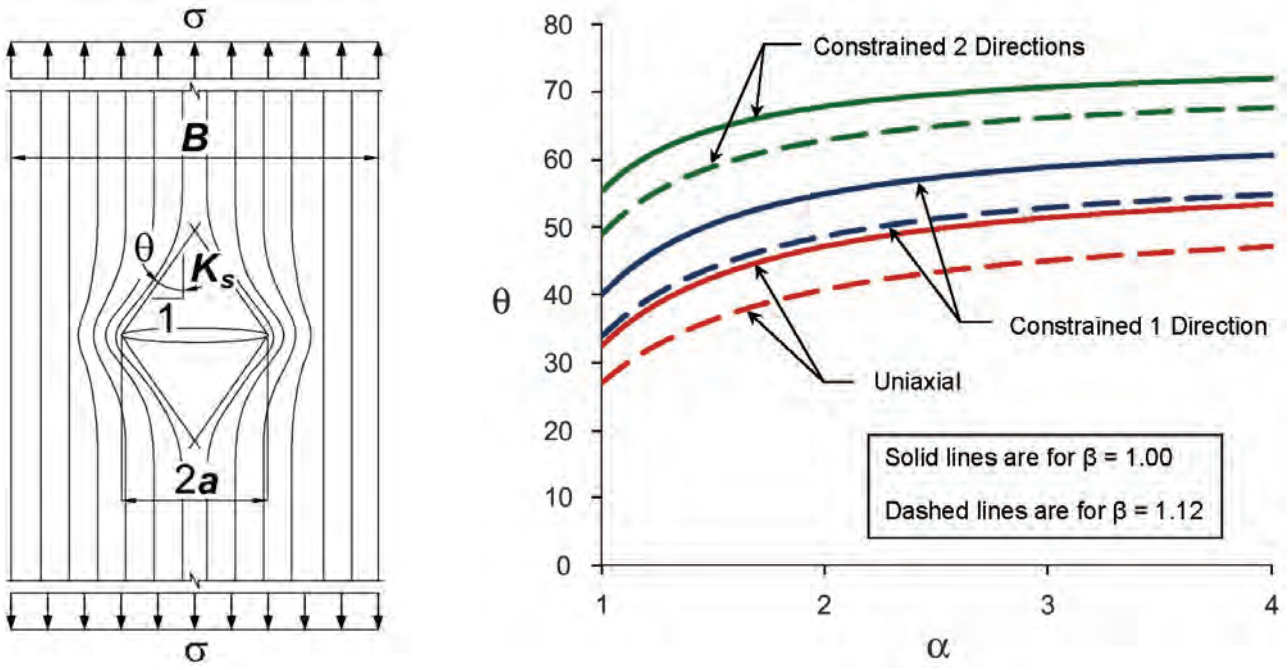

(a) stress-free zone ahead of a crack *(b) dispersion angle vs. normalized strain*

Fig. 4. Variable stress trajectories.

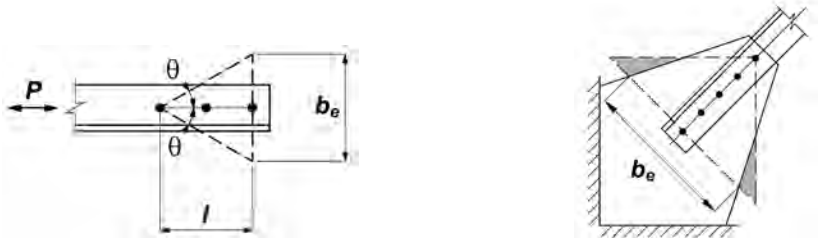

(a) variable effective width *(b) maximum effective width*

Fig. 5. Effective width.

λ_r = limiting slenderness parameter between elastic and inelastic behavior

For design purposes, linear interpolation can be used between $\alpha = 1.0$ and 1.7, resulting in Equation 6.

$$\alpha = 1.7 - 0.7\frac{\lambda_c}{\lambda_r} \geq 1.0 \quad (6)$$

Equation 6 is substituted into Equation 3 with $\lambda_r = 1.5$, resulting in Equation 7.

$$\tan\theta = \frac{1 - 0.389\lambda_c}{1 - 0.236\lambda_c} \quad (7)$$

Setting a lower limit of $\theta = 32.5°$, θ can be calculated with Equation 8, which results in $32.5° \leq \theta \leq 43.7°$.

$$\tan\theta = 0.956 - 0.213\lambda_c \geq 0.637 \quad (8)$$

Equation 5 is substituted into Equation 8, resulting in Equation 9.

$$\tan\theta = 0.956 - \frac{0.213K_\theta L}{\pi r}\sqrt{\frac{F_y}{E}} \geq 0.637 \quad (9)$$

To allow the use of different effective length factors in the stress dispersion angle and buckling strength calculations, K_θ was substituted for K in Equation 9.

EFFECTIVE LENGTH FACTORS

The dispersion angle, θ, defines the stress trajectory within the length of the fastener group; however, the stress continues to disperse through the gusset plate beyond the effective width as shown in Figure 6(a). This has a load-shedding effect on the equivalent column, where the load from the area bound by the effective width disperses into adjacent parts of the plate. The problem is similar to a column with a concentrated load at the top and a distributed load along the column length as shown in Figure 6(b). For corner gusset plates, the brace load also enters the framing members at the connected gusset boundaries, resulting in the shedding of a large portion of the load along the equivalent column length.

Another beneficial effect is the restraint from the relatively low-stress areas of the gusset plate adjacent to the equivalent column. Due to these and other effects discussed by Dowswell (2006), effective length factors for gusset plates cannot be estimated based on the buckled shape as they are for simple prismatic columns.

Effective length factors, both the effective width, K_θ, and buckling strength, K, calculations, were selected empirically, using the experiments and finite element models discussed in the Existing Research section of this paper. Although many of the specimens buckled in a sidesway mode, the empirical evidence shows that effective length factors much lower than the theoretical value of 1.0 can be safely used.

The effective length factors must be selected for use with a specific buckling length. Thornton (1984) originally proposed an effective length factor of 0.65 for use with a 30° stress dispersion angle and a buckling length, l_{avg}, which is the average of l_1, l_2, and l_3 as shown in Figure 2(b). When variable stress trajectories are used, the empirical data shows that a more accurate solution is obtained using a buckling length, $L = l_1$, which is the unsupported length along the center of the brace. Therefore, all effective length factors proposed in this paper have been calibrated for use with the unsupported length along the center of the brace.

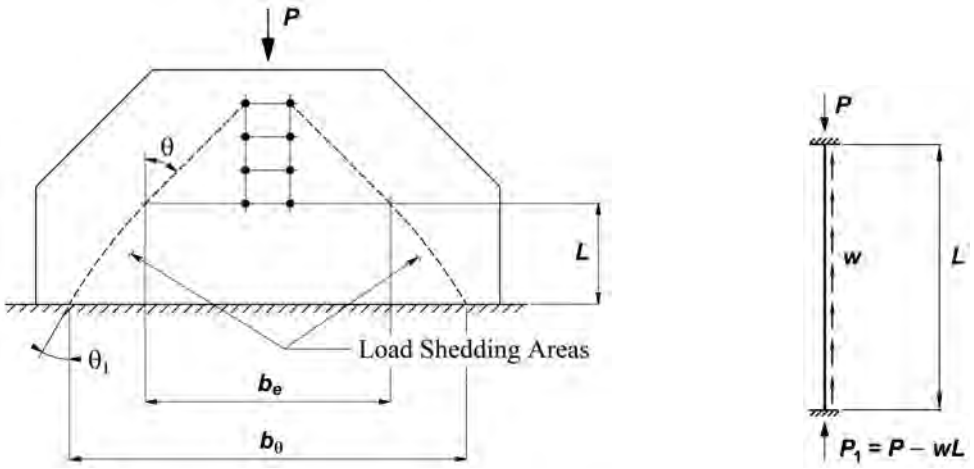

(a) gusset plate *(b) column model*

Fig. 6. Stress dispersion beyond the effective width.

RELIABILITY ANALYSIS

A reliability analysis was used to determine the most efficient combination of K_θ, K, and ϕ that provides a minimum β_R of 4.0, which is the applicable target reliability index for connections according to AISC *Specification* Section B3.1. Commentary. The buckling strength for the analysis was calculated using the provisions in AISC *Specification* Section J4.4 with the measured material and geometric properties of the experimental specimens. The reduction factor required to obtain a specific reliability level is (Galambos and Ravinda, 1978):

$$\phi = C_R \rho_R e^{-\beta_R \alpha_R V_R} \tag{10}$$

where

C_R = correction factor
V_R = coefficient of variation
α_R = separation factor
β_R = reliability index
ρ_R = bias coefficient

Galambos and Ravinda (1973) proposed a separation factor, α_R, of 0.55. For $L/D = 3.0$, Grondin et al. (2007) developed Equation 11 for calculating a correction factor, C, which is 0.900 at $\beta = 4.0$.

$$C_R = 1.4056 - 0.1584\,\beta_R + 0.008\,\beta_R^2 \tag{11}$$

The bias coefficient is

$$\rho_R = \rho_M \rho_G \rho_P \tag{12}$$

where

ρ_G = bias coefficient for the geometric properties
ρ_M = bias coefficient for the material properties
ρ_P = bias coefficient for the test-to-predicted strength ratios. Mean value of the professional factor is calculated with the measured geometric and material properties.

The coefficient of variation is

$$V_r = \sqrt{V_M^2 + V_G^2 + V_P^2} \tag{13}$$

where

V_G = coefficient of variation for the geometric properties
V_M = coefficient of variation for the material properties
V_P = coefficient of variation for the test-to-predicted strength ratios

Hess et al. (2002) recommended $\rho_G = 1.05$ and $V_G = 0.044$ for plate thickness variations. For the plate yield strength, $\rho_M = 1.11$ and $V_M = 0.054$ (Schmidt and Bartlett, 2002).

For corner gusset plates, the reliability analysis resulted in $K_\theta = 0.85$, $K = 0.40$, and $\phi = 0.75$ at $\beta_R = 4.0$. With these values, the mean ratio of the professional factor, ρ_P, is 1.12 and the coefficient of variation, V_P, is 0.192. Dowswell (2018), who analyzed the reliability of several existing design methods, showed that the minimum V_p for all of the existing methods is 0.270. Therefore, the proposed design method is substantially more accurate than the existing methods.

Because only 13 specimens are available for extended corner gusset plates, a reliability analysis was not conducted. With $K_\theta = 0.85$ and $K = 0.50$, $\rho_P = 1.15$, $V_P = 0.129$, and the minimum professional factor is 0.840. Although a lower value could potentially be justified, it is believed that, until further research is available, $K = 0.50$ provides a reasonable fit for extended corner gusset plates.

DESIGN MODEL

For the proposed design model, $K_\theta = 0.85$ and $r = t/\sqrt{12}$ were substituted into Equation 9 and the equation was adjusted so the trajectory angles are within $30° \le \theta \le 45°$, resulting in Equation 14.

$$\tan\theta = 1 - \frac{L}{5t}\sqrt{\frac{F_y}{E}} \ge \tan 30° \tag{14}$$

The effective width, b_e, is calculated with Equation 4; however, b_e is limited to the actual plate width at the critical section as shown in Figure 5(b). The equivalent rectangular column, $b_e \times t$, is designed according to AISC *Specification* Section J4.4 using $\phi = 0.75$ in lieu of 0.90. The length of the equivalent column, L, is defined along the center of the brace as shown in Figure 7, with $K = 0.40$ for corner gusset plates and $K = 0.50$ for extended corner gusset plates.

Results of experimental testing and finite element models discussed in the Existing Research section of this paper are compared to the predicted strengths from the design model in Tables A1 and A2 of Appendix A. The normalized experimental load, P_e/P_y, is plotted against λ_c in Figure 8. P_e is the experimental strength and $P_y = \sigma_y b_e t$ is the axial yield load of the equivalent column, based on the measured yield stress, σ_y.

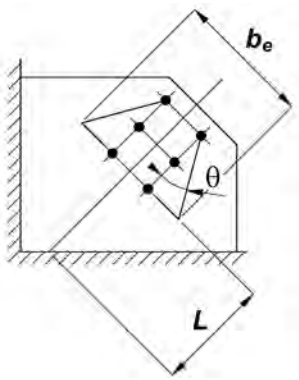

Fig. 7. Gusset geometry for proposed design procedure.

CONCLUSIONS

Gusset plates subjected to compression loads are currently designed with an equivalent column model, where the width of the equivalent column is defined by a 30° stress dispersion angle. However, both experimental and theoretical research has shown that the dispersion angle is partially dependent on the inelastic deformation capacity of the plate. To account for this behavior, a new design model for buckling of corner gusset plates has been developed. The model is valid for single- and double-plane corner gusset plates, including extended corner gusset plates commonly used for seismic design.

The design model, based on the equivalent column concept, allows variable trajectories which are dependent on the level of inelasticity that can be reached prior to buckling. A reliability analysis using the results of 162 specimens from 14 previously-published research projects showed that the buckling strength can be calculated using the provisions in AISC *Specification* Section J4.4 with $\phi = 0.75$ in lieu of 0.90. The length of the equivalent column, L, is defined along the center of the brace with $K = 0.40$ for corner gusset plates and $K = 0.50$ for extended corner gusset plates. The proposed design model was shown to produce more accurate results than the existing design methods.

DESIGN EXAMPLE

Given:

Determine the buckling strength of the gusset plate in Figure 9. The gusset plate is ½-in. thick ASTM A572 Grade 50 material, and the factored brace axial compression load is 800 kips.

Solution:

From AISC *Manual* Table 2-4
ASTM A572, Grade 50
$F_y = 50$ ksi

From AISC *Manual* Table 1-1
W14×109
$d = 14.3$ in.

W21×132
$d = 21.8$ in.

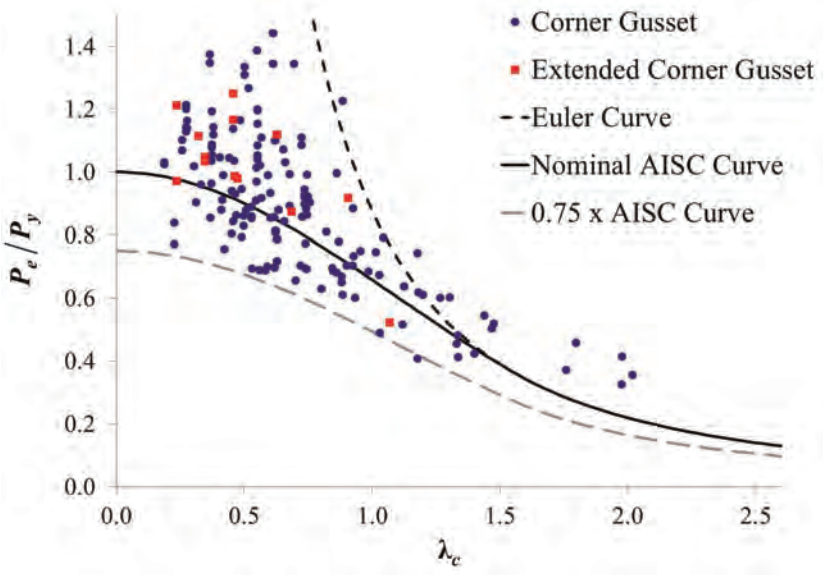

Fig. 8. Normalized load vs. slenderness for proposed design procedure.

$$L = 34 \text{ in.} - \frac{21.8 \text{ in.}}{2 \cos 50°}$$
$$= 17.0 \text{ in.}$$

$$\tan \theta = 1 - \frac{L}{5t}\sqrt{\frac{F_y}{E}} \geq \tan 30° \quad (14)$$
$$= 1 - \frac{17.0 \text{ in.}}{(5)(0.500 \text{ in.})}\sqrt{\frac{50 \text{ ksi}}{29{,}000 \text{ ksi}}} \geq \tan 30°$$
$$\theta = 35.7°$$

The gage in the 4-in. leg of the L6×4×¾, g, is 2.50 in.

The distance between bolts perpendicular to the load, w, is:

$$w = d + 2g$$
$$= 14.3 \text{ in.} + 2(2.5 \text{ in.})$$
$$= 19.3 \text{ in.}$$

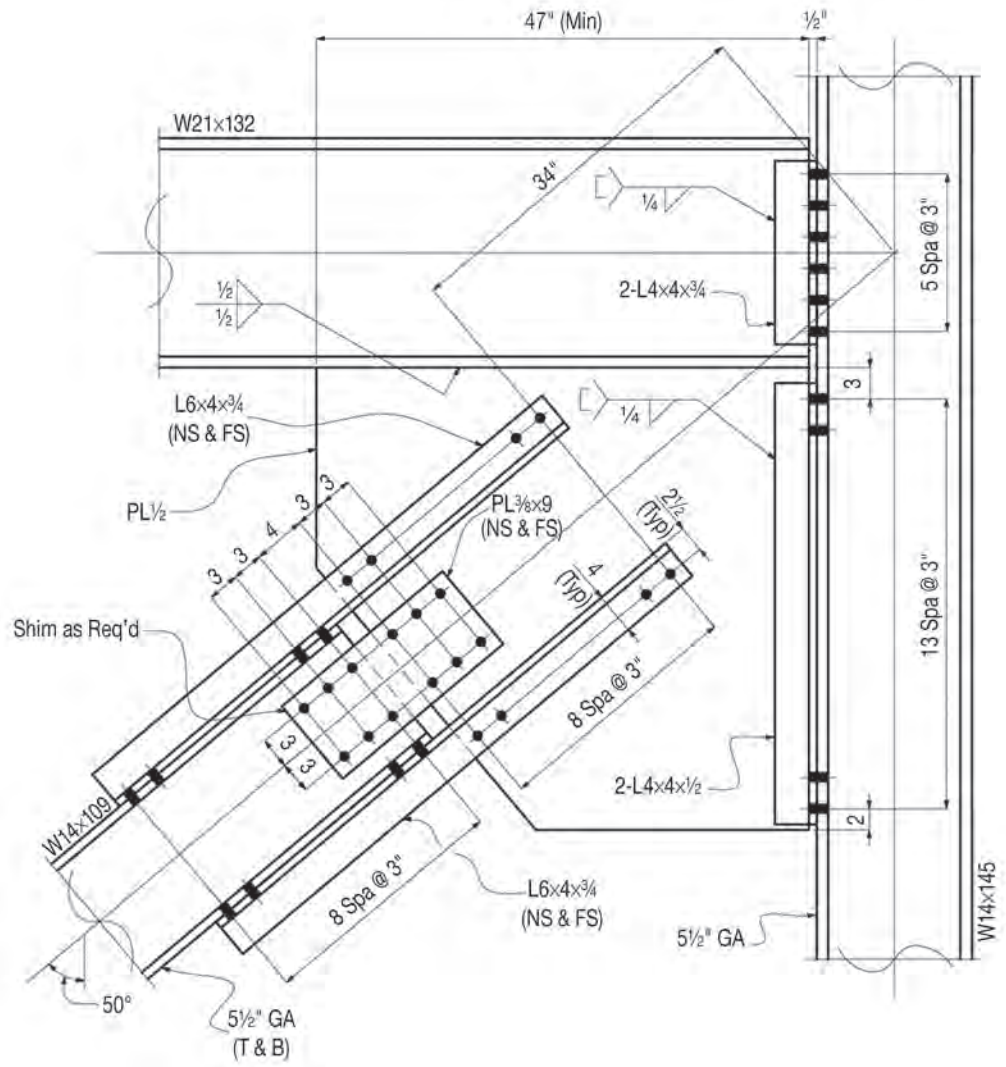

Fig. 9. Vertical bracing connection for Design Example.

The distance between bolts, parallel to the load, l, is:

$$\begin{aligned} l &= 8(3 \text{ in.}) \\ &= 24.0 \text{ in.} \end{aligned}$$

$$\begin{aligned} b_e &= 2l \tan\theta + w \\ &= \left[2(24 \text{ in.}) \tan(35.7°)\right] + 19.3 \text{ in.} \\ &= 53.8 \text{ in.} \end{aligned}$$

$$\begin{aligned} A_g &= (0.500 \text{ in.})(53.8 \text{ in.}) \\ &= 26.9 \text{ in.}^2 \end{aligned}$$

$$\begin{aligned} r &= \frac{t}{\sqrt{12}} \\ &= \frac{0.500 \text{ in.}}{\sqrt{12}} \\ &= 0.144 \text{ in.} \end{aligned}$$

Because the line through the innermost bolts, perpendicular to the brace line of action, intersects both the beam and column interfaces, the plate is classified as a corner gusset; therefore, $K = 0.40$.

$$\begin{aligned} L_c &= KL \\ &= (0.4)(17.0 \text{ in.}) \\ &= 6.80 \text{ in.} \end{aligned}$$

$$\begin{aligned} \frac{L_c}{r} &= \frac{6.80 \text{ in.}}{0.144 \text{ in.}} \\ &= 47.2 \end{aligned}$$

Because $\frac{L_c}{r} = 47.2 > 25$, AISC *Specification* Section J4.4 specifies that the compression strength is calculated according to AISC *Specification* Section E3.

The elastic buckling stress, F_e, is calculated using AISC *Specification* Equation E3-4:

$$\begin{aligned} F_e &= \frac{\pi^2 E}{\left(\frac{L_c}{r}\right)^2} \qquad \text{(Spec. Eq. E3-4)} \\ &= \frac{\pi^2 (29{,}000 \text{ ksi})}{(47.2)^2} \\ &= 128 \text{ ksi} \end{aligned}$$

$$\begin{aligned} 4.71\sqrt{\frac{E}{F_y}} &= 4.71\sqrt{\frac{29{,}000 \text{ ksi}}{50 \text{ ksi}}} \\ &= 113 \end{aligned}$$

Because $\frac{L_c}{r} = 47.2 < 113$, the critical stress, F_{cr}, is calculated using AISC *Specification* Equation E3-2.

$$F_{cr} = \left(0.658^{\frac{F_y}{F_e}}\right) F_y \qquad \text{(Spec. Eq. E3-2)}$$

$$= \left(0.658^{\frac{50 \text{ ksi}}{128 \text{ ksi}}}\right)(50 \text{ ksi})$$

$$= 42.5 \text{ ksi}$$

And the nominal compressive strength, P_n, is calculated using AISC *Specification* Equation E3-1.

$$P_n = F_{cr} A_g \qquad \text{(Spec. Eq. E3-1)}$$

$$= (42.5 \text{ ksi})(26.9 \text{ in.}^2)$$

$$= 1{,}140 \text{ kips}$$

The available compression strength is then:

$$\phi P_n = (0.75)(1{,}140 \text{ kips})$$

$$= 855 \text{ kips} > 800 \text{ kips} \quad \textbf{o.k.}$$

For the Dowswell (2006) method, the gusset is compact; therefore, the compression strength is based on Whitmore yielding. P_n = 1,180 kips, which is 3.51% higher than the strength calculated with the proposed method.

For the Thornton (1984) method, $L = l_{avg} = 4.71$ in. and $K = 0.65$. Because $KL/r < 25$, the compression strength is based on Whitmore yielding. P_n = 1,180 kips, which is 3.51% higher than the strength calculated with the proposed method.

For this example, the nominal strength calculated with the proposed method is similar to the nominal strengths calculated with both the Thornton (1984) and Dowswell (2006) methods. However, the reliability analysis showed that the proposed method is significantly more accurate than the existing methods for a wide range of slenderness values, potentially resulting in increased available strengths, ϕP_n, if all methods use a target reliability index of 4.0. Also, the proposed method more accurately models the stress trajectories in the gusset plate.

APPENDIX A TABLES

Table A1. Details of Corner Gusset Plates

Specimen	t in.	F_y ksi	E ksi	L in.	θ deg	b_e in.	P_c kips	P_e kips	P_e/P_c
Chakrabarti (1987)									
1	0.250	36.0	29000	8.00	37.8	9.20	74.6	68.7	0.920
2	0.250	36.0	29000	8.50	37.3	9.08	72.7	70.3	0.966
3	0.250	36.0	29000	8.00	37.8	9.20	74.6	71.4	0.957
Brown (1988)									
1-4-45-8	0.251	48.0	29500	7.75	36.9	10.8	114	180	1.58
2-3-45-4	0.196	45.2	29500	5.18	38.4	11.9	96.6	120	1.24
3-3-45-8	0.198	45.2	29500	7.75	34.7	10.2	75.7	82.0	1.08
9-3-55-4	0.192	45.2	29500	4.68	39.0	12.1	97.8	79.6	0.814
10-3-45-4	0.197	45.2	29500	5.26	38.3	11.9	96.6	110	1.13
11-4-40-8	0.250	48.0	29500	7.26	37.4	10.9	117	166	1.42
13-4-30-8	0.248	48.0	29500	6.16	38.6	11.2	123	139	1.13
14-4-30-4	0.248	48.0	29500	3.16	41.9	13.5	157	135	0.859
15-4-35-8	0.250	48.0	29500	6.80	38.0	11.0	120	154	1.29
16-4-35-4	0.250	48.0	29500	4.65	40.4	12.7	146	147	1.01
17-3-45-8	0.194	45.2	29500	7.79	34.4	10.2	73.0	120	1.64
18-4-45-4	0.251	48.0	29500	5.71	39.2	12.2	138	155	1.12
20-6-30-4	0.376	45.0	28300	4.81	41.9	13.5	223	176	0.789
Gross and Cheok (1988)									
1A	0.250	46.7	29000	8.01	36.6	8.94	91.3	116	1.27
1B	0.250	46.7	29000	8.01	36.6	8.94	91.3	96.0	1.05
2A	0.250	46.7	29000	8.63	35.9	8.78	87.7	138	1.57
2B	0.250	46.7	29000	8.63	35.9	8.78	87.7	148	1.69
3B	0.250	46.7	29000	8.51	36.0	8.82	88.4	88.0	1.00
Rabinovitch and Cheng (1993)									
A1	0.367	65.1	29878	8.72	37.9	19.9	430	378	0.879
A2	0.243	64.3	29878	8.72	33.7	17.5	218	254	1.16
A3	0.367	65.1	29878	8.72	37.9	19.9	430	451	1.05
A4	0.243	64.3	29878	8.72	33.7	17.5	218	258	1.18
Yam and Cheng (1993)									
GP1	0.524	42.8	30110	8.56	41.2	17.2	373	440	1.18
GP2	0.386	44.2	30487	8.56	39.7	16.4	264	305	1.15
GP3	0.256	39.9	28428	8.56	36.9	15.1	135	167	1.23
GP1R	0.524	42.8	30110	8.56	41.2	17.2	373	462	1.24
GP2R	0.386	44.2	30487	8.56	39.7	16.4	264	334	1.26
GP3R	0.256	39.9	28428	8.56	36.9	15.1	135	178	1.31
AP1	0.524	42.8	30110	9.58	40.8	16.9	365	387	1.06
AP2	0.386	44.2	30487	9.58	39.0	16.1	255	272	1.07
AP3	0.256	39.9	28428	9.58	35.7	14.6	127	164	1.29
MP1	0.524	42.8	30110	8.56	41.2	17.2	373	435	1.17
MP2	0.386	44.2	30487	8.56	39.7	16.4	264	296	1.12
MP3	0.256	39.9	28428	8.56	36.9	15.1	135	162	1.20
MP3A	0.256	39.9	28428	8.56	36.9	15.1	135	184	1.36
MP3B	0.256	39.9	28428	8.56	36.9	15.1	135	185	1.36
SP1-Free	0.524	42.8	30110	19.7	35.6	22.4	426	361	0.848
SP2-Free	0.386	44.2	30487	19.7	31.4	19.5	244	227	0.930
SP1-Fixed	0.524	42.8	30110	19.7	35.6	22.4	426	396	0.929
SP2-Fixed	0.386	44.2	30487	19.7	31.4	19.5	244	332	1.36

Table A1. Details of Corner Gusset Plates (continued)									
Specimen	t in.	F_y ksi	E ksi	L in.	θ deg	b_e in.	P_c kips	P_e kips	P_e/P_c
Walbridge et al. (1998)									
GP1B1	0.236	43.5	29878	8.72	35.7	18.6	163	155	0.952
GP1B3	0.236	43.5	29878	8.72	35.7	18.6	163	156	0.957
GP2B7	0.354	43.5	29878	8.72	39.1	20.7	296	290	0.980
GP3B11	0.472	43.5	29878	8.72	40.7	21.7	428	403	0.941
GP1MC20	0.524	42.8	30110	8.56	41.2	17.1	372	466	1.25
GP2MC22	0.386	44.2	30487	8.56	39.7	16.4	264	302	1.14
GP3MC24	0.256	39.9	28428	8.56	36.9	15.0	135	160	1.18
A2CL2	0.243	64.3	29878	8.72	33.7	17.5	218	246	1.13
A4CL4	0.243	64.3	29878	8.72	33.7	17.5	218	252	1.15
Nast et al. (1999)									
T2-FE	0.378	61.5	31256	8.72	38.5	20.3	434	444	1.02
T2	0.378	61.5	31256	8.72	38.5	20.3	434	380	0.876
Sheng et al. (2002)									
500×400×13.3×240	0.524	42.8	29008	11.3	39.8	11.9	251	366	1.45
500×400×13.3×310	0.524	42.8	29008	8.56	41.2	17.1	372	447	1.20
500×400×13.3×380	0.524	42.8	29008	5.80	42.5	22.8	504	528	1.05
750×400×13.3×240	0.524	42.8	29008	11.3	39.8	11.9	251	359	1.43
750×400×13.3×310	0.524	42.8	29008	8.56	41.2	17.1	372	438	1.18
750×400×13.3×380	0.524	42.8	29008	5.80	42.5	22.8	504	525	1.04
500×400×9.87×240	0.389	44.2	29008	11.3	37.7	11.2	173	257	1.48
500×400×9.87×310	0.389	44.2	29008	8.56	39.6	16.4	265	322	1.22
500×400×9.87×380	0.389	44.2	29008	5.80	41.5	22.2	370	420	1.13
750×400×9.87×240	0.389	44.2	29008	11.3	37.7	11.2	173	252	1.46
750×400×9.87×310	0.389	44.2	29008	8.56	39.6	16.4	265	315	1.19
750×400×9.87×380	0.389	44.2	29008	5.80	41.5	22.2	371	408	1.10
500×400×6.5×240	0.256	39.9	29008	11.3	33.9	10.1	82.7	114	1.38
500×400×6.5×310	0.256	39.9	29008	8.56	37.0	15.1	136	156	1.15
500×400×6.5×380	0.256	39.9	29008	5.80	39.8	21.0	203	222	1.10
750×400×6.5×240	0.256	39.9	29008	11.3	33.9	10.1	82.7	112	1.35
750×400×6.53×10	0.256	39.9	29008	8.56	37.0	15.1	136	150	1.10
750×400×6.5×380	0.256	39.9	29008	5.80	39.8	21.0	203	207	1.02
Hamedani et al. (2011)									
GP1	0.524	42.8	30110	8.56	41.2	17.2	373	462	1.24
GP2	0.386	44.2	30487	8.56	39.7	16.4	264	312	1.18
GP3	0.256	39.9	28428	8.56	36.9	15.1	135	172	1.27
Hafner (2012)									
1	0.250	47.0	29000	28.4	30.0	34.8	88.1	146	1.66
2	0.250	45.1	29000	28.4	30.0	34.8	88.1	163	1.85
3	0.375	45.9	29000	28.4	30.0	34.8	286	273	0.955
4	0.250	45.1	29000	28.4	30.0	34.8	88.1	128	1.45
5	0.375	46.1	29000	28.4	30.0	34.8	286	290	1.01
6	0.375	46.3	29000	28.4	30.0	34.8	286	249	0.869

Table A1. Details of Corner Gusset Plates (continued)									
Specimen	t in.	F_y ksi	E ksi	L in.	θ deg	b_e in.	P_c kips	P_e kips	P_e/P_c
Mentes (2011)									
GP307-SS3	0.375	36.4	29000	13.1	37.0	28.8	347	358	1.03
GP307-LS3	0.375	48.2	29000	18.1	31.2	28.2	372	398	1.07
GP490-SS3	0.375	46.4	29000	13.1	35.8	24.4	362	364	1.00
GP490-LS3-1	0.375	45.9	29000	18.1	31.6	22.3	285	264	0.928
Naghipour et al. (2013)									
1	0.157	53.7	30458	16.6	30.0	9.91	19.2	25.3	1.32
2	0.157	53.7	30458	13.9	30.0	13.1	36.4	45.2	1.24
3	0.157	53.7	30458	11.1	30.0	16.3	62.5	82.9	1.33
4	0.157	53.7	30458	8.3	30.9	20.1	99.2	169	1.70
5	0.315	53.7	30458	22.2	30.0	9.91	76.2	55.6	0.729
6	0.315	53.7	30458	19.4	30.0	13.1	115	88.0	0.764
7	0.315	53.7	30458	16.7	30.9	16.8	166	141	0.849
8	0.315	53.7	30458	13.9	33.7	21.9	239	232	0.971
9	0.315	53.7	30458	11.2	36.2	27.7	328	377	1.15
10	0.472	53.7	30458	21.4	33.3	10.8	175	201	1.15
11	0.472	53.7	30458	18.7	35.1	15.1	260	321	1.24
12	0.472	53.7	30458	15.9	36.7	20.0	360	420	1.17
13	0.472	53.7	30458	13.1	38.3	25.3	475	485	1.02
14	0.472	53.7	30458	10.4	39.8	31.1	605	547	0.905
15	0.630	53.7	30458	28.3	33.5	10.8	235	274	1.17
16	0.630	53.7	30458	25.5	34.8	15.0	340	409	1.20
17	0.630	53.7	30458	22.8	36.0	19.6	461	501	1.09
18	0.630	53.7	30458	20.0	37.2	24.5	597	597	1.00
19	0.630	53.7	30458	17.2	38.4	29.8	748	690	0.922
Test	0.315	53.7	30458	16.6	31.0	10.2	101	90.7	0.899
20	0.315	53.7	30458	16.6	31.0	10.2	101	93.4	0.926
White et al. (2013)									
P5U-WV-NP-01	0.250	53.0	29000	23.8	30.0	43.2	155	263	1.69
	0.313	53.0	29000	23.8	30.0	43.2	301	390	1.30
	0.375	53.0	29000	23.8	30.0	43.2	471	525	1.12
	0.400	53.0	29000	23.8	30.0	43.2	540	585	1.08
	0.438	53.0	29000	23.8	30.0	43.2	644	675	1.05
	0.500	53.0	29000	23.8	30.7	43.8	828	818	0.987
	0.625	53.0	29000	23.8	34.0	46.0	1227	1073	0.874
P6U-WV-NP-02	0.250	53.0	29000	18.5	30.0	46.2	270	260	0.963
	0.313	53.0	29000	18.5	30.0	46.2	453	396	0.873
	0.375	53.0	29000	18.5	30.0	46.2	638	554	0.868
	0.438	53.0	29000	18.5	32.5	49.4	878	723	0.824
	0.500	53.0	29000	18.5	34.3	51.9	1121	904	0.807
	0.600	53.0	29000	18.5	36.4	54.7	1510	1198	0.793
	0.625	53.0	29000	18.5	36.7	55.3	1607	1266	0.787
P8U-WV-INF-02	0.500	53.0	29000	25.3	30.0	49.6	900	987	1.10
P13U-W-NP-01	0.250	53.0	29000	19.6	30.0	46.6	249	322	1.30
	0.313	53.0	29000	19.6	30.0	46.6	431	479	1.11
	0.375	53.0	29000	19.6	30.0	46.6	618	636	1.03
	0.400	53.0	29000	19.6	30.2	46.9	697	702	1.01

Table A1. Details of Corner Gusset Plates (continued)									
Specimen	t in.	F_y ksi	E ksi	L in.	θ deg	b_e in.	P_c kips	P_e kips	P_e/P_c
White et al. (2013) continued									
	0.438	53.0	29000	19.6	31.7	49.1	845	792	0.937
	0.500	53.0	29000	19.6	33.7	51.9	1096	957	0.873
	0.625	53.0	29000	19.6	36.2	54.4	1557	1263	0.811
E1W-307SS	0.250	36.4	29000	13.1	32.2	25.7	177	190	1.07
	0.313	36.4	29000	13.1	35.1	27.6	262	265	1.01
	0.438	36.4	29000	13.1	38.2	29.7	432	409	0.947
	0.500	36.4	29000	13.1	39.2	30.4	515	487	0.945
E2W-307LS	0.250	48.2	29000	18.1	30.0	27.3	162	199	1.23
	0.313	48.2	29000	18.1	30.0	27.3	261	327	1.25
	0.438	48.2	29000	18.1	33.5	29.9	500	546	1.09
	0.500	48.2	29000	18.1	35.2	31.1	521	653	1.25
	0.625	48.2	29000	18.1	37.4	32.9	664	852	1.28
E3W-307SL	0.250	46.6	29000	13.1	30.1	33.2	270	284	1.05
	0.313	46.6	29000	13.1	33.6	36.6	423	369	0.872
	0.375	46.6	29000	13.1	35.8	38.8	578	473	0.818
	0.438	46.6	29000	13.1	37.2	40.4	733	573	0.782
E4W-490SS	0.250	46.4	29000	13.1	30.2	21.6	175	222	1.27
	0.313	46.4	29000	13.1	33.6	23.3	269	299	1.11
	0.438	46.4	29000	13.1	37.3	25.2	455	437	0.960
E5W-490LS	0.250	45.6	29000	18.1	30.0	21.5	126	148	1.18
	0.313	45.6	29000	18.1	30.0	21.5	200	230	1.15
	0.438	45.6	29000	18.1	33.9	23.4	376	402	1.07
	0.500	45.6	29000	18.1	35.5	24.3	468	488	1.04
	0.625	45.6	29000	18.1	37.6	25.4	650	638	0.981

Table A2. Details of Extended Corner Gusset Plates									
Specimen	t in.	F_y ksi	E ksi	L in.	θ deg	b_e in.	P_c kips	P_e kips	P_e/P_c
Sheng et al. (2002)									
440×310×13.3×240	0.524	42.8	29008	11.3	39.8	11.9	244	333	1.36
440×310×13.3×310	0.524	42.8	29008	8.56	41.2	17.1	365	403	1.10
440×310×13.3×380	0.524	42.8	29008	5.80	42.5	22.8	499	496	0.994
390×200×13.3×240	0.524	42.8	29008	11.3	39.8	10.6	217	277	1.27
390×200×13.3×310	0.524	42.8	29008	8.56	41.2	14.4	308	335	1.09
390×200×13.3×380	0.524	42.8	29008	5.80	42.5	17.0	373	463	1.24
390×200×9.87×240	0.389	44.2	29008	11.3	37.7	10.2	149	197	1.32
390×200×9.87×310	0.389	44.2	29008	8.56	39.6	14.4	226	243	1.08
390×200×9.87×380	0.389	44.2	29008	5.80	41.5	17.0	281	327	1.16
390×200×6.5×240	0.256	39.9	29008	11.3	33.9	9.69	70.3	90.8	1.29
390×200×6.5×310	0.256	39.9	29008	8.56	37.0	14.1	118	126	1.06
390×200×6.5×380	0.256	39.9	29008	5.80	39.8	17.0	159	172	1.08
Rabinovitch and Cheng (1993)									
A5	0.367	65.1	29878	15.2	31.6	16.3	242	204	0.843

SYMBOLS

C	Constraint factor
C_R	Correction factor
E	Modulus of elasticity, ksi
F_y	Specified minimum yield strength, ksi
K	Effective length factor used in the buckling strength calculation
K_θ	Effective length factor used for calculating the stress dispersion angle, θ
L	Column length, in.
V_G	Coefficient of variation for the geometric properties
V_M	Coefficient of variation for the material properties
V_P	Coefficient of variation for the test-to-predicted strength ratios
V_R	Coefficient of variation
a	Crack half-length, in.
b_e	Effective width, in.
l	Length, parallel to the load, of the connection between outermost fasteners, in.
r	Radius of gyration, in.
α	Factor accounting for inelastic potential
α_R	Separation factor
β	Geometry factor
β_R	Reliability index
λ	Inelastic material parameter
λ_c	Slenderness parameter
λ_r	Limiting slenderness parameter between elastic and inelastic behavior
ϕ	Reduction factor for designing according to LRFD
ρ_G	Bias coefficient for the geometric properties
ρ_M	Bias coefficient for the material properties
ρ_P	Bias coefficient for the test-to-predicted strength ratios. Mean value of the professional factor calculated with the measured geometric and material properties.
ρ_R	Bias coefficient
θ	Stress dispersion angle, deg

REFERENCES

AISC (2016), *Specification for Structural Steel Buildings*, ANSI/AISC 360–16, American Institute of Steel Construction, Chicago, Ill.

Bjorhovde, R. and Chakrabarti, S.K. (1985), "Tests of Full-size Gusset Plate Connections," *Journal of Structural Engineering,* ASCE, Vol. 111, No. 3, March, pp. 667–683.

Brown, V.L. (1988), *Stability of Gusseted Connections in Steel Structures*, Doctoral Dissertation, University of Delaware, Newark, Del.

Chakrabarti, S.K. (1983), *Tests of Gusset Plate Connections,* M.S. Thesis, University of Arizona, Tucson, Ariz.

Chakrabarti, S.K. (1987), *Inelastic Buckling of Gusset Plates*, Doctoral Dissertation, University of Arizona, Tucson, Ariz.

Cheng, J.J.R. and Grondin, G.Y. (1999), "Recent Developments in the Behavior of Cyclically Loaded Gusset Plate Connections," *Proceedings of the North American Steel Construction Conference*, AISC, Las Vegas, Nev., pp. 8–1 through 8–22.

Dowswell, B. (2006), "Effective Length Factors for Gusset Plate Buckling," *Engineering Journal*, AISC, Vol. 43, No. 2.

Dowswell, B. (2013), "Calculation of Stress Trajectories Using Fracture Mechanics," *Engineering Journal*, AISC, Vol. 50, No. 1.

Dowswell, B. (2016), "Stability of Rectangular Connection Elements," *Engineering Journal*, AISC, Vol. 53, No. 4.

Dowswell, B. (2018), "Reliability of the Equivalent Column Method for Corner Gusset Plates," *Engineering Journal*, AISC, Submitted for Review.

Galambos, T.V. and Ravinda, M.K. (1973), "Tentative Load and Resistance Factor Design Criteria for Steel Buildings," Research Report No. 18, Department of Civil and Environmental Engineering, September, Washington University, St. Louis, Mo.

Galambos, T.V. and Ravinda, M.K. (1978), "Properties of Steel for Use in LRFD," *Journal of the Structural Division*, ASCE, Vol. 104, No. ST9, September, pp. 1,459–1,468.

Girard, C., Picard, A., and Fafard, M. (1995), "Finite Element Modeling of the Shear Lag Effects in an HSS Welded to a Gusset Plate," *Canadian Journal of Civil Engineering*, Vol. 22, pp. 651–659.

Grondin, G., Jin, M., and Josi, G. (2007), "Slip Critical Bolted Connections—A Reliability Analysis for Design at the Ultimate Limit State," Structural Engineering Report No. 274, Department of Civil Engineering, October, University of Alberta, Alberta, Canada.

Gross, J.L. and Cheok, G. (1988), *Experimental Study of Gusseted Connections for Laterally Braced Steel Buildings*, National Institute of Standards and Technology, Gaithersburg, Md.

Hamedani, H., Gholampour, S., and Yadollahi, Y. (2011), "The Effect of Edge Stiffener on Compressive Behavior of Gusset Plate," *Proceedings of the Fifth Symposium on Advances in Science and Technology*, Mashhad, Iran.

Hafner, A.G. (2012), *Experimental Research on the Behavior and Strength of Large-Scale Steel Gusset Plates with Sway-buckling Response Including Effects of Corrosion and Retrofit Options*, Master's Thesis, Oregon State University, Corvallis, Ore., March 20.

Hess, P.E., Bruchman, D., Assakkaf, I.A., and Ayyub, B.M. (2002), "Uncertainties in Material Strength, Geometric and Load Variables," *Naval Engineers Journal*, Vol. 114, No. 2, April, pp. 139–166.

Higgins, C., Hafner, A., Turan, O., and Schumacher, T. (2013). "Experimental Tests of Truss Bridge Gusset Plate Connections with Sway-Buckling Response," *Journal of Bridge Engineering*, Vol. 18, No. 10, pp. 980–991.

Lavis, C.S. (1967), *Computer Analysis of the Stresses in a Gusset Plate*, Master's Thesis, University of Washington, Seattle, Wash.

Mentes, Y. (2011), *Analytical and Experimental Assessment of Steel Truss Bridge Gusset Plate Connections*, Doctoral Dissertation, Georgia Institute of Technology, Atlanta, Ga.

Muir, L.S. and Thornton, W.A. (2014), *Vertical Bracing Connections—Analysis and Design*, Design Guide 29, AISC, Chicago, Ill.

Naghipour, M., Abdollahzadeh, G., and Shokri, M. (2013), "Analysis and Design Procedure of Corner Gusset Plate Connections in BRBFs," *Iranica Journal of Energy and Environment*, Vol. 4, pp. 271–282.

Nast, T.E., Grondin, G.Y., and Cheng, J.J.R. (1999), *Cyclic Behavior of Stiffened Gusset Plate Brace Member Assemblies*, University of Alberta Department of Civil and Environmental Engineering Structural Engineering Report No. 229, University of Alberta, Alberta, Canada.

Rabern, D.A. (1983), *Stress, Strain and Force Distributions in Gusset Plate Connections*, Master's Thesis, University of Arizona, Tucson, Ariz.

Rabinovitch, J. and Cheng, J.J.R. (1993), *Cyclic Behavior of Steel Gusset Plate Connections*, University of Alberta Department of Civil Engineering Structural Engineering Report No. 191, University of Alberta, Alberta, Canada.

Sandel, J.A. (1950), *Photoelastic Analysis of Gusset Plates*, Master's Thesis, University of Tennessee, Knoxville, Tenn.

Schmidt, B.J. and Bartlett, F.M. (2002), "Review of Resistance Factor for Steel: Data Collection," *Canadian Journal of Civil Engineering*, Vol. 29, pp. 98–108.

Sheng, N., Yam, C.H., and Iu, V.P. (2002), "Analytical Investigation and the Design of the Compressive Strength of Steel Gusset Plate Connections," *Journal of Constructional Steel Research*, Vol. 58, pp. 1,473–1,493.

Thornton, W.A. (1984), "Bracing Connections for Heavy Construction," *Engineering Journal*, AISC, Vol. 21, No. 3, pp. 139–148.

Walbridge, S.S., Grondin, G.Y., and Cheng, J.J.R. (1998), *An Analysis of the Cyclic Behavior of Steel Gusset Plate Connections*, University of Alberta Department of Civil and Environmental Engineering Structural Engineering Report No. 225, University of Alberta, Alberta, Canada.

Whitmore, R.E. (1952), *Experimental Investigation of Stresses in Gusset Plates*, University of Tennessee Engineering Experiment Station Bulletin No. 16, University of Tennessee, Knoxville, Tenn.

White, D.W., Leon, R.T., Kim, Y.D., Mentes, Y., and Bhuiyan, M.T.R. (2013), *Finite Element Simulation and Assessment of the Strength Behavior of Riveted and Bolted Gusset-Plate Connections in Steel Truss Bridges*, Final Report Prepared for Federal Highway Administration and NCHRP Transportation Research Board, March.

Wyss, T. (1923), "Die Kraftfelder in Festen Elastischen Korpern und ihre Praktischen Anwendungen," Berlin.

Yamamoto, K., Akiyama, N., and Okumara, T. (1985), "Elastic Analysis of Gusseted Truss Joints," *Journal of Structural Engineering,* ASCE, Vol. 111, No. 12, December, pp. 2,545–2,564.

Yam, M.C.H. and Cheng, J.J.R. (1993), *Experimental Investigation of the Compressive Behavior of Gusset Plate Connections*, University of Alberta Department of Civil Engineering Structural Engineering Report No. 194, University of Alberta, Alberta, Canada.

Updated Equivalent Axial Load Method for Design of Steel Beam-Columns

MATHEW REYNOLDS and CHIA-MING UANG

ABSTRACT

The equivalent axial load method is a design aid that aims to select candidate wide-flange beam-columns with minimal iteration. The method itself was described in previous editions of the AISC *Steel Construction Manual* but has been removed in recent editions. An expanded version of the tables for sizing of both shallow and deep beam-columns based on the latest edition of the AISC *Manual* is presented. Several examples of uniaxial and biaxially loaded beam-columns are provided to demonstrate the effectiveness of the method. The method is validated using a programmed heuristic that designed beam-columns from randomly generated scenarios.

Keywords: beam-column, equivalent axial load, design.

INTRODUCTION

The equivalent axial load method was first developed by Burgett (1973) to efficiently select a candidate shape for the design of steel W-shape beam-columns. In this method, the required moment is first converted into an equivalent axial load component by using the "*m*" factor before it is added to the required axial load. Together with the column design strength table in the AISC *Steel Construction Manual*, a designer can use this equivalent axial load to select a candidate shape. The goal is that the candidate shape is either the most economical shape or very close to it. A table of *m* values was adopted into Part 3 (Column Design) of the 9th edition of the AISC *Allowable Stress Design* (ASD) *Steel Construction Manual* (1989) and the 1st edition of the AISC *Load and Resistance Factor Design* (LRFD) *Steel Construction Manual* (1986). The LRFD version of the table was found to produce erroneously large equivalent axial loads and was subsequently updated by Uang et al. (1990); these corrected values were incorporated into the 2nd edition of the AISC LRFD *Manual* (1994). Because column tables in these editions list shallow wide-flange shapes up to W14 shapes, *m* values were only derived for W-shapes up to a nominal depth of 14 in.

The 3rd edition of the AISC LRFD *Manual* (2001) saw the development of Part 6 for members subject to combined loading. This edition of the AISC *Manual* elected to adopt a method of using reciprocal coefficients of *b*, *m*, and *n* developed by Aminmansour (2000):

$$b = \frac{1}{\phi P_n} \tag{1}$$

$$m = \frac{8}{9\phi_b M_{nx}} \tag{2}$$

$$n = \frac{8}{9\phi_b M_{ny}} \tag{3}$$

These factors represent the reciprocal of the axial, major-axis bending, and minor-axis bending design strengths, respectively. Note that the *m* in this method does not relate to the *m* from the equivalent axial load method. It was proposed that an initial trial shape be evaluated by using Table 6-1 of the 3rd edition of the AISC LRFD *Manual*, which included median values of the reciprocals for each depth group (from W4 to W40 shapes). Applicable to shallow shapes and shapes deeper than W14, the proposed method to select a trial shape would be to use either the median *m* or *b* and solve for the required *b* or *m*. There was no formal guidance provided to determine the required depth of shape other than to focus on deep shapes when the moment demands dominate.

In the 13th (2005) and 14th (2011) editions of the unified AISC ASD and LRFD *Steel Construction Manual*, the method for selecting a trial shape by Aminmansour was removed and the tables of reciprocals became Table 6-1, where the reciprocals were renamed *p*, b_x, and b_y. The latest edition, the 15th, of the AISC *Manual* (AISC, 2017) presents a new way of organizing the beam-column design table. In this table, the information from the column design tables (Table 4-1) and beam design tables (Table 3-10) are presented side-by-side in Table 6-2. However, no guidance

Mathew Reynolds, P.Eng., Graduate Student Researcher, Department of Structural Engineering, University of California, San Diego, La Jolla, CA. Email: mpreynol@ucsd.edu (corresponding)

Chia-Ming Uang, PhD, Professor, Department of Structural Engineering, University of California, San Diego, La Jolla, CA. Email: cmu@ucsd.edu.

Paper No. 2018–10

is provided in the *Manual* on the selection of an initial trial beam-column W-shape for design purposes. Designers may resort to other resources—for example, a simplified table of m values for use in the equivalent axial load method in Geschwindner et al. (2017).

SCOPE

Using Table 6-2 in the 15th edition of the AISC *Manual*, it is believed that an updated m table for the equivalent axial load method will provide a straightforward and robust methodology for selecting a candidate wide-flange beam-column. This updated table will also encourage the use of shapes deeper than W14 (i.e., beam-type shapes) for beam-columns through the inclusion of m values up to W36 shapes. This is made possible through inclusion of shapes beyond W14 being tabulated in AISC *Manual* Table 6-2. In addition, for the first time an equation has been developed to guide users on selecting an appropriate depth of W-shaped beam-columns subjected to major-axis bending.

DERIVATION

The design of W-shape beam-columns is covered in AISC *Specification* Section H (2016). The design of beam-columns is governed by one of two interaction equations:

$$\frac{P_r}{P_c}+\frac{8}{9}\left(\frac{M_{rx}}{M_{cx}}+\frac{M_{ry}}{M_{cy}}\right)\le 1.0 \text{ when } \frac{P_r}{P_c}\ge 0.2$$

(*Spec.* Eq. H1-1a)

$$\frac{P_r}{2P_c}+\left(\frac{M_{rx}}{M_{cx}}+\frac{M_{ry}}{M_{cy}}\right)\le 1.0 \text{ when } \frac{P_r}{P_c}< 0.2$$

(*Spec.* Eq. H1-1b)

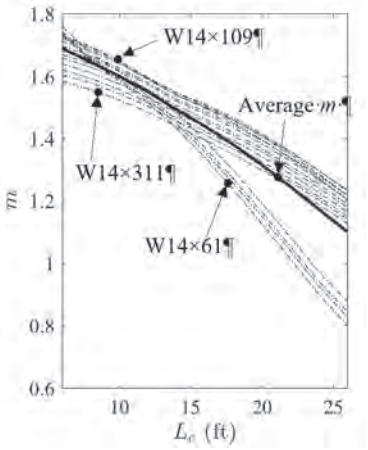

Fig. 1. Values of m *for W14 members.*

The equivalent axial load method rewrites these interaction equations into Equations 4a and 4b.

$$P_{eq}=P_r+mM_{rx}+muM_{ry}\le P_c \text{ when } \frac{P_r}{P_c}\ge 0.2 \quad (4a)$$

$$P_{eq}=\frac{P_r}{2}+\frac{9}{8}mM_{rx}+\frac{9}{8}muM_{ry}\le P_c \text{ when } \frac{P_r}{P_c}< 0.2 \quad (4b)$$

The left-hand side of these equations represents the equivalent axial load, P_{eq}. The coefficients m and u are defined in Equations 5 and 6.

$$m=\frac{\frac{8}{9}P_c}{M_{cx}} \quad (5)$$

$$u=\frac{M_{cx}}{M_{cy}} \quad (6)$$

Because the shapes are assumed to be compact, the design flexural strength in the major and minor directions are governed by AISC *Specification* Sections F2 and F6, respectively. Similarly, the design axial strength is governed by AISC *Specification* Section E3 using the least radius of gyration, r_y. Note that ϕ_c for computing P_c was 0.85 in the 1st edition of the AISC LRFD *Specification*, but was changed to and has remained 0.9 since the 13th edition.

The first step in deriving m values is to compute their value for every W-shape over a range of lengths. The range of W-shapes used for the derivation is limited to those which are classified as compact for F_y equal to 50 ksi. The values of m are then averaged across each nominal depth increment to provide an average m for each depth. For example, the m value for the W14 group is averaged across all weights between W14×61 to W14×311 (see Figure 1). Table 1 shows the computed values of m when the moment gradient adjustment factor for lateral-torsional buckling (LTB), C_b, is equal to 1.0. Table 2 shows another set of m values based on the major-axis flexural strength reaching the nominal plastic moment, a condition that is a function of L_b and C_b values. This condition is automatically satisfied in the plastic LTB region—that is, $L_b \le L_p$. In the inelastic LTB region—that is, $L_b < L_p < L_r$, C_b needs to be sufficiently large ($C_b = 1$ at $L_b = L_p$ and $C_b = 1.43$ at $L_b = L_r$). An even larger value of C_b (>1.43) is required to satisfy this condition in the elastic LTB region ($L_b > L_r$). Table 2 shows in light gray the values that are different from those in Table 1. Values in either table assume a yield stress equal to 50 ksi. In lieu of providing additional tables, it is found that the increase to 65 ksi yield stress results in an approximate reduction factor of 0.95 to these values.

Unless limited by factors like architectural limitations, choosing the nominal shape depth of an economical

Table 1. Values of m and u (F_y = 50 ksi[a] for C_b = 1.0)										
	Values of m									Values of u
L_c (ft)	8	10	12	14	16	18	20	22	24+	
W8	2.7	2.5	2.3	2	1.8	1.6	1.3	1.2	1	2.3
W10	2.2	2.1	2	1.9	1.8	1.6	1.4	1.3	1.2	2.3
W12	1.9	1.8	1.7	1.7	1.6	1.5	1.4	1.3	1.2	2.3
W14	1.6	1.6	1.5	1.5	1.4	1.4	1.3	1.2	1.2	2.3
W16	1.4	1.4	1.3	1.2	1.1	1	0.9	0.9	0.8	4.1
W18	1.3	1.2	1.2	1.1	1	1	0.9	0.8	0.7	4.1
W21	1.1	1.1	1	1	1	0.9	0.8	0.8	0.7	4.3
W24	1	1	0.9	0.9	0.9	0.8	0.8	0.7	0.7	4.4
W27	0.9	0.9	0.8	0.8	0.8	0.8	0.7	0.7	0.7	4.6
W30	0.8	0.8	0.8	0.8	0.7	0.7	0.7	0.7	0.6	4.8
W33	0.8	0.7	0.7	0.7	0.7	0.7	0.6	0.6	0.6	5.1
W36	0.7	0.7	0.7	0.6	0.6	0.6	0.6	0.5	0.5	6.1

[a] For F_y = 65 ksi, multiply m value by 0.95.

Table 2. Values of m and u for High Moment Gradient (F_y = 50 ksi, $M_{cx} = M_p$)[a]										
	Values of m									Values of u
L_c (ft)	8	10	12	14	16	18	20	22	24+	
W8	2.6	2.3	2.1	1.8	1.5	1.3	1	0.9	0.7	2.3
W10	2.2	2.1	1.9	1.7	1.6	1.4	1.2	1	0.9	2.3
W12	1.9	1.8	1.7	1.6	1.5	1.4	1.3	1.2	1	2.3
W14	1.6	1.6	1.5	1.5	1.4	1.3	1.2	1.1	1	2.3
W16	1.4	1.3	1.2	1	0.9	0.8	0.7	0.6	0.5	4.1
W18	1.3	1.2	1.1	1	0.9	0.8	0.7	0.6	0.6	4.1
W21	1.1	1.1	1	0.9	0.9	0.8	0.7	0.6	0.6	4.3
W24	1	1	0.9	0.9	0.8	0.7	0.7	0.6	0.6	4.4
W27	0.9	0.9	0.8	0.8	0.8	0.7	0.7	0.6	0.6	4.6
W30	0.8	0.8	0.8	0.7	0.7	0.7	0.6	0.6	0.5	4.8
W33	0.8	0.7	0.7	0.7	0.6	0.6	0.6	0.5	0.5	5.1
W36	0.7	0.7	0.7	0.6	0.6	0.5	0.5	0.5	0.4	6.1

[a] For convenience, values different from Table 1 are shown in gray.

beam-column is not straightforward. Previous editions of the m table have included first approximation values that would assist in choosing a nominal depth range. Based on the nominal shape depth of the first trial shape, the user then can update the equivalent axial load based on the subsequent approximation m values for an improved shape. This approach may result in conservative designs as the efficiency of moving to a deeper shape when under the influence of relatively high moment may not be realized unless the designer checks many different shapes. This effect can readily be observed by comparing the gradient of the equivalent axial load for a given set of required axial load and moment as one selects incrementally deeper shapes. For example, consider a 16-ft-long beam-column subjected to an axial load of 500 kips and a major-axis bending moment of 700 kip-ft. Using Table 1, P_{eq} equals 1,480 kips when considering a W14 shape compared to 1,060 kips when considering a W27 shape. A decrease of 30% of equivalent axial load is realized by moving to a deeper W-shape.

Instead of suggesting a first approximation for the value

of m, an approximate depth of shape can be computed from Equation 7, which has been derived based on curve-fitting randomly generated design scenarios compared with the most efficient W-shape as determined from an exhaustive analysis. The exhaustive analysis determines the most efficient wide-flange shape after performing the appropriate axial and bending interaction check using AISC *Specification* Equation H1-1a or H1-1b on every shape in the AISC W-shape database.

$$D = 1.2\sqrt[4]{P_u L_c} + 1.1\sqrt[4]{M_u L_c} + \frac{\sqrt{P_u M_u}}{3L_c^2} \quad (7)$$

where the units of M_u and P_u are in kip-ft and kips, L_c in ft, and D in inches.

The first term, $1.2\sqrt[4]{P_u L_c}$, represents the most efficient depth of column for a given axial load and length. The second term, $1.1\sqrt[4]{M_u L_c}$, represents the additional depth required for a given major-axis flexural demand. The last term is a correction factor that dominates for shorter columns with lengths less than 14 ft. Considering the preceding example, the estimated depth as computed using Equation 7 is 23.4 in. Therefore, the closest depth available of 24 in. can be chosen for a trial W-shape. The most efficient W-shape, determined by exhaustive analysis, is a W24×131. This step (using Equation 7) is only required if the designer has no other considerations on the depth of the shape.

Limitations

The key limitation to the values of m presented in Tables 1 and 2 is the assumption that the unbraced length for bending, L_b, is equal to the effective length of the column for minor-axis buckling. Two common situations where this limitation is violated are:

1. The beam-column has some end fixity or minor-axis bracing.
2. The major-axis flexural buckling governs such that $L_{cy\ eq} > L_{cy}$, where $L_{cy\ eq}$ represents the equivalent length in the minor-axis as determined using AISC *Manual* Equation 4–1 (2017), $L_{cy\ eq} = L_{cx}/(r_x/r_y)$.

In both situations, it is recommended to conservatively use the unbraced length for bending as the length to use with the m table to start the design process. More iterations using AISC *Specification* Equation H1-1a or H1-1b may be required to accurately account for these effects.

Second-Order and Biaxial Bending Considerations

Beam-columns may be subject to second-order amplification of the applied moments. Using B_1 and B_2 from the approximate second-order analysis in AISC *Specification* Appendix 8 results in an iterative procedure because the amplification of flexural demands depends on the flexural stiffness. Some designers suggest that a value of B_1 equal to 1.1 be chosen for trial selection for sidesway inhibited beam-columns. This value is found to be adequate for conservative estimation for beam-columns of moderate length. As a design aid, a similar procedure that was used to develop m values was implemented to develop approximate B_1 values for the amplification of major-axis flexural demands. To derive the B_1 value, Equation 8 was used by assuming a factored axial load of $0.25A_gF_y$:

$$B_1 = \frac{C_m}{1 - \frac{P_r}{P_{el}}} \quad (8)$$

where C_m is the equivalent uniform moment factor, and P_{el} is the elastic critical buckling strength in the plane of bending. The values of B_1 are then averaged across each nominal W-shape depth group (see Figure 2). Figure 3 shows the variation of B_1 for major-axis bending for each nominal depth group. For second-order amplification of sway effects or minor-axis bending, arbitrary values of B_1 and B_2 should be chosen based on experience.

For a beam-column with biaxial bending, a conversion factor, u, between minor- and major-axis design flexural strengths is required (see Equations 4 and 6). Previous editions of the AISC *Manual* included a single value of u in the column design table based on the ratio of plastic moment capacities. A similar procedure was used for the development of the B_1 design aid was implemented to produce values of u for each depth group for a range of lengths (see Figure 4). Note that the influence of length arises from the length dependence of major-axis LTB strength. The last column in Tables 1 and 2 shows the recommended u value for each nominal depth group; other than providing a complex

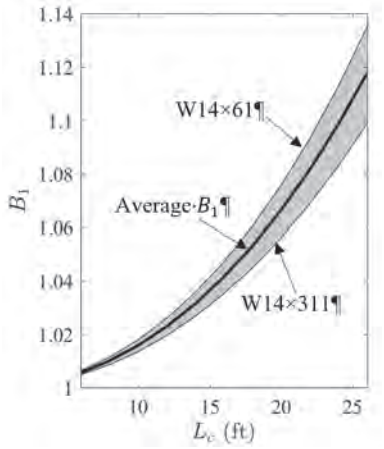

Fig. 2. B_1 *for W14 members (major axis).*

equation to reflect the dependence of member length, the recommended u value is based on the major-axis plastic moment for M_{cx}.

RECOMMENDED DESIGN PROCEDURE

1. For a given L_c, select an appropriate value of m from Table 1 (for C_b close to 1.0) or Table 2 (for C_b between 1.5 and 2.0). If the nominal depth of the shape is not predetermined, use Equation 7 to estimate a shape depth. Select or determine B_1 (Figure 2) and u (Tables 1 and 2 or Figure 4) if there is biaxial bending.
2. Calculate the equivalent axial load, $P_{eq} = P_r + mM_{rx} + muM_{ry}$. Use the first-order flexural demands and estimated values of B_1 and B_2 to calculate M_{rx} and M_{ry}.
3. If $P_r/P_{eq} < 0.2$, modify the equivalent axial load as $P_{eq} = \frac{P_r}{2} + \frac{9}{8}mM_{rx} + \frac{9}{8}muM_{ry}$.
4. Select a candidate shape from AISC *Manual* Table 6-2. Alternatively, AISC *Manual* Table 4-1 may be used for W-shapes with a nominal depth no greater than 14 in. If an efficient candidate shape cannot be found within the selected nominal depth group, move to step 5. Otherwise, proceed to step 6.
5. Consider shapes of the lesser or greater nominal depth group, and select new m, B_1, and u values. Repeat steps 2 through 4.
6. Verify the adequacy of the W-shape using the AISC *Specification* interaction Equations H1-1a or H1-b. This is easily performed using AISC *Manual* Table 6-2, which lists the design axial and flexural strength of each shape. If the shape does not satisfy the interaction formula or more efficiency is sought, additional iterations may be performed.

Several representative examples are included in the Appendix to illustrate the efficiency of the design procedure.

VALIDATION

To test the values contained in Tables 1 and 2, a design heuristic was programmed to compare the W-shape determined from the equivalent axial load method to the most efficient W-shape as determined from exhaustive analysis. The heuristic uses the depth estimate from Equation 7 to select the closest applicable nominal depth for initial shape selection. If the heuristic fails to determine a W-shape with a demand-capacity ratio (DCR) between 0.85 and 1.0 (see Equation 9) within the first nominal depth group selected, then the heuristic is permitted one additional adjacent nominal depth group for candidate selection. This DCR range was chosen to represent an adequate level of efficiency a designer might use in selecting a beam-column shape. The heuristic uses AISC *Manual* Table 6-2 to determine P_c. A tabulated version of Figure 3 is provided to the heuristic for an initial estimate of B_1. The error in the equivalent axial load method is then determined by comparing the weight of the shape as determined from the design heuristic and the most efficient shape determined by exhaustive analysis (see Equation 10).

$$DCR = \frac{P_{eq}}{P_c} \tag{9}$$

$$Error = \frac{W_{eq} - W_{act}}{W_{act}} \tag{10}$$

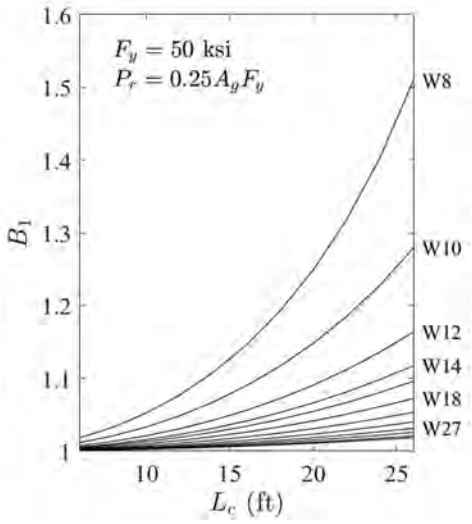

Fig. 3. Value of B_1 *(major-axis bending).*

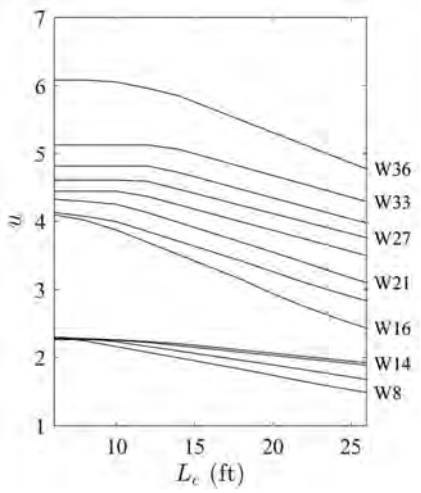

Fig. 4. Value of u.

where W_{eq} is the unit weight of the shape determined using the equivalent axial load method, and W_{act} is the unit weight of the most efficient shape for the given force demands.

Figure 5 shows the probability density function (PDF) of the error obtained after performing 10,000 randomly generated uniaxial design scenarios. The mean error was equal to +0.5%. Integrating the PDF results in a 90% probability of selecting a shape within 5% of the most efficient shape in terms of unit weight. Additionally, it was found that 77% of the time the shape was selected from the first nominal depth based on Equation 7. Otherwise, it was found to be within one adjacent group.

CONCLUSION

The equivalent axial load method consists of converting the minor- and major-axis bending moments into an equivalent axial load for adding to the applied axial load that a designer can use to compare against tabulated design axial strengths. This methodology simplifies the candidate selection of beam-columns by reducing the number of iterations a designer needs to perform while using the tabulated design values found in the AISC *Steel Construction Manual*. To use the method, a designer uses values of *m* found in Tables 1 or 2, which have been tabulated beyond shapes of 14-in. nominal depths. This updated and expanded *m* table in combination with AISC *Manual* Table 6-2 provides a powerful methodology in selecting candidate W-shapes. Once a candidate shape is selected, the governing interaction equation can be verified using AISC *Manual* Table 6-2. Potential inefficiencies are avoided by using Equation 7 to select the appropriate trial depth, which encourages the use of deeper and more efficient W-shapes for bending dominated beam-columns. Simplified *u* factors are provided in Tables 1 and 2 that can be used for biaxial bending design problems.

APPENDIX

Example 1. Select an economical W12 shape for a member with minor-axis effective length and unbraced beam length equal to 12 ft. The factored axial load and moments calculated from a first-order structural analysis are given as $P_u = 200$ kips, $M_{u1} = 100$ kip-ft, and $M_{u2} = -200$ kip-ft, where M_{u1} and M_{u2} are the major-axis moments at member ends. The negative sign of M_{u2} represents reverse-curvature bending. Assume minor-axis bending is negligible.

Solution:

1. Select $m = 17$ from Table 2. Because $C_m = 0.6 - 0.4(M_1/M_2) = 0.4$, we assume $B_1 = 1.0$ (Equation 8).

2. Calculate the equivalent axial load:

$$P_{eq} = P_r + mM_{rx} + muM_{ry} \le P_c \tag{4a}$$
$$= 200 \text{ kips} + 1.7(200 \text{ kip-ft})$$
$$= 500 \text{ kips}$$

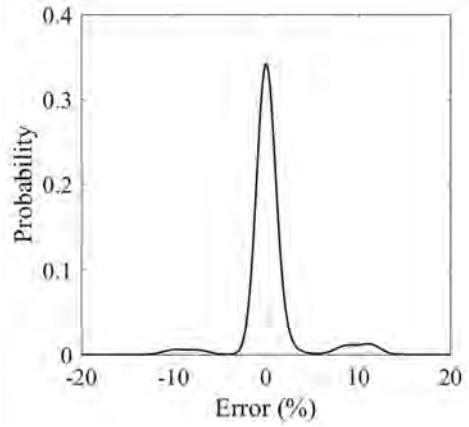

Fig. 5. Probability distribution of percentage error of the equivalent axial load method.

3. Because P_r/P_{eq} = 200 kips/500 kips = 0.4000 ≥ 0.2, the assumption of using Equation 4a was correct and no changes are required.

4. Using AISC *Manual* Table 6-2, select a W12×53 as the most economical shape with $\phi_c P_n$ = 549 kips.

5. No revision is required because an appropriate shape was found.

6. Check the appropriate interaction using AISC *Specification* Equation H1-1a and AISC *Manual* Table 6-2. Note that the moment gradient gives C_b = 217, which results in $\phi_b M_{nx}$ = 292 kip-ft (for L_b = 0 ft) rather than the value listed for L_b = 12 ft.

$$\frac{P_r}{P_c}+\frac{8}{9}\left(\frac{M_{rx}}{M_{cx}}+\frac{M_{ry}}{M_{cy}}\right)\le 1.0 \text{ when } \frac{P_r}{P_c}\ge 0.2 \qquad \text{(}Spec\text{. Eq. H1-1a)}$$

$$\frac{200 \text{ kips}}{549 \text{ kips}}+\frac{8}{9}\left(\frac{200 \text{ kip-ft}}{292 \text{ kip-ft}}\right)=0.97<1.0 \qquad \textbf{o.k.}$$

Example 2. Select an economical W-shape for an 18-ft-long member in a braced frame assuming pinned end connections. The factored axial loads and moment calculated from a first-order structural analysis are given as P_u = 600 kips and M_u = 350 kip-ft due to a transverse loading. Assume minor-axis bending is negligible and C_b = 10.

Solution:

1. Use the first two terms of Equation 7 to estimate the depth (the third term is small for L_c > 12 ft).

$$1.2\sqrt[4]{P_u L_c}+1.1\sqrt[4]{M_u L_c}=22.0 \text{ in.} \qquad \text{(from Eq. 7)}$$

Select the W21 group as the first estimate, and select m = 0.9 from Table 1. Because C_m = 10, the value of B_1 may be determined from Figure 3 as 1.03.

2. Calculate the equivalent axial load:

$$\begin{aligned} P_{eq} &= P_r + mM_{rx} + muM_{ry} \le P_c \qquad \text{(4a)}\\ &= 600 \text{ kips} + 0.9\left[350 \text{ kip-ft}(1.03)\right]\\ &= 924 \text{ kips}\end{aligned}$$

3. Because P_r/P_{eq} = 600 kips/924 kips = 0.650 ≥ 0.2, the assumption of using Equation 4a was correct and no changes are required.

4. Using AISC *Manual* Table 6-2, select a W21×111 as the most economical shape with $\phi_c P_n$ = 978 kips.

6. Check the appropriate interaction using AISC *Specification* Equation H1-1a and AISC *Manual* Table 6-2. The actual B_1 value is determined to be 1.04.

$$\frac{P_r}{P_c}+\frac{8}{9}\left(\frac{M_{rx}}{M_{cx}}+\frac{M_{ry}}{M_{cy}}\right)\le 1.0 \text{ when } \frac{P_r}{P_c}\ge 0.2 \qquad \text{(}Spec\text{. Eq. H1-1a)}$$

$$\frac{600 \text{ kips}}{978 \text{ kips}}+\frac{8}{9}\left[\frac{350 \text{ kip-ft (1.04)}}{901 \text{ kip-ft}}\right]=0.97<1.0 \qquad \textbf{o.k.}$$

Note: If the designer had chosen a W24 section in Step 1, the resulting P_{eq} would have been 888 kips, which would have permitted the selection of the slender W24×104 shape because AISC *Manual* Table 6-2 already includes the reduction for effective widths of slender elements. Checking the interaction formula of this shape results in a DCR of 1.00; either shape is a valid selection.

Example 3. Select an economical shape for a member with the major- and minor-axis effective lengths and unbraced length equal to 18 ft. The factored axial load and moments calculated from a first-order structural analysis are given as P_u = 1,150 kips, M_{u1} = 760 kip-ft, and M_{u2} = –760 kip-ft, where M_{u1} and M_{u2} are the major-axis moments at member ends. Assume minor-axis bending is negligible.

Solution:

1. Use the first two terms of Equation 7 to estimate the depth (third term is small for $L_c > 12$ ft).

$$1.2\sqrt[4]{P_u L_c} + 1.1\sqrt[4]{M_u L_c} = 26.3 \text{ in.} \quad \text{(from Eq. 7)}$$

The value of C_b is expected to be large because the member is bent in double curvature. Therefore, select m as 0.7 from Table 2, assuming a nominal depth of 27 in. Because $C_m = 0.6 - 0.4(M_1/M_2) = 0.2$, determine $B_1 = 1.0$ using Equation 8.

2. Calculate the equivalent axial load:

$$\begin{aligned} P_{eq} &= P_r + mM_{rx} + muM_{ry} \le P_c \quad \text{(4a)} \\ &= 1{,}150 \text{ kips} + 0.7(760 \text{ kip-ft}) \\ &= 1{,}680 \text{ kips} \end{aligned}$$

3. Because $P_r/P_{eq} \ge 0.2$, the assumption of using Equation 4a was correct and no changes are required.

4. Using AISC *Manual* Table 6-2, select a W27×178 as the most economical shape with $\phi_c P_n = 1{,}710$ kips.

5. No revision is required because an appropriate shape was found.

6. Check the appropriate interaction using AISC *Specification* Equation H1–1a and AISC *Manual* Table 6-2. Note that the moment gradient gives $C_b = 2.3$, which results in $\phi_b M_{nx} = 2{,}140$ kip-ft (for $L_b = 0$ ft) rather than the value listed for $L_b = 18$ ft.

$$\frac{P_r}{P_c} + \frac{8}{9}\left(\frac{M_{rx}}{M_{cx}} + \frac{M_{ry}}{M_{cy}}\right) \le 1.0 \text{ when } \frac{P_r}{P_c} \ge 0.2 \quad \text{(}\textit{Spec.}\text{ Eq. H1-1a)}$$

$$\frac{1{,}150 \text{ kips}}{1{,}710 \text{ kips}} + \frac{8}{9}\left(\frac{760 \text{ kip-ft}}{2{,}140 \text{ kip-ft}}\right) = 0.99 < 1.0 \quad \textbf{o.k.}$$

Example 4. Select an economical W12 shape for a 20-ft-long member in a braced frame. The effective length factor, K, is assumed to be 1.0 in both directions. The factored axial load and moments calculated from a first-order structural analysis are given as $P_u = 400$ kips, $M_{u1} = 200$ kip-ft, and $M_{u2} = 200$ kip-ft, where M_{u1} and M_{u2} are the major-axis moments at member ends. Assume a minor-axis bending moment of $M_{uy} = 50$ kip-ft due to the application of a transverse load.

Solution:

1. Select $m = 1.4$ from Table 1. Because $C_m = 10$, the value of B_1 for major-axis bending may be determined from Figure 3 as 1.09. The value of u is determined to be 2.0 from Figure 4. The value of B_1 for minor-axis bending is assumed to be 1.3.

2. Calculate the equivalent axial load:

$$\begin{aligned} P_{eq} &= P_r + mM_{rx} + muM_{ry} \le P_c \quad \text{(4a)} \\ &= 400 \text{ kips} + 1.4\left[200 \text{ kip-ft}(1.09) + 50 \text{ kip-ft}(2.0)(1.3)\right] \\ &= 887 \text{ kips} \end{aligned}$$

3. Because $P_r/P_{eq} \ge 0.2$, the assumption of using Equation 4a was correct and no changes are required.

4. Using AISC *Manual* Table 6-2, select a W12×106 as the most economical shape with $\phi_c P_n = 908$ kips.

6. Check the appropriate interaction using AISC *Manual* Table 6-2. The actual major- and minor-axis values of B_1 are 1.09 and 1.37, respectively. C_b is equal to 1.0.

$$\frac{P_r}{P_c} + \frac{8}{9}\left(\frac{M_{rx}}{M_{cx}} + \frac{M_{ry}}{M_{cy}}\right) \le 1.0 \text{ when } \frac{P_r}{P_c} \ge 0.2 \quad \text{(}\textit{Spec.}\text{ Eq. H1-1a)}$$

$$\frac{400 \text{ kips}}{908 \text{ kips}} + \frac{8}{9}\left(\frac{200 \text{ kip-ft}(1.09)}{562 \text{ kip-ft}} + \frac{50 \text{ kip-ft}(1.37)}{282 \text{ kip-ft}}\right) = 1.0 \le 1.0 \quad \textbf{o.k.}$$

Note: If the designer had instead used $u = 23$ from Table 1, the equivalent axial load, P_{eq}, would be equal to 915 kips. Because this is marginally greater than $\phi_c P_n$ of W12×106 at 20 ft, the designer may elect to initially choose a W12×120 instead, but expect a DCR of approximately 0.89 (determined as 915 kips/1,030 kips). The actual DCR for the W12×120 is found to be 0.87 after checking the interaction formula using AISC *Specification* Eq. H1–1a.

REFERENCES

AISC (1986), *Load and Resistance Factor Design Manual of Steel Construction*, 1st Ed., American Institute of Steel Construction, Chicago, Ill.

AISC (1989), *Allowable Stress Design Manual of Steel Construction*, 9th Ed., American Institute of Steel Construction, Chicago, Ill.

AISC (1994), *Load and Resistance Factor Design Manual of Steel Construction*, 2nd Ed., American Institute of Steel Construction, Chicago, Ill.

AISC (2001), *Load and Resistance Factor Design Manual of Steel Construction*, 3rd Ed., American Institute of Steel Construction, Chicago, Ill.

AISC (2005), *Steel Construction Manual*, 13th Ed., American Institute of Steel Construction, Chicago, Ill.

AISC (2011), *Steel Construction Manual*, 14th Ed., American Institute of Steel Construction, Chicago, Ill.

AISC (2016), *Specification for Structural Steel Buildings*, ANSI/AISC 360–16, American Institute of Steel Construction, Chicago, Ill.

AISC (2017), *Steel Construction Manual*, 15th Ed., American Institute of Steel Construction, Chicago, Ill.

Aminmansour, A. (2000), "A New Approach for Design of Steel Beam-Columns," *Engineering Journal*, AISC, Vol. 37, No. 2, pp. 41–72.

Burgett, L.B. (1973), "Selection of a Trial Column Section," *Engineering Journal*, AISC, Vol. 10, No. 2, pp. 56–60.

Geschwindner, L.F., Liu, J., and Carter, C.J. (2017), *Unified Design of Steel Structures*, 3rd Ed., North Charleston, S.C.

Uang, C-M., Wattar, S.W., and Leet, K.M. (1990), "Proposed Revision of the Equivalent Axial Load Method for LRFD Steel and Composite Beam-Column Design," *Engineering Journal*, AISC, Vol. 27, No.4, pp.150–157.

Walking-Induced Vibration of Steel-Framed Floors Supporting Sensitive Equipment

BRAD DAVIS and DI LIU

ABSTRACT

This paper explains the vibration evaluation methods for floors supporting sensitive equipment in the second edition of AISC Design Guide 11, *Vibrations of Steel-Framed Structural Systems Due to Human Activity*. It presents new experimentally verified equations that are simplified for practical implementation. Sensitive equipment tolerance limits are stated in numerous forms, including peak acceleration and various spectral acceleration and velocity. For this reason, response predictions are given in terms of all tolerance limit forms that are commonly used. The most severe responses of lower frequency floors to walking are due to resonant buildups, whereas the most severe responses of higher frequency floors are due to a series of individual footstep impulses; equations are given for both. Because the sensitive equipment tolerance limit is objective, each equation includes a calibration factor that results in a high probability that the predicted response will exceed the actual response.

Keywords: vibration, serviceability, floors, sensitive equipment.

INTRODUCTION

Steel-framed floors commonly support vibration-sensitive equipment in hospitals, laboratories, and other modern facilities. Sensitive equipment vibration tolerance limits are usually stringent, so walking vibration serviceability often requires much larger member sizes than those required for strength, deflection, or human comfort, even in quiet areas such as offices or residences. The consequence of objectionable vibration usually involves expensive and difficult retrofit solutions. The consequence of an overdesign is excessive steel tonnage. Thus, it is important that engineers have access to prediction methods that are accurate and have known levels of conservatism.

Until 2016, vibrations of floors supporting sensitive equipment had been evaluated using the American Institute of Steel Construction (AISC) Design Guide 11, *Floor Vibration Due to Human Activity* (Murray et al., 1997) Chapter 6, which is based on an approach suggested by Ungar and White (1979).

In recent years, updated response prediction methods have been developed (Young and Willford, 2001; Willford et al., 2007a, 2007b) and specialized by the writers for floors supporting sensitive equipment (Liu and Davis, 2015; Liu, 2015). These updated methods are the basis of Chapter 6 of the second edition of Design Guide 11 *Vibrations of Steel-Framed Structural Systems Due to Human Activity* (Murray et al., 2016). The purpose of this paper is to explain the methods and their design implementation.

The paper is organized into the following sections:

- Tolerance limits for vibration-sensitive equipment
- Prediction of modal properties
- Forces due to walking
- Prediction of resonant responses
- Prediction of impulse responses
- Response prediction
- Commentary on first and second editions of AISC Design Guide 11, Chapter 6
- Conclusions

TOLERANCE LIMITS FOR VIBRATION-SENSITIVE EQUIPMENT

Equipment manufacturers provide specific tolerance limits in terms of various vibration measures, for example, waveform peak acceleration, narrowband spectral acceleration, and one-third octave spectral velocity. An example of measured response to walking, showing the acceleration waveform, narrowband acceleration spectrum, and one-third octave velocity spectrum, is in Figure 1. Such specific limits should be used when possible.

Brad Davis, PhD, SE, Associate Professor, Department of Civil Engineering, University of Kentucky, Lexington, KY. Email: dbraddavis@uky.edu (corresponding)

Di Liu, Associate, Liftech Consultants Incorporated, Oakland, CA. Email: dliu@liftech.net

Paper No. 2018–13

Spectral limits can be converted from displacement to velocity or from velocity to acceleration by multiplying by $2\pi f$, where f is the frequency. For example, if the velocity limit at 8 Hz is 3000 μin./sec (mips), then the corresponding acceleration limit at 8 Hz is 0.151 in./sec^2 = 0.0391%*g*.

Most spectral limits are in terms of root-mean-square (RMS) accelerations or velocities, but occasionally they are in terms of peak quantities. A peak spectral limit is converted to RMS by multiplying by 0.7071. Often, the type of spectrum, peak versus RMS, is not clear; in such cases, the equipment manufacturer should be contacted.

If the type, but not model, of equipment has been identified, or if the manufacturer does not provide a specific limit, then generic tolerance limits should be used. The most common generic limits are the vibration criterion (VC) curves (Ungar et al., 2006) that are the basis of AISC Design Guide 11, Table 6-2, and are stated in terms of RMS velocity in one-third octave bands of frequency.

Tolerance limits for sensitive equipment are usually considered definitive. "Failure" of the floor vibration limit state for sensitive equipment is considered to correspond to equipment malfunction. Equipment manufacturers often require site surveys in which actual velocity levels are compared to the tolerance limit. When the measured values exceed the limit, difficult and expensive retrofit solutions are usually required. Thus, in the following sections, the objective is to predict the vibration magnitudes that will be measured by the site surveyor, and a calibration factor is included to ensure a low probability that the measured values will exceed the ones predicted during design.

PREDICTION OF MODAL PROPERTIES

Fundamental modal properties can be determined using the following equations that are suitable for manual calculations, finite element analysis, or other rational methods.

For typical rectangular floor bays with approximately uniformly distributed mass, the fundamental natural frequency, f_n, can be computed using the following equation. Its predictions are accurate according to Pabian et al. (2013),

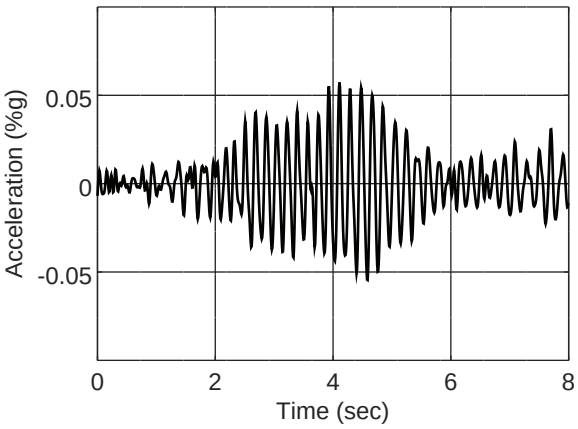

(a) waveform

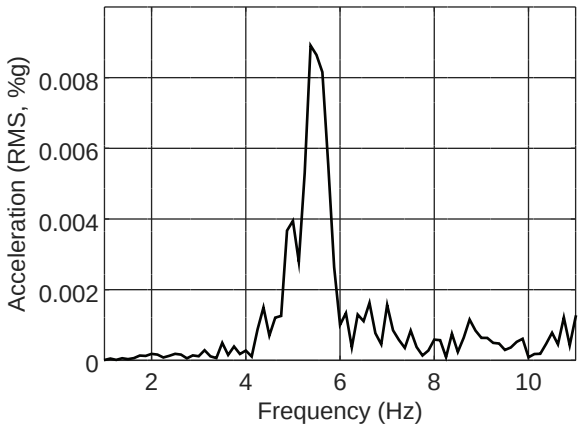

(b) narrowband acceleration spectrum

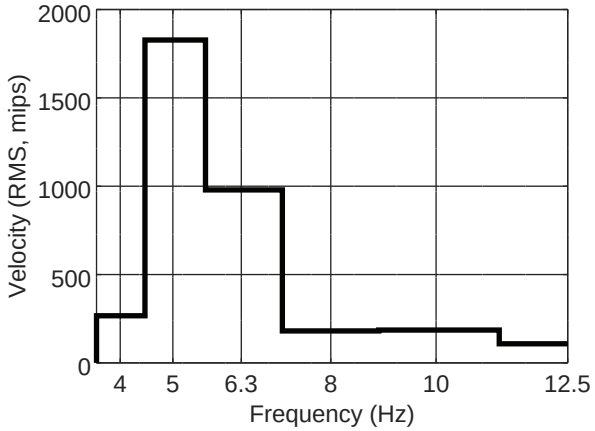

(c) one-third octave velocity spectrum

Fig. 1. Example measured vibration due to walking.

and it is similar to the equation in the British Steel Construction Institute's P354 publication (Smith et al., 2009).

$$f_n = \min(f_b, f_g) \tag{1}$$

where f_b and f_g are the beam and girder natural frequencies from AISC Design Guide 11, Chapter 3.

The effective weight, W, of the fundamental mode can be computed using the following equation from AISC Design Guide 11 Chapter 4. W is double the weight of the effective mass, M_{eff} for load and acceleration at mid-bay (Allen and Murray, 1993).

$$W = \frac{\Delta_b}{\Delta_b + \Delta_g} W_b + \frac{\Delta_g}{\Delta_b + \Delta_g} W_g \tag{2}$$

where

Δ_b, Δ_g = beam and girder mode deflections (AISC Design Guide 11, Chapter 3)

W_b, W_g = beam and girder mode effective weights (AISC Design Guide 11, Chapter 4)

Often, the equipment or walker (or both) is away from mid-bay. This is considered in the Response Prediction section by scaling the mid-bay response by the ratio of the mode shape values.

For typical rectangular bays, the mode shape can be estimated as follows. If the beam natural frequency is lower than the girder natural frequency, then the mode shape is assumed to be the beam bending mode shown in Figure 2. In this assumed shape, the beam deflection is in a half sine wave pattern, with a maximum value of 1.0 at mid-bay. Perpendicular to the beams, the mode shape is assumed to be a half sine wave that extends to the edges of the adjacent bays. If the girder natural frequency is lower than the beam natural frequency, the mode shape is assumed to be a girder bending mode, which is similar to Figure 2 except that the half-sine wave parallel to the girders has a length of L_g. Equation 3 can be used to compute the mode shape value, ϕ, at the equipment or walker location. The equations can be adjusted for other boundary conditions or framing arrangements (e.g., significantly different girder lengths), based on engineering judgment.

Alternatively, the natural frequencies and mode shapes can be predicted using finite element analysis per AISC Design Guide 11, Chapter 7.

The viscous damping ratio, β, is estimated using AISC Design Guide 11, Chapter 4. The damping ratio varies from approximately 0.02 for laboratory floors with ceiling below but no partitions to 0.05 for floor bays with significant full-height partitions. It should be noted that the suggested damping ratios may differ considerably from the actual ones. Because the predicted response depends on β, there is considerable uncertainty in the prediction.

$$\phi = \sin\frac{\pi x}{L_b} \sin\frac{\pi (y + L_g)}{3L_g} \text{ if } f_b \le f_g \tag{3a}$$

$$\phi = \sin\frac{\pi (x + L_b)}{3L_b} \sin\frac{\pi y}{L_g} \text{ if } f_b > f_g \tag{3b}$$

FORCES DUE TO WALKING

For sensitive equipment evaluations, AISC Design Guide 11 defines four walking speeds: very slow, slow, moderate, and fast. Very slow walking applies in areas with short walking paths, such as a medical imaging control room or a small laboratory. For this category, the walking path is too short for a series of nearly identical footsteps that might cause a resonant buildup. Fast walking applies in areas, such as corridors, that do not limit the speed of walking. Slow and moderate walking are intermediate categories that can be used based on judgment. Table 1 indicates the step frequencies for these categories. The minimum frequency of slow walking, 1.5 Hz, is near the lower end of regular step frequencies listed in AISC Design Guide 11, Chapter 1. Similarly, the maximum frequency of fast walking is at the higher end of regular step frequencies, 2.2 Hz. The boundaries between slow and moderate walking, and moderate and fast walking, are approximately at the one-third points between 1.5 Hz and 2.2 Hz.

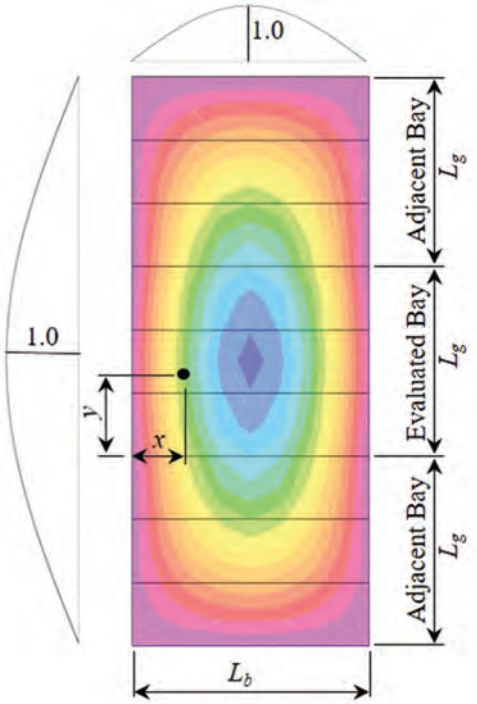

Fig. 2. Beam bending mode shape.

Table 1. Step Frequencies		
Category	**Range (Hz)**	**Mid-Range (Hz)**
Very slow	1.0–1.5	1.25
Slow	1.5–1.7	1.60
Moderate	1.7–2.0	1.85
Fast	2.0–2.2	2.10

Forces due to walking have been measured by various researchers. The measurements by Rainer et al. (1988) and Kerr (1998) have been influential in North American (Murray et al., 1997; Murray et al., 2016; NRCC, 2010) and European (Willford and Young, 2006; Smith et al., 2009) design guides. The footstep forces used for sensitive equipment in AISC Design Guide 11 are based on the database of more than 800 measurements by Kerr and others, reported in Willford et al. (2007a; 2007b).

Fourier Series

For the purpose of computing resonant responses due to walking, the walking force, $F(t)$, is represented by the following Fourier series limited to four harmonics.

$$F(t) = \sum_{i=1}^{4} \alpha_i Q \sin(2\pi i f_{step} t - \phi_i) \quad (4)$$

where

Q = reference bodyweight, lb
f_{step} = step frequency, Hz
t = time, sec
α_i = dynamic coefficient of the ith harmonic
ϕ_i = phase lag of the ith harmonic

The reference bodyweight is 168 lb to be consistent with Willford and Young (2006) and Smith et al. (2009), which use dynamic coefficients similar to those used herein.

The phase lag has extremely high variability. Zivanovic et al. (2007) indicated that measured phase lags varied uniformly from $-\pi$ to π. In the formulations described herein, the phase lag is not required.

Willford et al. (2007a) provided a good summary of dynamic coefficients (called "dynamic load factors" in their paper) measured by several researchers, including Kerr (1998). They plotted the dynamic coefficients for the first four harmonics versus frequency. The plots indicate: (1) the dynamic coefficients vary widely; (2) dynamic coefficients decrease slightly with increasing harmonic number; and (3) for a given harmonic, the dynamic coefficient increases slightly with increasing step frequency. The approximate average dynamic coefficients for the first four harmonics are 0.4, 0.07, 0.06, and 0.05.

The second through fourth harmonic dynamic coefficients at mid-range harmonic frequencies—product of mid-range step frequency from Table 1 and harmonic number—were curve-fit for slow, moderate, and fast walking to facilitate the development of resonant response prediction equations. The curve-fit for slow walking, for example, is in Figure 3. The resulting equation is:

$$\alpha = 0.0985e^{-\gamma f} \quad (5)$$

where

f = frequency, Hz
γ = 0.1, 0.09, and 0.08 for slow, moderate, and fast walking, respectively

Effective Impulse

From basic mechanics, the peak velocity of a mass, M, immediately after an impulse, I, is:

$$v_p = \frac{I}{M} \quad (6)$$

This relationship can be used to compute the peak velocity immediately after a footstep. The walking force is expressed as an effective impulse, I_{eff} in lb-sec, and the mass is the effective mass of the floor bay, M_{eff}, in lb-sec^2/in.

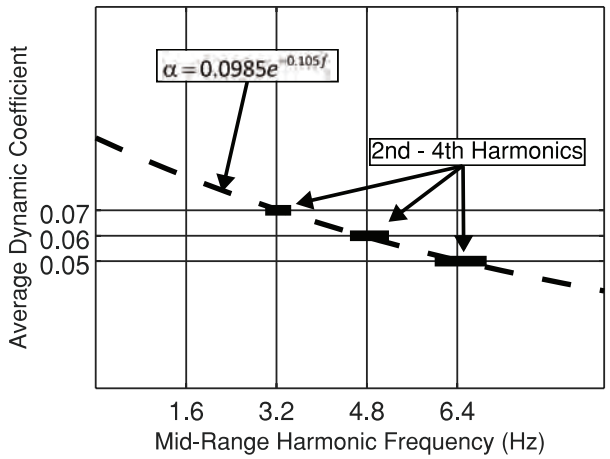

Fig. 3. Example curve-fit of dynamic coefficients.

The following effective impulse was adapted from Young and Willford (2001). They computed peak velocities of analytical representations of floors subjected to 880 measured footstep forces from Kerr (1998). [More information is found in Liu and Davis (2015).] For each case, the effective impulse was the product of the peak velocity and mass. The results indicated that the effective impulse increases as the step frequency increases and decreases as the natural frequency increases. The average effective impulse from their study is:

$$I_{eff} = \frac{f_{step}^{1.43}}{f_n^{1.30}} \frac{Q}{17.8} \tag{7}$$

where f_{step} is the step frequency. For the research described herein, f_{step} is the mid-range frequency from Table 1.

PREDICTION OF RESONANT RESPONSES

According to Rainer et al. (1988), only the "first three or four harmonics comprise the main dynamic components of walking forces." Thus, resonant responses are possible if the natural frequency does not exceed the maximum frequency of the fourth harmonic, which is called f_{4max} in AISC Design Guide 11. For slow walking, the maximum step frequency from Table 1 is 1.7 Hz, so f_{4max} = (1.7 Hz)(4) = 6.8 Hz. Similarly, for moderate and fast walking, respectively, f_{4max} is 8.0 Hz and 8.8 Hz.

Figure 4 is an example resonant response of a floor with a natural frequency of 5.18 Hz, due to walking at 5.18 Hz/3 = 1.73 Hz. The waveform indicates a resonant buildup followed by a short duration of sinusoidal vibration with nearly constant amplitude. According to research by the writers and their colleagues, the average number of footsteps in a resonant buildup is approximately six.

Figure 4(b) indicates very low responses to the first and second harmonics (1.73 Hz and 3.46 Hz) and that the vast majority of the response is due to the third harmonic, which is at the natural frequency—5.18 Hz in this example. Thus, the bay can be idealized as a single degree-of-freedom (SDOF) system with the natural frequency, effective mass, and damping of the bay, subjected to the harmonic force causing resonance. Figure 5 is the computed response to the harmonic, with frequency equaling the natural frequency and a 3-sec resonant buildup, followed by viscous decay.

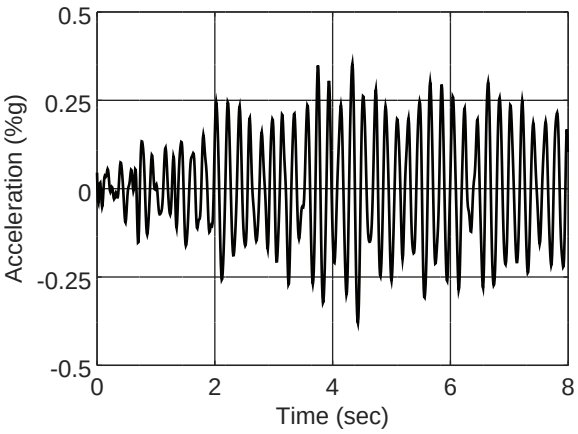

(a) waveform

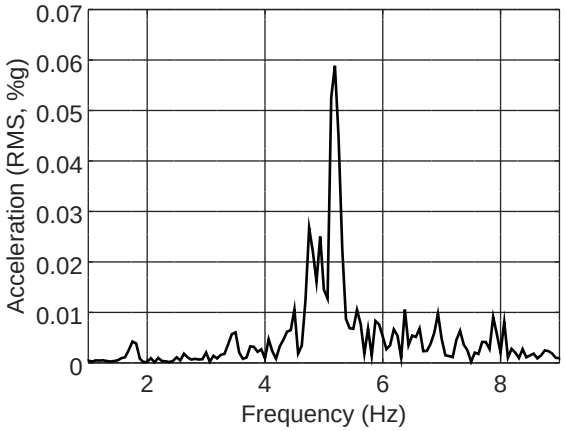

(b) narrowband spectrum

Fig. 4. Example measured resonant response.

Peak Acceleration and Velocity Due to Resonant Response

Using an SDOF idealization, the predicted peak acceleration, a_p, is the product of a calibration factor, R, steady-state acceleration, $a_{SteadyState}$, due to the harmonic force at the natural frequency, and resonant buildup factor, ρ (Liu, 2015), as shown in Equation 8. The steady-state acceleration and resonant buildup factor are computed using classical equations for an SDOF system subjected to a sinusoidal load at resonance (Chopra, 2011; Clough and Penzien, 1993).

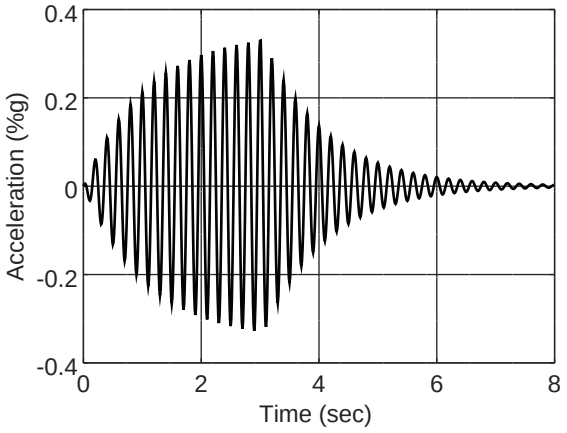

Fig. 5. Example computed response to the harmonic causing resonance.

$$a_p = Ra_{SteadyState} \tag{8}$$
$$= R\frac{\alpha_h Q}{2\beta M_{eff}}(1-e^{-\beta 2\pi f_n T_{BU}})$$

where

R = calibration factor

T_{BU} = duration of resonant buildup, sec

α_h = average dynamic coefficient of the harmonic causing resonance

The effective mass of the fundamental mode, M_{eff}, is half the mass of the effective weight, W, from AISC Design Guide 11, Chapter 4 (Murray et al., 1997). Note that this effective mass applies when the load and acceleration are at mid-bay.

Liu (2015) compared predictions from Equation 8, with R = 1.0, with 65 measurements to determine the accuracy and establish the calibration factor. The predictions were slightly conservative with an average measured-to-predicted ratio of 0.870 and a coefficient of variation (COV) of 33%. An R value of 1.3 results in 10% of measured accelerations exceeding predicted accelerations.

Equation 8 was simplified for design guide implementation as follows. The damping ratio is usually between 0.03 and 0.05. The average resonant buildup is due to approximately six footsteps, so the resonant buildup duration, T_{BU}, ranges from 6/2.2 Hz = 2.7 sec to 6/1.6 Hz = 3.8 sec. For these values of β and T_{BU}, and $f_n \geq 6$ Hz, the resonant buildup factor, ρ, is between 0.95 and 1.0, so it is conservatively taken as 1.0.

After setting R equal to 1.3, substituting Equation 5 for α_h, setting ρ equal to 1.0 and simplifying, the peak acceleration due to a resonant buildup is:

$$a_p = \frac{21.5}{\beta W}e^{-\gamma f_n}g \tag{9}$$

where g is the gravitational acceleration and the other variables are defined previously.

Figure 6 summarizes the measured-to-predicted ratio for the measurements by Liu (2015) and predictions from Equation 9.

The peak velocity is approximately equal to the peak acceleration divided by $2\pi f_n$. In units of mips, the peak velocity due to a resonant buildup is:

$$V_p = \frac{1.32\times 10^9}{\beta W f_n}e^{-\gamma f_n} \tag{10}$$

Maximum Narrowband Acceleration and Velocity Due to a Resonant Response

The maximum narrowband spectral acceleration, shown as the highest peak in Figure 1(b), is computed by Fourier transformation of the waveform in Figure 5. The peak acceleration in the waveform is from Equation 8 with the calibration factor removed.

The resonant buildup is assumed to be 3 sec long, which is approximately the average duration considering six footsteps at the average step frequency of 2 Hz. The remainder of the waveform is viscous decay. The duration of the waveform has a significant influence on the computed spectral acceleration. Shorter durations result in higher spectral accelerations because a larger portion of the waveform consists of the buildup, which has higher responses than the decay portion. The shortest reasonable duration that is expected to be used by site surveyors is 8.0 sec because this results in a 0.125-Hz frequency resolution. Shorter durations result in spectra that are overly coarse. Thus, 8 sec is used herein.

The Fourier transformation results in the following equation for the maximum magnitude. See Liu (2015) for a detailed derivation. Note that the result is an RMS acceleration.

$$A_{NB} = R\frac{27}{\sqrt{2}}\frac{\alpha_h}{\beta^2 W f_n T}\left[C-(1-e^{-C})(e^{-C})^{r_t}\right]g \tag{11}$$

where

T = total duration of waveform, sec

r_t = duration of decay divided by duration of buildup

The variable, C, is:

$$C = 12\pi\beta H \tag{12}$$

where H is the number of the harmonic that causes resonance, estimated by:

$$H = f_n / f_{step} \tag{13}$$

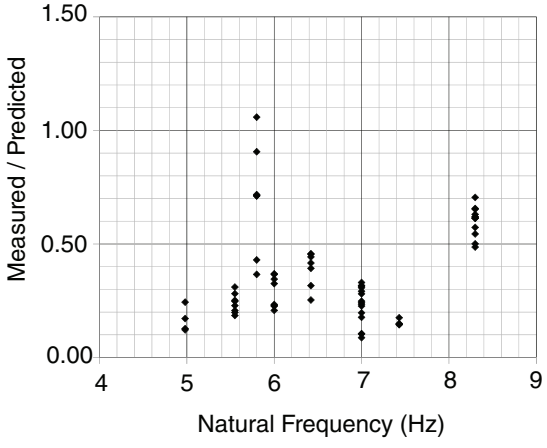

Fig. 6. Comparisons of measurements and predictions, resonant responses, peak acceleration.

Table 2. One-Third Octave Bands		
Lower Limit (Hz)	**Center Frequency (Hz)**	**Upper Limit (Hz)**
3.55	4.0	4.47
4.47	5.0	5.62
5.62	6.3	7.08
7.08	8.0	8.91
8.91	10.0	11.2
11.2	12.5	14.1
14.1	16.0	17.8
17.8	20.0	22.4

The step frequency, f_{step} is the mid-range frequency from Table 1.

For the database of floors mentioned previously, the average measured-to-predicted ratio, with $R = 1.0$, was 0.780 and the COV was 46.2%. The calibration factor, R, for a 10% probability of exceedance, is 1.3 (Liu, 2015).

Equation 11 was simplified for design guide implementation as follows. The second term was omitted because it is much smaller than C. After substituting Equation 5 for α_h, including $R = 1.3$, and simplifying, the narrowband spectral acceleration maximum RMS magnitude is:

$$A_{NB} = \frac{7.2}{\beta W} e^{-\gamma f_n} g \tag{14}$$

Figure 7 summarizes the measured-to-predicted ratio for the aforementioned measurements and predictions from Equation 14.

The narrowband spectral velocity equals the spectral acceleration divided by $2\pi f$ for all frequencies, f. After simplifying, the narrowband spectral velocity maximum magnitude—in mips, RMS—due to a resonant buildup is:

$$V_{NB} = \frac{442 \times 10^6}{\beta W f_n} e^{-\gamma f_n} \tag{15}$$

Maximum One-Third Octave Acceleration and Velocity Due to a Resonant Response

The one-third octave velocity is determined by bandwidth conversion from narrow bands to the bands summarized in Table 2. A one-third octave band encompasses many narrow bands, exemplified by the band with 5 Hz center frequency in Figure 8, so it contains the summation of the energies of the spectral accelerations in the contained narrow bands.

The energy of the signal at a narrowband frequency, f, is:

$$E_{NB}(f) = A_{NB,R=1}(f)^2 \tag{16}$$

where $A_{NB,R=1}$ is the peak acceleration from Equation 11 with $R = 1.0$.

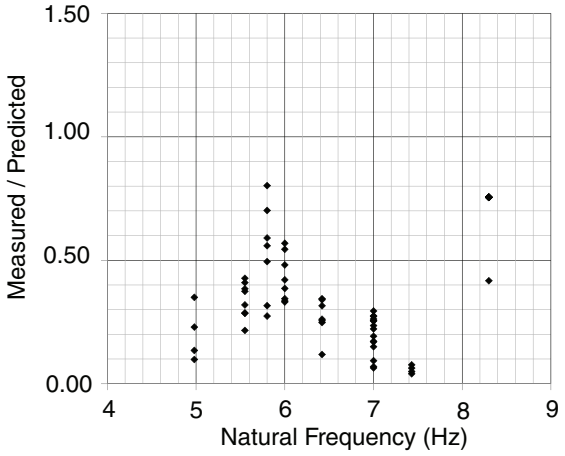

Fig. 7. Comparisons of measurements and predictions, resonant responses, narrowband acceleration.

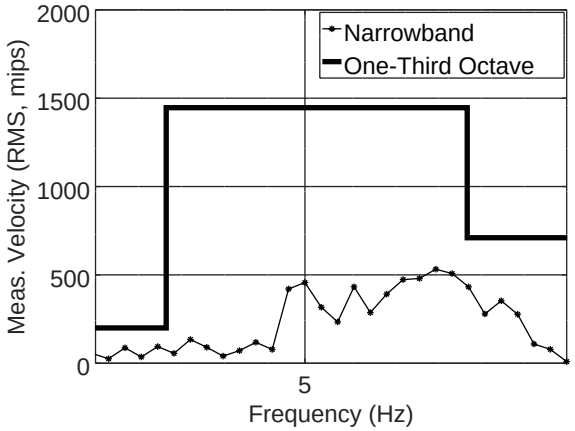

Fig. 8. Example one-third octave band.

The energy spectral density (ESD) at frequency, f, is:

$$ESD(f) = A_{NB,R=1}(f)^2/\Delta f \tag{17}$$

where the narrowband spectral resolution, Δf, is the reciprocal of the duration, T, of the walking event used to compute the narrowband spectrum.

The energy of the signal within a one-third octave band is the area under the ESD curve in the one-third octave band (Liu, 2015). Typically, one peak in the narrowband spectrum [Figure 1(b)] fits within a one-third octave band. This peak can be idealized as a triangle with maximum magnitude equal to the value from Equation 11 with R = 1.0. The width of the triangle is approximately 10% of the harmonic frequency (Brownjohn et al., 2004), which equals the natural frequency. The energy spectral density of this peak is slightly curved as shown in the example in Figure 9. In this example, the natural frequency is 6.2 Hz, so the peak is 0.62 Hz wide. This peak fits inside the 6.3-Hz one-third octave band, which has lower and upper bounds shown dashed on the plot.

The energy of the signal within the one-third octave band is:

$$E_{1/3} = \int ESD(f)\,df = \frac{1}{3}\frac{(A_{NB,R=1})^2}{\Delta f}\frac{f_n}{10} = \frac{(A_{NB,R=1})^2 Tf_n}{30} \tag{18}$$

where

$A_{NB,R=1}$ = spectral acceleration magnitude from Equation 11 with R = 1.0

T = duration of waveform used in the Fourier transformation, 8.0 sec

Using Equations 16 and 18, the uncalibrated one-third octave acceleration is derived as follows. (The uncalibrated version is carried through this calculation because the calibration factor is potentially different for narrowband acceleration and one-third octave acceleration.)

$$\begin{aligned} E_{1/3} &= A_{1/3,R=1}^2 \\ \frac{(A_{NB,R=1})^2 Tf_n}{30} &= A_{1/3,R=1}^2 \\ A_{1/3,R=1} &= A_{NB,R=1}\sqrt{\frac{Tf_n}{30}} \end{aligned} \tag{19}$$

The one-third octave velocity is the acceleration divided by $2\pi f_n$:

$$V_{1/3,R=1} = \frac{A_{NB,R=1}}{2\pi f_n}\sqrt{\frac{Tf_n}{30}} = \frac{A_{NB,R=1}}{2\pi}\sqrt{\frac{T}{30 f_n}} \tag{20}$$

For the database of floors mentioned above, the average measured-to-predicted velocity ratio was 0.640 and the COV was 38.7%. The calibration factor, R, for a 10% probability of exceedance, is 1.0 (Liu, 2015).

Equations 19 and 20 are simplified for design guide implementation by substituting Equation 14 with R = 1.0 for $A_{NB,R=1}$ and using T = 8 sec. After simplification, the one-third octave acceleration, RMS, due to a resonant buildup, is:

$$A_{1/3} = \frac{6.39}{\beta W}e^{-\gamma f_n}g \tag{21}$$

Also, the one-third octave velocity, RMS in mips, is:

$$V_{1/3} = \frac{175\times10^6}{\beta W\sqrt{f_n}}e^{-\gamma f_n} \tag{22}$$

Figure 10 summarizes the measured-to-predicted ratio for the measurements mentioned above and predictions from Equation 22.

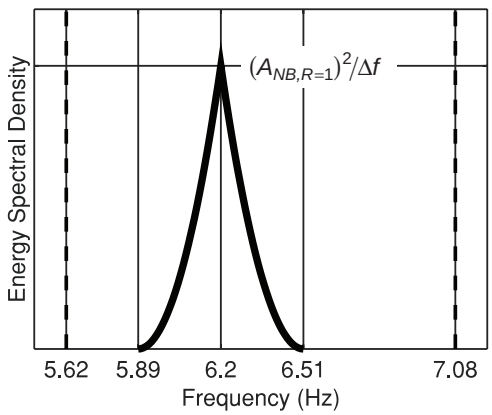

Fig. 9. Energy spectral density.

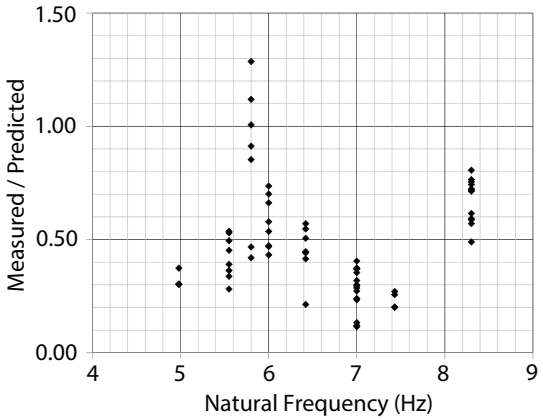

Fig. 10. Comparisons of measurements and predictions, resonant responses, one-third octave velocity.

PREDICTION OF IMPULSE RESPONSES

If the fundamental frequency exceeds the maximum frequency of the fourth harmonic, f_{4max}, resonance will not occur, and the maximum response resembles a series of individual impulse responses with little or no buildup. An example measured waveform is shown in Figure 11. The higher responses near the middle of the waveform are due to footsteps near mid-bay. The development in the following is described in detail in Liu (2015) and Liu and Davis (2015).

Peak Acceleration and Velocity Due to Impulse Response

The peak velocity immediately after a footstep is the product of a calibration factor, R, and the effective impulse from Equation 7, divided by the effective mass of the bay. Multiple modes contribute significantly to impulse responses, so a factor, $R_M = 2.0$, from Liu and Davis (2015), is included.

$$v_p = RR_M \frac{I_{eff}}{M_{eff}} = RR_M \frac{Q}{17.8} \frac{f_{step}^{1.43}}{f_n^{1.30}} \frac{2g}{W} \tag{23}$$

The peak acceleration is approximately equal to the peak velocity multiplied by $2\pi f_n$:

$$a_p = RR_M \frac{Q}{17.8} \frac{f_{step}^{1.43}}{f_n^{1.30}} \frac{2g}{W} (2\pi f_n) \tag{24}$$

A total of 89 measured peak accelerations were compared to predictions from Equation 24, with R = 1.0, to assess the accuracy of the equation and establish the calibration factor. The average measured-to-predicted ratio was 0.966 and the COV was 26%. R = 1.3 results in 10% of measured accelerations exceeding predicted accelerations (Liu, 2015; Liu and Davis, 2015).

After simplification, the following two equations are recommended. Note that v_p is in units of mips.

$$v_p = \frac{18.9 \times 10^9}{W} \frac{f_{step}^{1.43}}{f_n^{1.30}} \tag{25}$$

$$a_p = \frac{308}{W} \frac{f_{step}^{1.43}}{f_n^{0.3}} g \tag{26}$$

where f_{step} is the mid-range frequency from Table 1.

Figure 12 summarizes the measured-to-predicted ratio for the measurements mentioned above and predictions from Equation 26.

Maximum Narrowband Acceleration and Velocity Due to a Series of Impulse Responses

The maximum narrowband acceleration due to a series of impulses responses is computed by Fourier transforming the idealized waveform in Figure 13 and then adjusting for several differences between the idealized waveform and measured waveforms.

The peak acceleration in the idealized waveform is from Equation 26 with the calibration factor, 1.3, removed. This peak acceleration is for acceleration at mid-bay due to a footstep at mid-bay. The remainder of the response to each footstep is viscous decay. Identical footsteps are appended at the step frequency, so the waveform is perfectly periodic. The Fourier transformation results in a very complicated equation for the spectral peak at each harmonic of the walking force (Liu and Davis, 2015). The maximum spectral magnitude (peak, not RMS) for this idealized walking event, $A_{NB,I}$, at the natural frequency, is:

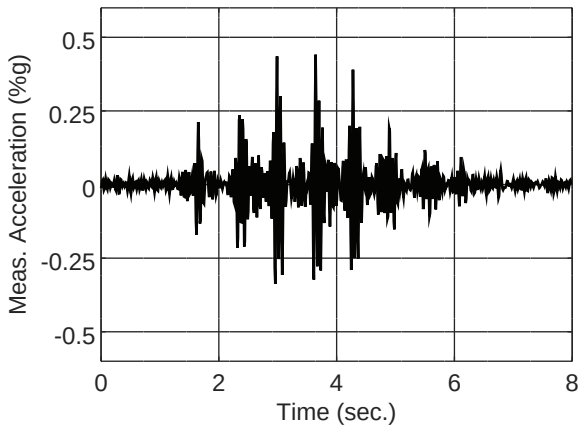

Fig. 11. Example series of impulse responses.

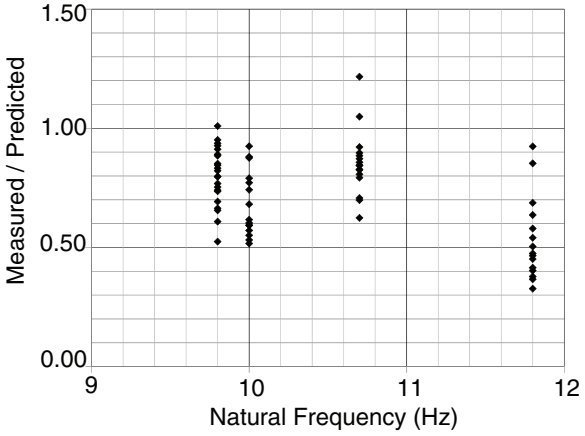

Fig. 12. Comparisons of measurements and predictions, impulse responses, peak acceleration.

$$A_{NB,I} = a_{p,R=1} \frac{1 - e^{-2\pi\beta H}}{2\pi\beta H} \tag{27}$$

where $a_{p,R=1}$ is from Equation 24 with $R = 1.0$, and H is the number of the harmonic at the natural frequency.

Actual footsteps are not identical, nor are they repeated precisely at the step frequency. This results in energy being leaked into frequencies adjacent to each harmonic frequency, and lower spectral peaks. This is considered with the imperfect footsteps reduction factor, $R_I = 0.6$, which is based on research by Brownjohn et al. (2004).

Actual walking events do not have infinite durations as used in the Fourier transformation leading to Equation 27. Recall that the objective is to predict what the site surveyor will measure, and it is assumed that the Fourier transformations will be of waveforms lasting 8 sec. The duration of the series of impulse responses varies, but is taken as 4 sec, see Figure 11 for an example. This results in a duration adjustment factor, $R_D = 0.5$.

Actual walking events do not have each footstep at mid-bay. Instead, some footsteps will be applied near mid-bay where the mode shape values are maximal and others will be applied away from mid-bay. For walking that traverses an entire bay with a half sine wave mode shape, the adjustment factor is 0.7. Slightly conservatively, the adjustment factor, R_L, is taken as 0.9.

After these adjustments are made and a calibration factor, R, is added, the maximum RMS magnitude is:

$$A_{NB} = \frac{1}{\sqrt{2}} R R_I R_D R_L a_{p,R=1} \frac{1 - e^{-2\pi\beta H}}{2\pi\beta H} \tag{28}$$

where $a_{p,R=1}$ is from Equation 24 with $R = 1.0$, and H is the number of the harmonic at the natural frequency.

Measurements from the database mentioned above were compared to predictions from Equation 28 with $R = 1.0$ to assess the accuracy of the equation and establish the calibration factor. The average measured-to-predicted ratio was 0.790 and the COV was 32%. An R value of 1.1 results in 10% of measured accelerations exceeding predicted accelerations (Liu, 2015; Liu and Davis, 2015).

After the inclusion of the calibration factor and simplification, the RMS magnitude is:

$$A_{NB} = \frac{7.93}{\beta W} \frac{f_{step}^{2.43}}{f_n^{1.3}} (1 - e^{-2\pi\beta f_n / f_{step}}) g \tag{29}$$

Figure 14 summarizes the measured-to-predicted ratio for the aforementioned measurements and predictions from Equation 29.

The narrowband velocity magnitude is computed by dividing Equation 29 by $2\pi f_n$. The RMS magnitude in mips is:

$$V_{NB} = \frac{487 \times 10^6}{\beta W} \frac{f_{step}^{2.43}}{f_n^{2.3}} (1 - e^{-2\pi\beta f_n / f_{step}}) \tag{30}$$

Maximum One-Third Octave Acceleration and Velocity Due to a Series of Impulse Responses

The one-third octave acceleration and velocity due to a series of impulse responses were determined using the bandwidth conversion method described above for resonant responses.

The one-third octave velocity is computed using Equation 20 with $A_{NB,R=1}$ from Equation 28. Measurements from the database mentioned above were compared to predictions to assess the accuracy of the predictions and establish the calibration factor. The average measured-to-predicted ratio was 0.736 and the COV was 34%. An R value of 1.1 results in 10% of measured accelerations exceeding predictions (Liu, 2015; Liu and Davis, 2015).

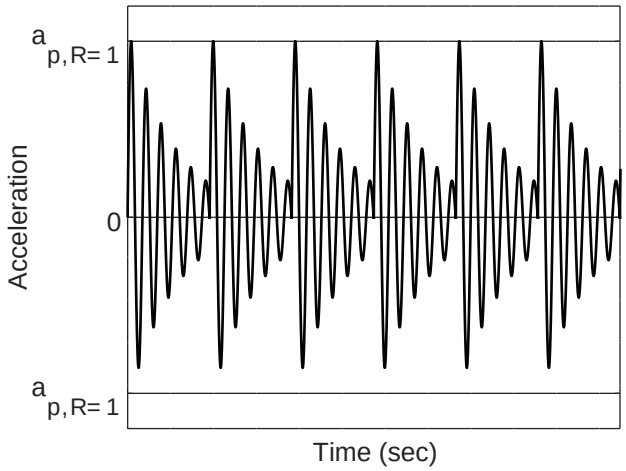

Fig. 13. Idealized impulse series of impulse responses.

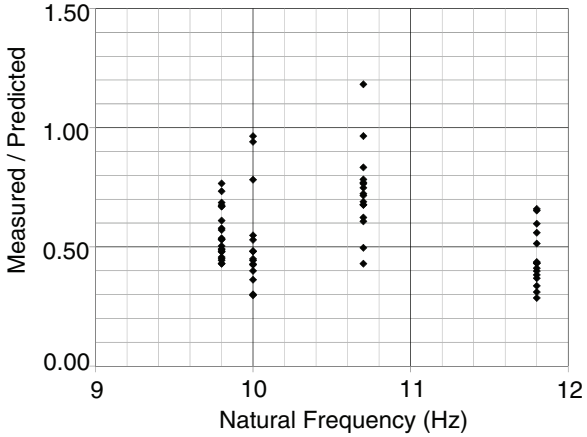

Fig. 14. Comparisons of measurements and predictions, impulse responses, narrowband acceleration.

Table 3. Boundaries of Intermediate Zones		
Walking Speed	**f_L (Hz)**	**f_U (Hz)**
Slow	6.0	8.0
Moderate	7.0	9.0
Fast	8.0	10.0

After including the calibration factor and simplifying, the one-third octave RMS velocity due to a series of impulse responses in mips is:

$$V_{1/3} = \frac{252 \times 10^6}{\beta W} \frac{f_{step}^{2.43}}{f_n^{1.8}} \left(1 - e^{-2\pi\beta f_n / f_{step}}\right) \quad (31)$$

Figure 15 summarizes the measured-to-predicted ratio for the aforementioned measurements and predictions from Equation 31.

The one-third octave acceleration is computed using Equation 19 with $A_{NB,R=1}$ from Equation 28. After including the calibration factor of R = 1.1 and simplifying, the RMS acceleration is:

$$A_{1/3} = \frac{4.2}{\beta W} \frac{f_{step}^{2.43}}{f_n^{0.8}} \left(1 - e^{-2\pi\beta f_n / f_{step}}\right) g \quad (32)$$

RESPONSE PREDICTION

The first step in predicting the response is the selection of the tolerance limit. The form (peak acceleration) of the response prediction must obviously match the tolerance limit.

As explained in the Resonant Response section, resonant responses are possible when the natural frequency does not exceed the maximum frequency of the fourth harmonic, f_{4max}. Impulse responses are possible for any natural frequency. The controlling response is the maximum of the two, and when a resonant response is possible, it usually greatly exceeds the impulse response. This is illustrated in Figure 16. This example is for slow walking (f_{4max} = 6.8 Hz) on a floor with W = 250 kips and β = 0.05. As f_n crosses f_{4max} on the plot, the controlling velocity decreases abruptly by a large amount, which would not occur in reality. It is much more likely that the behavior would gradually change from resonant to impulse response as the natural frequency crosses f_{4max}, thus defining a region of intermediate responses. For design guide implementation, linear interpolation is used in this region, which is 2 Hz wide and approximately centered on f_{4max} as shown in Figure 16. The lower and upper bounds of the intermediate zones are in Table 3.

For very slow walking, the impulse response is computed regardless of the natural frequency. For slow, moderate, and fast walking, if the natural frequency does not exceed f_L, then the resonant response is computed using equations from the Resonant Responses section. If the natural frequency exceeds f_U, then the impulse response is computed using equations from the Impulse Responses section. If the natural frequency is between f_L and f_U, then the intermediate response is computed by linear interpolation between the resonant response at f_L and the impulse response at f_U. In equation form, using one-third octave velocity for example:

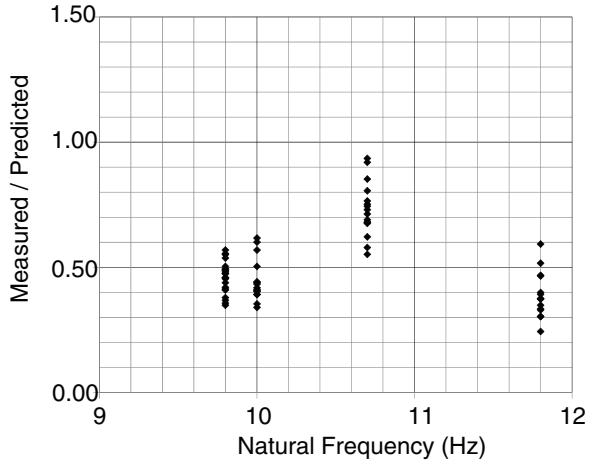

Fig. 15. Comparisons of measurements and predictions, impulse responses, one-third octave velocity.

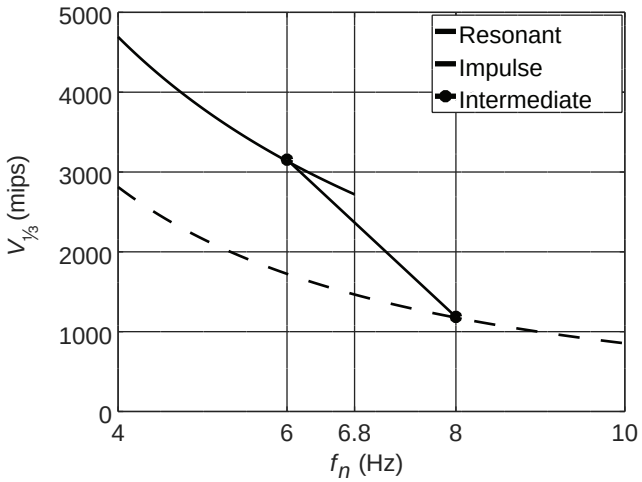

Fig. 16. Example velocity as a function of natural frequency.

$$V_{1/3} = \begin{cases} \dfrac{175\times10^6}{\beta W\sqrt{f_n}} e^{-\gamma f_n} \\ \dfrac{252\text{x}10^6}{\beta W}\dfrac{f_{step}^{2.43}}{f_n^{1.8}}\left(1-e^{-2\pi\beta f_n/f_{step}}\right) \end{cases} \quad \text{if } f_n \le f_L \qquad (33a)$$

$$V_{1/3} = \frac{252\times10^6}{\beta W}\frac{f_{step}^{2.43}}{f_n^{1.8}}\left(1-e^{-2\pi\beta f_n/f_{step}}\right) \quad \text{if } f_n > f_U \qquad (33b)$$

For one-third octave velocity, the resonant response controls if $f_n \le f_L$, so Equation 33a and 33b reduce to:

$$V_{1/3} = \begin{cases} \dfrac{175\times10^6}{\beta W\sqrt{f_n}} e^{-\gamma f_n} \text{ if } f_n \le f_L \\ \dfrac{252\times10^6}{\beta W}\dfrac{f_{step}^{2.43}}{f_n^{1.8}}\left(1-e^{-2\pi\beta f_n/f_{step}}\right) \text{ if } f_n > f_U \end{cases} \qquad (34)$$

All response equations presented above are for the worst-case scenario of mid-bay vibration response to walking through mid-bay. Very often, the equipment is located away from mid-bay. Also, walls and other obstacles often prevent walking through mid-bay. Tolerance limits are often very stringent, so the response should typically be computed based on the actual equipment location and walking path location. This is accomplished by scaling the mid-bay response by the ratio of mode shape values.

When the equipment is away from mid-bay and the walker can pass through mid-bay, the predicted response, using velocity for example, is:

$$V = V_{midbay}\frac{\phi_e}{\phi_{midbay}} \qquad (35)$$

where

V = response at the equipment

V_{midbay} = response at mid-bay due to walking through mid-bay

ϕ_e = mode shape value at the equipment location

ϕ_{midbay} = mode shape value at mid-bay

When the walking path does not pass through mid-bay, and the equipment is at mid-bay, the predicted response is:

$$V = V_{midbay}\frac{\phi_w}{\phi_{midbay}} \qquad (36)$$

where ϕ_w is the maximum mode shape value along the walking path.

When neither the equipment nor the walking path is at mid-bay, the predicted response is:

$$V = V_{midbay}\frac{\phi_e}{\phi_{midbay}}\frac{\phi_w}{\phi_{midbay}} \qquad (37)$$

The mode shape values can be determined by any rational method such as finite element analysis per AISC Design Guide 11, Chapter 7. For simple cases with typical framing, Equation 3 can be used or adjusted for other boundary conditions.

COMMENTARY ON FIRST AND SECOND EDITIONS OF AISC DESIGN GUIDE 11, CHAPTER 6

The methods in the first and second editions of AISC Design Guide 11, Chapter 6, were derived using significantly different models, so the velocity predictions differ significantly in some cases. The following are the main differences between the two editions.

For frequencies above 8–9 Hz, the responses are impulsive, and the second edition takes this into account. Impulse responses are not strongly linked to natural frequency, but are strongly linked to mass. Thus, natural frequency often plays a less prominent role and mass plays a more prominent role in the second edition than in the first edition.

Response is not a function of damping in the first edition. However, in the second edition, most of the responses are functions of damping because the spectral responses depend on the entire waveform, including the decay portion. It is noted that this makes velocity comparisons difficult between the two editions.

In the first edition, moderate walking causes much higher velocities than those from slow walking. Similarly, fast walking causes much higher velocities than those from moderate walking. Our measurements indicate the differences are not as large as those in the first edition. Thus, the second edition responses for various speeds are much closer together. Also, the speed categories are different. Slow walking in the first edition is fairly close to very slow walking in the second edition.

CONCLUSIONS

Floor vibration tolerance limits for sensitive equipment, in terms of various acceleration and velocity measures, are much more stringent than those for human comfort.

The floor response to walking is affected by the speed of walking, natural frequency, effective mass, and damping. Walking in higher speed categories causes higher responses. Higher natural frequency, effective mass, and damping cause lower responses. For lower frequency floors, the highest response is due to a resonant buildup. For higher frequency floors, the highest response is due to a series of impulse responses to individual footsteps.

Fairly simple equations for resonant and impulse responses are recommended herein for design. These equations use natural frequency, effective weight, and damping

estimates from AISC Design Guide 11; they are suitable for manual calculations. Note that natural frequency and effective mass or weight can be determined through other means such as finite element analyses. The response prediction equations have been experimentally verified with fairly large databases of walking measurements on lower and higher frequency floors.

Vibration of floors supporting sensitive equipment is usually very objective. Also, reduction of vibration levels of a constructed floor is difficult and expensive. Thus, each response prediction equation includes a calibration factor that results in predictions that exceed measured vibration levels 90% of the time.

ACKNOWLEDGMENTS

The authors thank AISC for funding the research that resulted in the methods described herein.

REFERENCES

Allen, D.E. and Murray, T.M. (1993), "Design Criteria for Vibrations Due to Walking," *Engineering Journal*, AISC, Vol. 30, No. 4, pp. 117–129.

Brownjohn, J.M.W., Pavic, A., and Omenzetter, P. (2004), "A Spectral Density Approach for Modelling Continuous Vertical Forces on Pedestrian Structures Due to Walking," *Canadian Journal of Civil Engineering*, Vol. 31, No. 1, pp. 65–77.

Chopra, A.K. (2011), *Dynamics of Structures: Theory and Applications to Earthquake Engineering*, 4th Ed., Prentice Hall, Upper Saddle River, N.J.

Clough, R.W. and Penzien, J. (1993), *Dynamics of Structures*, 2nd Ed., McGraw-Hill, New York, N.Y.

Kerr, S.C. (1998), "Human Induced Loading on Staircases," PhD Thesis, University of London, London, England.

Liu, D. (2015), "Vibration of Steel-Framed Floors Supporting Sensitive Equipment in Hospitals, Research Facilities, and Manufacturing Facilities," PhD Dissertation, University of Kentucky, Lexington, Ky. (in preparation).

Liu, D. and Davis, B. (2015), "Walking Vibration Response of High-Frequency Floors Supporting Sensitive Equipment," *Journal of Structural Engineering*, Vol. 141, No. 8.

Murray, T.M., Allen, D.E., and Unger, E.E. (1997), *Floor Vibrations Due to Human Activity*, Design Guide 11, AISC, Chicago, Ill.

Murray, T.M., Allen, D.E., Unger, E.E., and Davis, D.B. (2016), *Vibration of Steel-Framed Structural Systems Due to Human Activity*, Design Guide 11, 2nd Ed., AISC, Chicago, Ill.

NRCC (2010), *National Building Code of Canada*, National Research Council of Canada, Ottawa, Canada.

Pabian, S., Thomas, A., Davis, B., and Murray, T.M. (2013), "Investigation of Floor Vibration Evaluation Criteria Using an Extensive Database of Floors," *Proceedings of the ASCE/SEI Structures Congress*, ASCE, May 2–3, Pittsburgh, Pa., pp. 2,478–2,486.

Rainer, J.H., Pernica, G., and Allen, D.E. (1988), "Dynamic Loading and Response of Footbridges," *Canadian Journal of Civil Engineering*, Vol. 15, No. 1, pp. 66–71.

Smith, A.L., Hicks, S.J., and Devine, P.J. (2009), *Design of Floors for Vibration: A New Approach*, (Revised), SCI P354, The Steel Construction Institute (SCI), Silwood Park, Ascot, Berkshire.

Ungar, E.E. and White, R.W. (1979), "Footfall-Induced Vibrations of Floors Supporting Sensitive Equipment," *Sound and Vibration*, Vol. 13, October, pp. 10–13.

Ungar, E., Zapfe, J., and Kemp, J. (2006), "Predicting Footfall-Induced Floor Vibrations Relative to Criteria for Sensitive Apparatus," *Proceedings of the ASCE/SEI Structures Congress*, ASCE, May 18–21, St. Louis, Mo., pp. 1–13.

Willford, M. and Young, P. (2006), *A Design Guide for Footfall Induced Vibration of Structures*, CCIP-016, The Concrete Centre, Surrey, UK.

Willford, M., Young, P., and Field, C. (2007a), "Predicting Footfall-Induced Vibration: Part 1," *Structures and Buildings*, Vol. 160, No. SB2, pp. 65–72.

Willford, M., Young, P., and Field, C. (2007b), "Predicting Footfall-Induced Vibration: Part 2," *Structures and Buildings*, Vol. 160, No. SB2, pp. 73–79.

Young, P. and Willford, M. (2001), *Towards a Consistent Approach to the Prediction of Footfall-Induced Structural Vibration,* Internal Document, Ove Arup and Partners, London, UK.

Zivanovic, S., Pavic, A., and Reynolds, P. (2007), "Probability-Based Prediction of Multi-Mode Vibration Response to Walking Excitation," *Engineering Structures*, Vol. 29, No. 6, pp. 942–954.

Weld Effective Lengths for Round HSS Cross-Connections under Branch Axial Loading

KYLE TOUSIGNANT and JEFFREY A. PACKER

ABSTRACT

Recent experimental and numerical research performed on fillet-welded, round-to-round, HSS cross-connections is reviewed, along with prior research on round HSS-to-rigid plate connections. The data from these weld-critical tests are then interpreted to determine practical weld effective lengths for such connections, in conjunction with permitting the directional strength-increase factor for fillet welds to round HSS. Recommendations are made for AISC *Specification* Section K5, and a design example is given to illustrate the approach.

Keywords: hollow structural sections, welded joints, cross-connections, weld effective lengths, fillet welds, design procedures.

The AISC *Specification for Structural Steel Buildings* (AISC, 2016), hereafter referred to as the AISC *Specification*, gives weld effective lengths for plate-to-rectangular HSS welded joints and rectangular-to-rectangular HSS welded joints in Section K5. These are used to design welds between plate and HSS branches to rectangular HSS main members whenever the welds are to be "fit for purpose" and not necessarily able to develop the yield capacity of the branch. However, for round-to-round HSS connections, the AISC *Specification* is silent, and there are no weld effective length rules given for such connections. As a consequence of this uncertainty, there is a tendency for many designers to just specify complete-joint-penetration (CJP) groove welds for round-to-round HSS connections, which is an expensive and undesirable default practice.

It is known that the load distribution around the perimeter of a round HSS welded joint can be highly nonuniform (Marshall, 1992). To deal with potential weld "unzipping" caused by one part of a welded joint being much more highly loaded than another, AWS D1.1, clause 9.6.1.3(4), (AWS, 2015) implies that the weld effective length in axially loaded round-to-round HSS connections is equal to $1/1.5$ of the total weld length under factored loads. This simple rule is believed to be conservative, but the weld effective length is likely to vary with specific connection parameters, particularly the cross-sectional slenderness of the chord wall, D/t. This paper reviews research data with the objective of assessing—and improving on—this recommendation, while still satisfying the AISC target reliability index.

Because the design of welds in codes/specifications is based on simplification of a complex loading, any proposed effective length approach to the design of welds must be checked for its safety level in conjunction with the weld design rules of a particular specification. While AISC *Specification* Section K5 (AISC, 2016) explicitly prohibits the use of the "fillet weld directional strength-enhancement factor," $(1.0 + 0.50 \sin^{1.5} \theta)$, when designing "fit for purpose" welds for rectangular HSS, the AISC *Specification* is again silent about whether it is allowed when designing such welds for round HSS.

Laboratory testing and finite element analysis studies have been performed on fillet-welded joints to the ends of HSS members, where the HSS end is connected to a rigid plate and the HSS is subjected to axial tension (Packer et al., 2016; Tousignant and Packer, 2016; 2017a). In such situations, the entire weld length is effective due to the rigid base material. This research has shown that single-sided welds to a tension-loaded HSS wall element are partially unrestrained and are prone to local bending about the axis of the weld, as shown in Figure 1, leading to opening of the weld root. The restraint provided to the fillet weld depends on the connected element thickness and shape (linear versus curved), as well as the weld size and amount of penetration. It was found that the HSS welded joints in the aforementioned research did not achieve the expected target safety (reliability) index of $\beta^+ \geq 4.0$ at failure, as discussed in AISC *Specification* Commentary B3.1, if the fillet weld directional strength-enhancement factor was applied. In general, however, setting this factor of $(1.0 + 0.50 \sin^{1.5} \theta)$ to unity (i.e., taking θ as zero) when calculating the strength of fillet welds to tension-loaded HSS wall elements achieves $\beta^+ \geq 4.0$.

In the aforementioned studies, the single-sided weld effect was much more severe for square and rectangular HSS than

Kyle Tousignant, PhD, Assistant Professor, Department of Civil and Resource Engineering, Dalhousie University, Halifax, Nova Scotia, Canada. E-mail: kyle.tousignant@dal.ca (corresponding)

Jeffrey A. Packer, PhD, Bahen/Tanenbaum Professor of Civil Engineering, Department of Civil and Mineral Engineering, University of Toronto, Toronto, Ontario, Canada. E-mail: jeffrey.packer@utoronto.ca

Paper No. 2019–02

Table 1. Proposed Changes to the Applicability of the sinθ Factor for Fillet Welds to HSS			
Case	**Loading Sense**	**2016 AISC *Specification***	**2022 AISC *Specification***
Fillet welds connecting round HSS branches to base plates, cap plates, or HSS chords	Tension	Permitted	Permitted
	Compression	Permitted	Permitted
	Pure bending	Permitted	Permitted
Fillet welds connecting square or rectangular HSS branches to base plates, cap plates, or HSS chords	Tension	Not permitted in truss-type connections, otherwise permitted (K5 Commentary)	Not permitted
	Compression		Permitted
	Pure bending		Not permitted*
Double-sided fillet welds connecting longitudinal or transverse branch plates to HSS chords	Tension	Permitted	Permitted
	Compression	Permitted	Permitted
	Pure bending	Permitted	Permitted

* AISC TC6 has recommended that the sinθ factor not be permitted when any face of the square or rectangular HSS branch is in tension (e.g., under pure bending). Provided that the entire branch remains under compression, the sinθ factor may be used for axial compression plus bending loading.

for round HSS, when viewed separately. Recent reliability analysis of round HSS-to-rigid plate experiments, combined with parametric finite element analyses thereof (Tousignant and Packer, 2019), has found that these connections generated a safety index of $\beta^+ = 3.7$. This is only marginally lower than the target value. AISC Committee on Specifications (COS) Task Committee 6 (TC6) on Connection Design has hence recommended that the fillet weld directional strength-enhancement factor for fillet welds to the ends of round HSS be permitted in the 2022 AISC *Specification*.

On the other hand, use of the directional strength-enhancement factor is not acceptable for fillet welds to the ends of square and rectangular HSS in which any face is in tension, when the design approach is to develop the yield strength of the connected HSS wall, nor when the design is a "fit-for-purpose" approach. The latter is covered in AISC *Specification* Section K5, and entails the use of weld effective lengths. The Section K5 provisions have been shown to generate suitable target safety (reliability) indices for welded joints to square and rectangular HSS with faces in tension, in conjunction with the weld effective lengths advocated and non-use of the "sinθ factor" (McFadden and Packer, 2014; Tousignant and Packer, 2015).

AISC TC6 has also recommended the use of the directional strength-enhancement factor for double-sided fillet welds to longitudinal or transverse plate branches, attached to all HSS, regardless of branch loading, and for single-sided welds between HSS branches and HSS chords where all of the branch remains in compression. Although not yet final for the 2022 AISC *Specification*, Table 1 provides a summary of the proposed changes to the applicability of the sinθ factor for fillet welds to HSS. For the purpose of this paper, it will be assumed that the fillet weld directional strength-enhancement factor is permitted for calculating the strength of welds to round HSS.

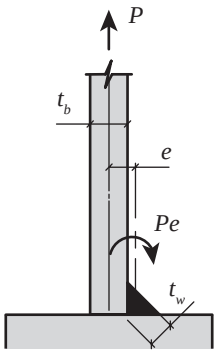

Fig. 1. Eccentric loading on a single-sided fillet weld, resulting in local bending.

EXPERIMENTS ON WELD-CRITICAL ROUND-TO-ROUND HSS CROSS-CONNECTIONS

A total of 12 laboratory tests have been performed on round-to-round HSS cross-connections, fabricated from large-size ASTM A500 (ASTM, 2018), dual-certified, Grade B/C HSS (Tousignant and Packer, 2017b). A professional fabricator was employed to deposit fillet welds all-around the branches using a semiautomatic, flux-cored arc welding process with a CO_2 shielding gas. The chord members were HSS10.75×0.500 and HSS16.00×0.500, with branches (at either 90° or 60°) selected to obtain branch-to-chord width ratios, β, ranging from 0.25 to 0.47. All test specimens had geometric configurations that permitted the use of fillet welding in accordance with AWS D1.1 (AWS, 2015). Welding procedure specifications were developed in conjunction with trial sectioning to achieve minimal, but adequate, root

penetration; the welds were ground to an ideal triangular shape; and careful measurements were made of the geometric and mechanical properties of the welds. Specimens were well-instrumented and loaded to failure by applying a quasi-static axial tension force to the end of the branches, as shown in Figure 2. Failure in all cases occurred in a brittle manner by fracture along a plane through the weld. A typical rupture failure is shown in Figure 3 for a 90° connection.

Strain gauges around the branch members close to the welds (such as indicated by SG in Figure 3) confirmed the nonuniform strain, and thus the tensile load distribution, around the branch and hence in the neighboring weld. For the 90° connections, the tensile strain decreased as a function of distance away from the highly loaded saddle position (indicated in Figure 3). An example of this strain variation around the branch and weld is shown in Figure 4 for various load levels corresponding to 25%, 50%, 75%, and 100% of the weld fracture load, P_a. In Figure 4, the subtended angle, x, is the angle measured clockwise (CW) around the branch, with 0° and 180° corresponding to the two crown points and 90° corresponding to the saddle point (see Figure 3). The tensile (positive) strain is therefore smallest at the crown, with much of the weld remaining in compression (negative strain) for the entire tensile load range, and largest at the saddle points. This nonuniform loading is more pronounced for connections with higher β values.

The nonuniformity of stress observed in the experiments (Tousignant and Packer, 2017b) will be prevalent in all round-to-round HSS connections of similar geometries (T-, Y-, and X-type) with branch axial loading. This would also apply regardless of the weld type [fillet, partial joint penetration (PJP) groove weld, or CJP groove weld] used to join the branch(es) to the chord, assuming that the welds do not significantly change the footprint of the branch(es).

NUMERICAL MODELING OF WELD-CRITICAL ROUND-TO-ROUND HSS CROSS-CONNECTIONS

Nonlinear finite element (FE) models, incorporating a weld fracture criterion, have been validated against the results of the 12 laboratory tests (Tousignant and Packer, 2018). A parametric study was then performed, consisting of 256 FE weld-critical, round HSS cross-connections with varied width ratio β, chord slenderness D/t, branch angle θ, and branch-to-chord thickness ratio τ. All numerical models failed by weld fracture. It was found that the weld

Fig. 2. Testing arrangement for round-to-round HSS cross-connections.

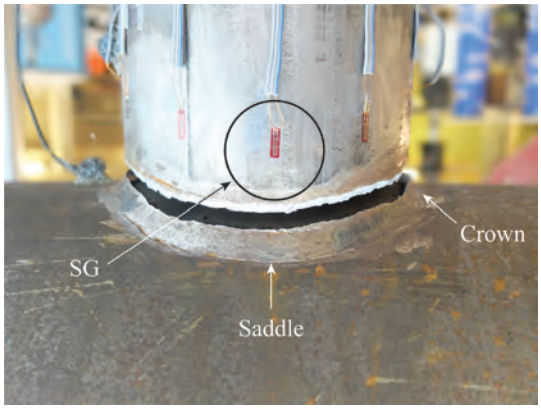

Fig. 3. Weld fracture in a 90° cross-connection.

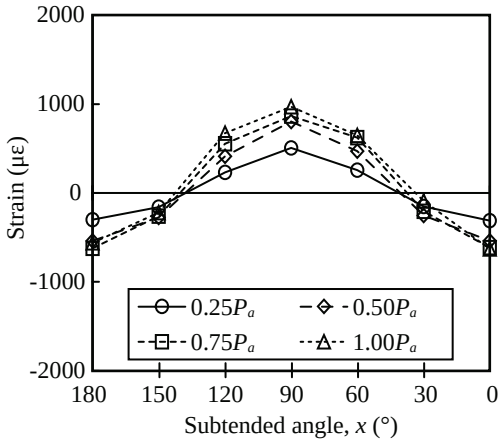

Fig. 4. Strain distribution around the weld, for a HSS5.00×0.500 branch to HSS10.75×0.500 chord.

effective length decreases as D/t increases, β increases, and τ increases. The weld effective length ranged from 0.58 to 1.0 times the total weld length within the parameter range studied ($60° \le \theta \le 90°$; $10 \le D/t \le 50$; $0.10 \le \beta \le 0.50$; $0.20 \le \tau \le 1.00$), with the weld length becoming 100% effective for $\beta(D/t) \le 8$. Within the range studied, the branch inclination angle had only a very minor effect on the weld effective length.

DESIGN

In Section K5 of the AISC *Specification* (AISC, 2016), a detailed design method considering weld effective lengths for plate-to-rectangular and rectangular-to-rectangular HSS welded joints is given. According to this section, the nominal strength of welds, R_n or P_n, in connections subject to branch axial load is based on the limit state of shear rupture along the plane of the weld effective throat and calculated as follows:

$$R_n \text{ or } P_n = F_{nw} t_w l_e \quad \textit{Spec.} \text{ Eq. K5-1 (1)}$$

where F_{nw} is the nominal stress of the weld metal calculated according to AISC *Specification* Chapter J, currently utilizing no increase in strength due to the directionality of load for fillet welds-to-rectangular HSS branches in tension or compression (i.e., omitting the $\sin\theta$ factor) (AISC, 2016).

According to the load and resistance factor design (LRFD) method of the AISC *Specification* (AISC, 2016), resistance factors of $\phi = 0.75$ and 0.80 for fillet and PJP groove welds, respectively, are applied to Equation 1 to determine available strength.

For round-to-round HSS welded joints, including cross-connections, Equation 1 would also apply. For such joints, based on the recent recommendation by AISC TC6, the $\sin\theta$ factor is permitted; that is,

$$F_{nw} = 0.60 F_{EXX} (1.0 + 0.50 \sin^{1.5}\theta) \quad \textit{Spec.} \text{ Eq. J2-5 (2)}$$

where θ is the angle between the line of action of the applied force and the weld longitudinal axis (in degrees) and F_{EXX} is the filler metal classification strength.

Application of the $\sin\theta$ factor to fillet welds in round-to-round HSS welded joints is nontrivial. The angle of loading, θ, varies continuously around the joint (see Figure 5), and calculation of θ at any point along the weld axis, let alone the value of the $\sin\theta$ factor for the entire joint, involves a complex procedure.

Calculation of the $\sin\theta$ Factor for a Round-to-Round HSS Joint

To calculate the loading angle of a fillet weld, θ, at a point along the weld axis, and to determine the value of the $\sin\theta$ factor for a round-to-round HSS joint, the following procedure can be used:

Step 1. Determine the coordinates of the branch/chord intersection at two points corresponding to x and $x + \Delta x$ at the root of the fillet weld. Calculate the vector $\overline{V}$ [see Figure 6(a)] to approximate the weld longitudinal axis between x and $x + \Delta x$. For the coordinate system shown in Figure 6(b):

$$\overline{V} = \left[\left(-l_{t,x+\Delta x} + l_{t,x}\right), \left(r_b \sin\left(x+\Delta x\right) - r_b \sin x\right), \left(-r_b \cos\left(x+\Delta x\right) + r_b \cos x\right) \right] \quad (3)$$

where r_b is the radius of the branch ($= D_b/2$), and:

$$l_{t,x} = \frac{r_b (1 - \cos x)}{\tan\theta} + \frac{r - \sqrt{r^2 - (r_b \sin x)^2}}{\sin\theta} \quad (4)$$

where r is the radius of the chord ($= D/2$). The dimension $l_{t,x}$ is shown in Figure 6(b). For $l_{t,x+\Delta x}$, substitute $x + \Delta x$ for x in Equation 4.

Step 2. Calculate the magnitude of $\overline{V}$ to determine the length, l_i, of the pseudo-linear weld element i [see Figure 6(a)] between x and $x + \Delta x$; that is,

$$l_i = \left|\overline{V}\right| \quad (5)$$

The smaller the value of Δx, the closer l_i will be to the actual weld length between the two points [1 and 2, in Figure 6(a)] at the root of the fillet weld.

Step 3. Increment x by Δx and calculate l_i again. Do this for all values of x between 0° and $360° - \Delta x$, then sum the results to determine the total weld length l_w; that is,

$$l_w = \sum l_i \quad (6)$$

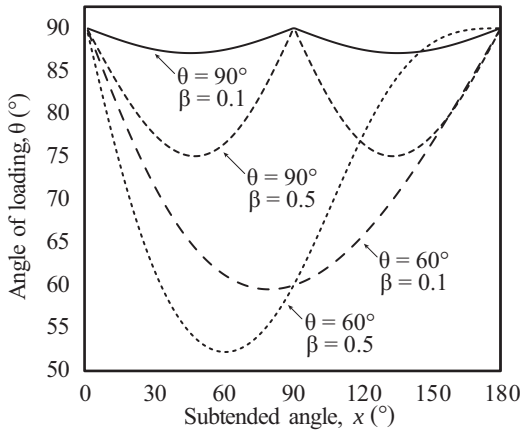

Fig. 5. Typical variations in loading angle of a fillet weld around a round-to-round HSS joint.

Step 4. Next, compute the vector that defines the direction of the applied force $\overline{P}$. For the coordinate system shown in Figure 6(b), one option is:

$$\overline{P} = [(1),(0),(0)] \tag{7}$$

Step 5. Calculate the angle of loading θ_i of each weld element i using the dot product; that is,

$$\theta_i = \cos^{-1}\left(\frac{\overline{V} \bullet \overline{P}}{|\overline{V}||\overline{P}|}\right) \tag{8}$$

In some cases, θ_i will be greater than 90°. It is recommended to calculate the acute angle of loading by subtracting the calculated angle from 180°. This has been done in Figure 5.

Step 6. Calculate the directional strength-enhancement factor for each weld element i by substituting θ_i for θ in the $(1.0 + 0.50 \sin^{1.5} \theta)$ term.

Step 7. Calculate the value of the $(1.0 + 0.50 \sin^{1.5} \theta)$ factor for the entire joint, K_{CHS}, by taking a weighted average of the $(1.0 + 0.50 \sin^{1.5} \theta_i)$ values for each weld element to account for variations in l_i; that is,

$$K_{CHS} = \frac{1}{l_w}\sum(1.0 + 0.50 \sin^{1.5} \theta_i)\, l_i \tag{9}$$

Equation 9 assumes that the weld effective throat, t_w, shown in Figure 1 is constant around the entire joint.

Sinθ Factor Design Aid

Using the procedure just outlined, with $\Delta x = 1°$, a design aid (given by Table 2) was developed to allow engineers to find the $(1.0 + 0.50 \sin^{1.5} \theta)$ factor for all-around fillet welds with a constant throat dimension in round-to-round HSS joints where fillet welds are potentially feasible. The value of $\Delta x = 1°$ used to develop the design values in Table 2 provides convergent values of the $(1.0 + 0.50 \sin^{1.5} \theta)$ factor within the range $0.1 \le \beta \le 0.5$ and $60° \le \theta \le 90°$. Table 2 is used by reading across and down for values of β and θ, respectively, for a given connection. For values of β and θ not shown, but within the range $0.1 \le \beta \le 0.5$ and $60° \le \theta \le 90°$, linear interpolation may be used.

Total Weld Length

The total weld length, l_w, measured at the root of the fillet weld, can be determined from 3D solid models of intersecting cylinders. Alternatively, it was shown that the K_a approximation given by AWS D1.1, clause 9.5.4 (AWS, 2015), is remarkably good, and slightly conservative, within the range $0.1 \le \beta \le 0.5$ and $60° \le \theta \le 90°$ (Tousignant and Packer, 2017b); i.e.,

$$l_w = \pi D_b K_a \tag{10}$$

where D_b is the branch diameter, θ is the branch inclination angle, and K_a is the weld length factor, given by:

$$K_a = \frac{1 + 1/\sin\theta}{2} \tag{11}$$

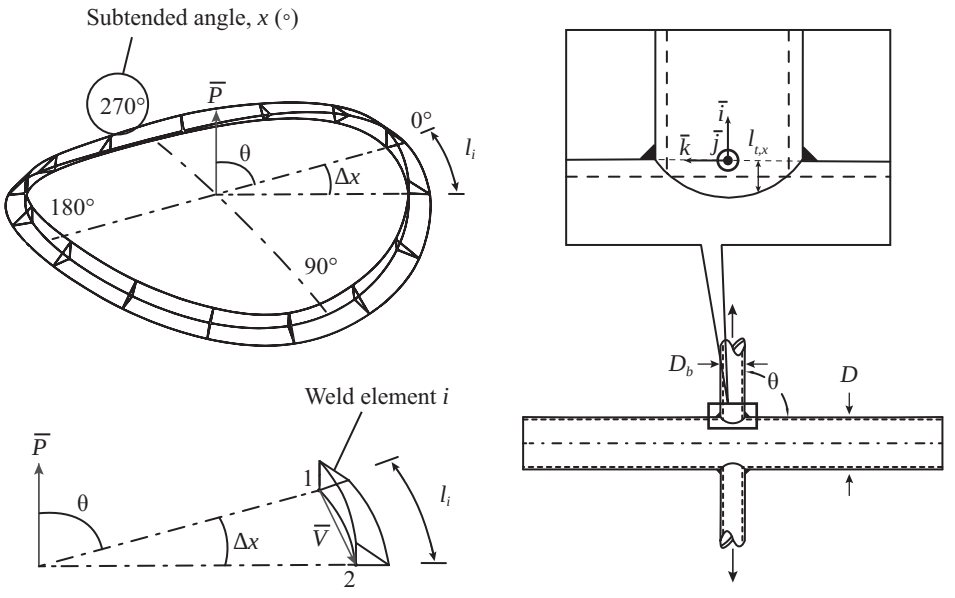

(a) vectors and notation *(b) coordinate system and additional notation*

Fig. 6. Calculation of the sinθ factor for a round-to-round HSS connection.

Table 2. Values of the $(1.0 + 0.50 \sin^{1.5}\theta)$ Factor (K_{CHS}) for an All-Around Fillet Weld in a Round-to-Round HSS Joint				
	Branch Inclination Angle, θ (°)			
Width Ratio, β	90°	80°	70°	60°
0.1	1.500	1.494	1.476	1.446
0.2	1.498	1.492	1.475	1.445
0.3	1.496	1.490	1.473	1.443
0.4	1.492	1.487	1.470	1.440
0.5	1.487	1.482	1.465	1.436
Note: The values of $(1.0 + 0.50 \sin^{1.5}\theta)$ assume a constant weld throat dimension, t_w.				

WELD EFFECTIVE LENGTHS FOR ROUND-TO-ROUND HSS CROSS-, T-, AND Y-JOINTS

Weld effective lengths are not necessary for round-to-round HSS joints (i.e., the total weld length can be used for l_e in Equation 2) when the sinθ factor is set to unity (i.e., θ taken as zero) in Equation 2 (Tousignant and Packer, 2019); however, a proposed approach for calculating weld effective lengths when the sinθ factor is used has not hitherto been addressed. Several options for the weld effective length, l_e, in round-to-round HSS cross-, T-, and Y-joints in the AISC *Specification* (AISC, 2016) are hence examined.

To evaluate the inherent safety level of each option, a reliability analysis, shown in Equation 12, is used to check that the target reliability index of $\beta^+ \geq 4.0$, as discussed in AISC *Specification* Commentary B3.1, is achieved (Ravindra and Galambos, 1978; Fisher et al., 1978); that is,

$$\phi = \phi_{\beta^+} \rho_R \exp(-\alpha \beta^+ V_R) \quad (12)$$

where α_R is the coefficient of separation, taken as 0.55 (Ravindra and Galambos, 1978); ρ_R is the bias coefficient for resistance; V_R is the associated coefficient of variation (COV) of ρ_R; and ϕ_{β^+} is an adjustment factor that modifies φ when β^+ is not equal to the safety index used for the evaluation of the load factors, which is normally 3.0 (Fisher et al., 1978). An equation developed by Franchuk et al. (2002) was used to calculate this factor:

$$\phi_{\beta^+} = 0.0062(\beta^+)^2 - 0.131\beta^+ + 1.338 \quad (13)$$

The bias coefficient for resistance, ρ_R, and its associated COV, V_R, are:

$$\rho_R = \rho_M \rho_G \rho_P \quad (14)$$

$$V_R = \sqrt{V_M^2 + V_G^2 + V_P^2} \quad (15)$$

where ρ_M is the mean ratio of actual-to-nominal ultimate tensile strength for the weld metal, ρ_G is the mean ratio of actual-to-nominal values for the weld throat area, and ρ_P is the mean ratio of FE-to-predicted joint strength. V_M, V_G, and V_P are the associated COVs of ρ_M, ρ_G, and ρ_P, respectively.

In the current study, ρ_M and V_M account for actual filler metal strength being greater than the filler metal classification strength in most applications. The values of ρ_M and V_M shown in Table 3 were determined from 708 coupon tests on filler metal(s) by Lesik and Kennedy (1990), Callele et al. (2009), and others (as summarized in Tousignant and Packer, 2017b). The factors ρ_G and V_G account for the typical increase in weld throat area due to weld face convexity (i.e., via an increase in t_w). The values of ρ_G and V_G shown in Table 3 were justified by Callele et al. (2009) for similar fillet-welded connections. The factors ρ_P and V_P relate the FE rupture strength of the joint to the nominal weld strength predicted using one of the design model options discussed in detail in the following. The factor ρ_P was taken as the average over all of the 256 FE weld-critical, round HSS cross-connection tests of the FE fillet weld fracture load, P_a, divided by R_n, with R_n calculated using Equations 1 and 2 (i.e., including the sinθ factor) with actual values of t_w, l_w, and F_{EXX} (i.e., the values used in the FE models) as opposed to nominal values (Tousignant and Packer, 2018).

If the total weld length is assumed to be effective (i.e., $l_e = l_w$ in Equation 1), the mean FE-to-predicted strength ratio for the 256 fillet-welded joints, ρ_P, is 0.93 with a COV, V_p, of 0.19 (see Table 3). The correlation of the predicted capacity, R_n, to the FE fracture load, P_a, is shown in Figure 7. With $l_e = l_w$ and $\phi = 0.75$ (AISC, 2016), $\beta^+ = 2.8$, which is much less than the target reliability index of $\beta^+ \geq 4.0$. Thus, a weld effective length rule is necessary for round-to-round HSS cross-connections in the AISC *Specification* (AISC, 2016).

Option 1

In clause 9.6.1.3(4), AWS D1.1 (AWS, 2015) implies a weld effective length, l_e, in axially loaded round-to-round HSS connections equal to $1/1.5$ of the total weld length under factored loads; that is,

Table 3. Reliability Analysis Parameters and Results for the AISC *Specification*				
		Option 1	**Option 2**	**Option 3**
l_e	l_w	**Equation 16**	**Equation 17**	**Equation 17**
K_{CHS}	**Table 2**	**Table 2**	**Table 2**	**Equation 18**
ϕ	0.75	0.75	0.75	0.75
ρ_M V_M	1.12 0.12	1.12 0.12	1.12 0.12	1.12 0.12
ρ_G V_G	1.03 0.10	1.03 0.10	1.03 0.10	1.03 0.10
ρ_P V_P	0.93 0.19	1.40 0.19	1.07 0.06	1.08 0.06
ρ_R V_R	1.08 0.25	1.62 0.25	1.24 0.17	1.24 0.17
ϕ_{β^+}	1.02	0.87	0.90	0.89
β^+	**2.8**	**4.6**	**4.2**	**4.2**

$$l_e = \frac{1}{1.5} l_w \tag{16}$$

This rule has been derived from numerical work on round-to-round HSS T-connections (Caulkins, 1968) and is based on potential weld unzipping caused by one part of the weld being much more highly loaded than another (Marshall, 1992).

If the AWS D1.1, clause 9.6.1.3(4) (AWS, 2015), expression is used for l_e (i.e., $l_e = {}^1\!/_{1.5}\, l_w$) in Equation 1, the mean FE-to-predicted strength ratio for the 256 fillet-welded joints, ρ_P, is 1.40 with a COV of $V_p = 0.19$ (see Table 3). The correlation of predicted capacity, R_n, to the FE fracture load, P_a, is then as shown in Figure 8, providing a reliability index of $\beta^+ = 4.6 \geq 4.0$ when $\phi = 0.75$ is used (AISC, 2016). This indicates that the AWS D1.1, clause 9.6.1.3(4) (AWS, 2015), expression for l_e shown in Equation 16 provides an acceptable level of safety; however, based on having $\rho_P = 1.40$, there is room to improve the l_e expression to increase the design efficiency (reduce the average ratio of P_a/R_n) of such joints. This is because Equation 16 was derived from the ratio of nominal-to-peak elastic strain in numerical tests (Calkins, 1968), and this has been shown to be conservative (Tousignant and Packer 2017b).

Option 2

Weld effective lengths in round-to-round HSS connections have also been shown to vary with D/t, β, and τ, though predominantly with D/t and β (Tousignant and Packer, 2018).

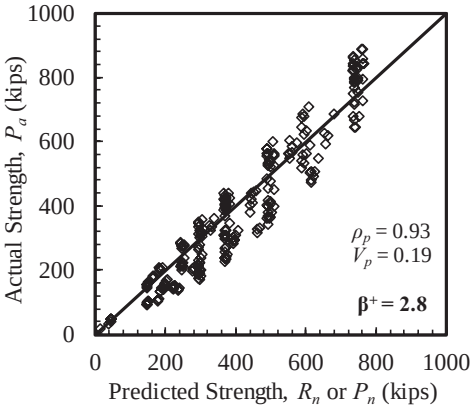

Fig. 7. Correlation of AISC Specification *provisions with FE results, assuming a weld effective length equal to the total weld length.*

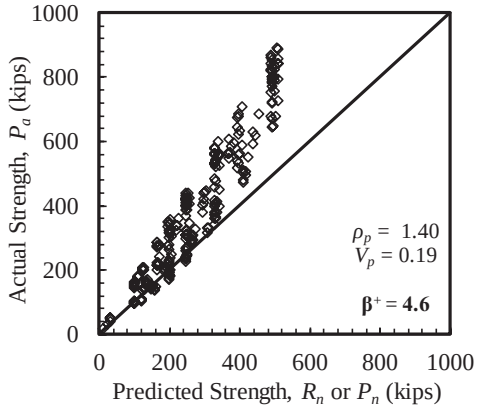

Fig. 8. Correlation of AISC Specification *provisions with FE results, assuming a weld effective length equal to ${}^1\!/_{1.5}$ of the total weld length (option 1).*

An accurate, yet simple, expression taking this into account is (Tousignant and Packer, 2018):

$$l_e = \frac{4}{\sqrt{2\beta(D/t)}} l_w \le l_w \quad (17)$$

If Equation 17 is used for l_e in Equation 1, the mean FE-to-predicted strength ratio for the 256 fillet-welded joints, ρ_P, is 1.07 with a COV of $V_p = 0.06$. The correlation of predicted capacity, R_n, to the FE fracture load, P_a, is then as shown in Figure 9.

Equation 17 provides $\beta^+ = 4.2 \ge 4.0$ when $\phi = 0.75$ is used (AISC, 2016), indicating that it also provides an acceptable level of safety. Notably, Equation 17 results in lower values of both ρ_P and V_p than the AWS D1.1, clause 9.6.1.3(4) (AWS, 2015), expression for l_e (Equation 16). It can therefore be concluded that Equation 17 results in greater efficiency of fillet welds in round-to-round HSS cross-, T-, and Y-connections than Equation 16 (i.e., it reduces the average ratio of P_a/R_n while still meeting the target reliability index). A side-by-side comparison of the reliability analysis parameters and results for these two options is given in Table 3.

Option 3

It may be argued that because the $(1.0 + 0.50 \sin^{1.5}\theta)$ factor already incorporates a simplification of a complex loading arrangement, a further simplification to option 2 is justified. Option 3 hence proposes that a designer take the loading angle [θ in the $(1.0 + 0.50 \sin^{1.5}\theta)$ factor] as equal to the branch inclination angle, to approximate the value of K_{CHS}; that is,

$$K_{CHS} = 1.0 + 0.5 \sin^{1.5}\theta \quad (18)$$

where θ is the acute angle between the branch and chord (in degrees), as opposed to the angle between the line of action of the applied force and the weld longitudinal axis.

K_{CHS} will hence become a simple function of the branch inclination angle, θ, and can therefore be calculated without relying upon a design aid. This recommended approach ranges from being marginally unconservative (by less than 1%, for connections with high values of θ and high values of β) to marginally conservative (by about 3%, for connections with low values of θ and high values of β) within the range $0.1 \le \beta \le 0.5$ and $60° \le \theta \le 90°$.

If Equation 17 is used to calculate l_e in Equation 1, with K_{CHS} now approximated using Equation 18 (as opposed to using the values in Table 2), the mean FE-to-predicted strength ratio for the 256 fillet-welded joints, ρ_P, is 1.08 with a COV of $V_p = 0.06$, and the correlation of predicted capacity, R_n, to the FE fracture load, P_a, is as shown in Figure 10. Based on these results, which are summarized in Table 3, using Equation 18 to approximate K_{CHS} provides a similar (acceptable) level of safety to Option 2 [i.e., $\beta^+ = 4.2 \ge 4.0$ when $\phi = 0.75$ is used (AISC, 2016)].

CONCLUSIONS

Based on a review of recent experimental and numerical research performed on fillet-welded, round-to-round HSS cross-connections, in which FE results have been analyzed in conjunction with allowing the $\sin\theta$ factor for fillet welds to the ends of round HSS in the AISC *Specification* (AISC, 2016), it has been found that:

- Application of the $\sin\theta$ factor to fillet-welded round-to-round HSS joints is nontrivial, if the true angle of loading to the weld axis is considered as it varies around the joint.

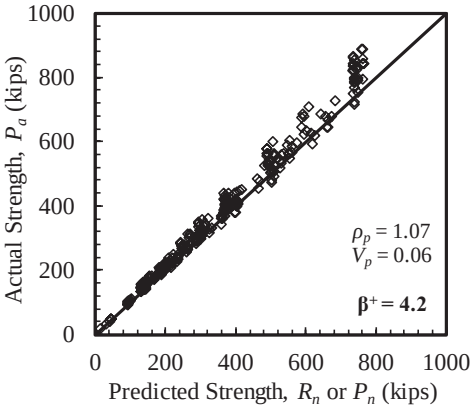

Fig. 9. Correlation of AISC Specification *provisions with FE results, assuming a weld effective length equal to Equation 17 (option 2).*

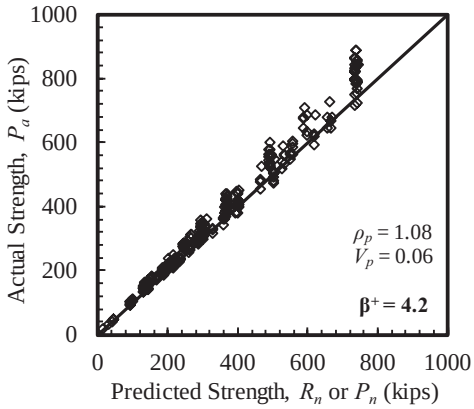

Fig. 10. Correlation of AISC Specification *provisions with FE results, assuming a weld effective length equal to Equation 17 and using Equation 18 to approximate* K_{CHS} *(option 3).*

A design aid as shown in Table 2 has been developed to simplify this procedure.

- Taking the total weld length as effective to design fillet welds in round-to-round HSS joints does not meet the target reliability index of $\beta^+ \geq 4.0$ (AISC *Specification* Commentary B3.1), when the sinθ factor is used to determine the available strength.
- The AWS D1.1, clause 9.6.1.3(4) (AWS, 2015), expression for the weld effective length in round-to-round HSS connections (i.e., $l_e = {}^1\!/_{1.5}\, l_w$) provides an acceptable level of safety ($\beta^+ = 4.6 \geq 4.0$) when the sinθ factor is used.
- Equation 17 for the weld effective length provides an acceptable level of safety ($\beta^+ = 4.2 \geq 4.0$) when the sinθ factor is used. This expression also provides lower values of actual-to-predicted nominal weld strength compared to the AWS D1.1, clause 9.6.1.3(4) (AWS, 2015) expression, allowing greater design efficiency to be achieved.
- Taking θ in the $(1.0 + 0.50 \sin^{1.5} \theta)$ factor as equal to the branch inclination angle (Equation 18), provides a similar (acceptable) level of safety ($\beta^+ = 4.2 \geq 4.0$) to the design aid (Table 2), when used in conjunction with Equation 17 to calculate the weld effective length.

RECOMMENDATION

It is recommended that the following design provisions be adopted for fillet welds in round-to-round HSS cross-, T-, and Y-connections:

$$R_n \text{ or } P_n = F_{nw} t_w l_e \tag{19}$$

where:

$$F_{nw} = 0.60 F_{EXX} K_{CHS} \tag{20}$$

where K_{CHS} is as shown in Table 2 for values of β and θ for a given joint, and

$$l_e = \frac{4}{\sqrt{2\beta(D/t)}} l_w \leq l_w \tag{21}$$

where l_w is determined from 3D solid models of intersecting cylinders or from the following simplified equation:

$$l_w = \pi D_b \frac{1 + 1/\sin\theta}{2} \tag{22}$$

The weld effective length given by Equation 21 is represented by two arcs of $l_e/2$ around the saddle regions, as illustrated in Figure 11.

Alternative Approach for Calculating K_{CHS}

As an alternative to using Table 2 to calculate K_{CHS} in Equation 20, it can instead be approximated with the following "modified sinθ factor":

$$K_{CHS} = 1.0 + 0.5 \sin^{1.5} \theta \tag{23}$$

where θ is the acute angle between the branch and chord (in degrees), rather than the angle between the line of action of the applied force and the weld longitudinal axis.

This recommendation is subject to the following limits of applicability:

Width ratio:	$0.1 \leq \beta \leq 0.5$
Branch angle:	$60° \leq \theta \leq 90°$
Chord wall slenderness:	$10 \leq D/t \leq 50$
Thickness ratio:	$0.20 \leq \tau \leq 1.00$
Weld throat:	t_w is constant around the joint

ACKNOWLEDGMENTS

Financial support for this project was provided by the Natural Sciences and Engineering Research Council of Canada (NSERC). Fabrication of test specimens was provided, as a gift in-kind, by Walters Inc., Hamilton, Ontario. Hollow structural sections used for experiments were donated by Atlas Tube, Harrow, Ontario.

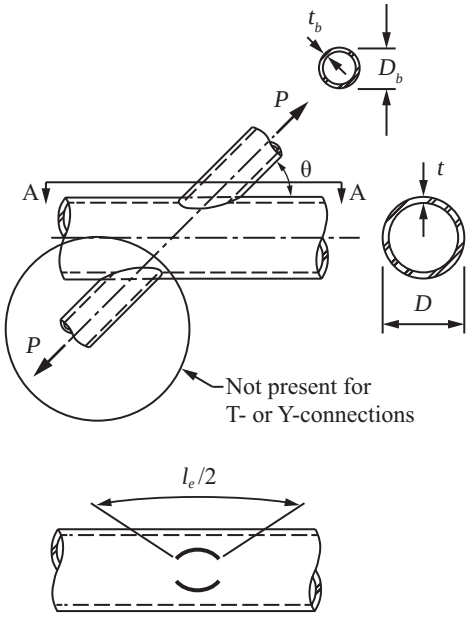

Fig. 11. Weld effective length for round-to-round HSS cross, T-, and Y-connections.

DESIGN EXAMPLE

Given:

A 60° cross-connection is formed between an HSS12.750×0.500 chord member and two HSS4.500×0.237 branch members in ASTM A500 Grade C material, as shown in Figure 12. The loads shown consist of 25% dead load and 75% live load. Determine a suitable fillet weld effective throat size around the branch members in this tubular connection, using matched electrodes with a specified ultimate strength of 70 ksi.

From the AISC *Manual* (AISC, 2017) Table 2-4, the material properties are as follows:

For all members
ASTM A500 Grade C
F_y, F_{yb} = 46 ksi
F_u, F_{ub} = 62 ksi

From the AISC *Manual* Table 1-13, the HSS geometric properties are as follows:

HSS12.750×0.500
D = 12.75 in.
t = 0.465 in.
A = 17.9 in.^{2}

HSS4.500×0.237
D_b = 4.50 in.
t_b = 0.220 in.
A_b = 2.96 in.^{2}

Solution:

Required strength (expressed as a force in the branch)

From ASCE/SEI 7 (ASCE, 2016) Chapter 2, the required strength is:

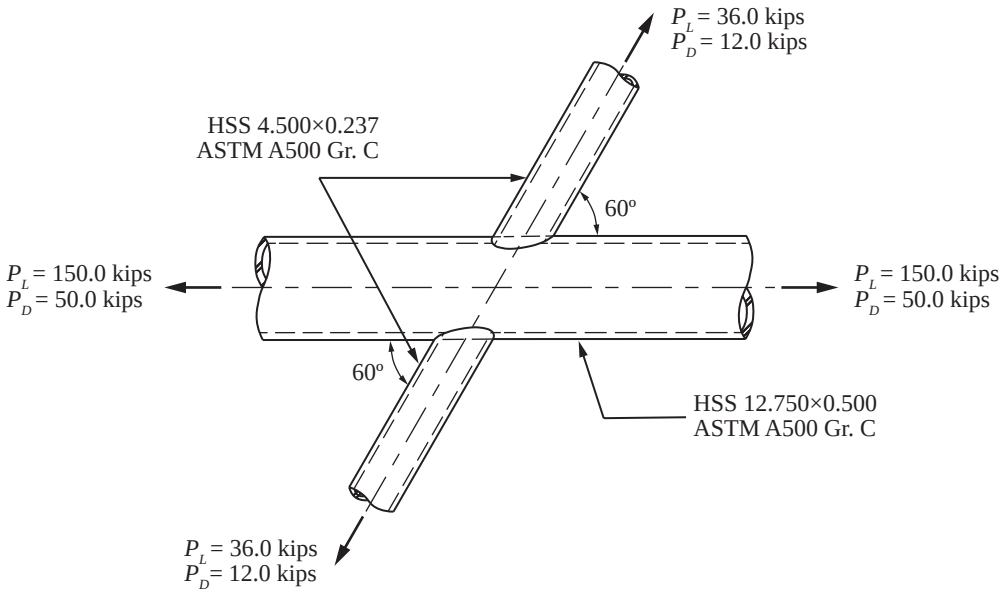

Fig. 12. Round-to-round HSS cross-connection subject to branch axial tension.

LRFD	ASD
$P_u = 1.2(12.0 \text{ kips}) + 1.6(36.0 \text{ kips})$ $= 72.0 \text{ kips}$	$P_a = 12.0 \text{ kips} + 36.0 \text{ kips}$ $= 48.0 \text{ kips}$

Note that this HSS connection satisfies the limits of applicability given by AISC *Specification* Table K3.1A (AISC, 2016); hence the connection strength can be determined from AISC *Specification* Table K3.1A for round HSS truss connections. Using AISC *Specification* Equations K3-1 and K3-3, the connection available axial strength (governed by the limit state of chord plastification) is $P_n = 82.5$ kips (LRFD) or $P_n/\Omega = 54.9$ kips (ASD), which exceeds the required strengths and is therefore acceptable. It is worthwhile noting that the required strength of 72.0 kips (LRFD) is only 59% of the available branch axial yield strength = $\phi A_b F_{yb} = 122.5$ kips.

Limits of applicability

A suitable fillet weld effective throat size around the branch members can be determined using Equations 19–21 only if the following limits of applicability are satisfied:

$0.1 \le \beta = 0.353 \le 0.5$ **o.k.**
$60° \le \theta = 60° \le 90°$ **o.k.**
$10 \le D/t = 27.4 \le 50$ **o.k.**
$0.20 \le \tau = 0.473 \le 1.00$ **o.k.**
t_w is constant around the joint **o.k.**

Because the limits of applicability are satisfied, Equations 19–21 can be used.

Required throat size

Determine the total weld length, l_w, using the approximation given by AWS D1.1, clause 9.5.4 (AWS, 2015):

$$l_w = \pi D_b \frac{1 + 1/\sin\theta}{2} \tag{22}$$
$$= \pi(4.500 \text{ in.}) \frac{1 + 1/\sin 60°}{2}$$
$$= 15.2 \text{ in.}$$

Calculate the weld effective length, l_e, using the previous results:

$$l_e = \frac{4}{\sqrt{2\beta(D/t)}} l_w \le l_w \tag{21}$$
$$= \frac{4}{\sqrt{2(0.353)(27.4)}}(15.2 \text{ in.}) \le 15.2 \text{ in.}$$
$$= 13.8 \text{ in.} \le 15.2 \text{ in.}$$
$$= 13.8 \text{ in.}$$

Account for the directional strength increase for fillet welds in round-to-round HSS connections using the factor K_{CHS}. For the connection considered, with $\beta = 0.353$ and $\theta = 60°$, K_{CHS} can be found by linearly interpolating between $\beta = 0.300$ and $\beta = 0.400$ in Table 2 for $\theta = 60°$.

For $\beta = 0.300$ and $\theta = 60°$, $K_{CHS} = 1.443$, and for $\beta = 0.400$ and $\theta = 60°$, $K_{CHS} = 1.440$. Hence, for $\beta = 0.353$ and $\theta = 60°$:

$$K_{CHS} = 1.440 + \frac{0.400 - 0.353}{0.400 - 0.300}(1.443 - 1.440)$$
$$= 1.441$$

Alternatively, K_{CHS} can be approximated using Equation 23, as follows:

$$K_{CHS} = 1.0 + 0.5\sin^{1.5}\theta \tag{23}$$
$$= 1.0 + 0.50\sin^{1.5}(60°)$$
$$= 1.403$$

The remainder of the design example is completed using $K_{CHS} = 1.441$.

The nominal stress of the weld metal, F_{nw}, can now be determined using Equation 20:

$$F_{nw} = 0.60F_{EXX}K_{CHS} \tag{20}$$
$$= 0.60(70 \text{ ksi})(1.441)$$
$$= 60.5 \text{ ksi}$$

Applying the resistance factor of $\phi = 0.75$ to fillet welds designed using the LRFD method, or the safety factor of $\Omega = 2.00$ to fillet welds designed using the ASD method, an expression for the available weld strength, ϕP_n or P_n/Ω, can be written (AISC, 2016).

LRFD	ASD
$\phi P_n = 0.75F_{nw}t_w l_e$	$\frac{P_n}{\Omega} \geq \frac{F_{nw}t_w l_e}{2.00}$

Set the expression for the available weld strength equal to (or greater than) the required strength to determine the required weld throat size, t_w, to transmit the calculated forces.

LRFD	ASD
$0.75F_{nw}t_w l_e \geq P_u$ $t_w \geq \frac{P_u}{0.75F_{nw}l_e}$ $t_w \geq \frac{72.0 \text{ kips}}{0.75(60.5 \text{ ksi})(13.8 \text{ in.})}$ $t_w \geq 0.115 \text{ in.}$	$\frac{F_{nw}t_w l_e}{2.00} \geq P_a$ $t_w \geq \frac{2.00P_a}{F_{nw}l_e}$ $t_w \geq \frac{2.00(48.0 \text{ kips})}{(60.5 \text{ ksi})(13.8 \text{ in.})}$ $t_w \geq 0.115 \text{ in.}$

Rounding up to the nearest sixteenth of an inch, $t_w = 0.125$ in. would satisfy the strength requirements of this connection.

It should be noted that the limitations of AISC *Specification* Section J2.2b also apply, and the weld leg size, L, must not be less than the size given in AISC *Specification* Table J2.4. Therefore, for $t_b = 0.220$ in., corresponding to the material thickness of the thinner part joined, L must be greater than or equal to 0.125 in. Because L will never be less than t_w (= 0.125 in.) for a fillet weld, this requirement is satisfied.

Hence, $t_w = 0.125$ in., or ⅛ in., is a suitable fillet weld throat size.

SYMBOLS AND ACRONYMS

A	Cross-sectional area of round HSS chord member, in.^{2}
A_b	Cross-sectional area of round HSS branch member, in.^{2}
AISC	American Institute of Steel Construction
AWS	American Welding Society
COV	Coefficient of variation
D	Outside diameter of round HSS chord member, in.
D_b	Outside diameter of round HSS branch member, in.
F_{EXX}	Filler metal classification strength, ksi
F_{nw}	Nominal stress of weld metal, ksi
F_u	Specified minimum tensile strength of round HSS chord member, ksi
F_{ub}	Specified minimum tensile strength of round HSS branch member, ksi
F_y	Specified minimum yield stress of round HSS chord member, ksi
F_{yb}	Specified minimum yield stress of round HSS branch member, ksi
K_a	Weld length factor according to AWS D1.1 (AWS, 2015)
K_{CHS}	Value of $(1.0 + 0.50 \sin^{1.5} \theta)$ for a round-to-round HSS joint
L	Weld leg size, in.
LRFD	Load and resistance factor design
P	Axial force, kips
P_D	Axial force due to dead load, kips
P_L	Axial force due to live load, kips
P_a	Actual weld fracture load, kips; required axial strength in tension or compression, using ASD load combinations, kips
P_n	Nominal axial strength, kips
P_u	Required axial strength in tension or compression, using LRFD load combinations, kips
$\overline{P}$	Vector defining the direction of the applied force
R_n	Nominal strength, kips
V_G	Coefficient of variation of ρ_G
V_M	Coefficient of variation of ρM
V_P	Coefficient of variation of ρP
V_R	Coefficient of variation of ρR
$\overline{V}$	Vector approximation to the weld longitudinal axis between points at x and $x+\Delta x$
l_e	Weld effective length, in.
$l_{t,x}$	"Template length" at x, parallel to branch, in.
$l_{t,x}+\Delta x$	"Template length" at $x + \Delta x$, parallel to branch, in.
l_i	Length of weld element i, in.
l_w	Total length of weld, in.
r	Outside radius of round HSS chord member, in.
r_b	Outside radius of round HSS branch member, in.
t	Wall thickness of round HSS chord member, in.
t_b	Wall thickness of round HSS branch member, in.
t_w	Weld effective throat, in.
x	Subtended angle around the branch, measured clockwise from the heel, degrees
α	Coefficient of separation, taken as 0.55
β	Width ratio; the ratio of branch diameter to chord diameter for round HSS
β^+	Reliability index
Ω	Safety factor
ϕ	Resistance factor
$\phi_{\beta+}$	Adjustment factor for ϕ
τ	Branch-to-chord thickness ratio
θ	Acute angle between the branch and chord, degrees; angle between the line of action of the applied force and the weld longitudinal axis, degrees
θ_i	Angle between the line of action of the applied force and the weld longitudinal axis for weld element i, degrees
ρ_G	Mean ratio of actual-to-nominal values for the weld throat area
ρ_M	Mean ratio of actual-to-nominal ultimate tensile strength for the weld metal
ρ_P	Mean ratio of FE-to-predicted joint strength
ρ_R	Bias coefficient for resistance

REFERENCES

AISC (2016), *Specification for Structural Steel Buildings*, ANSI/AISC 360–16, American Institute of Steel Construction, Chicago, Ill.

AISC (2017), *Steel Construction Manual*, 15th Ed., American Institute of Steel Construction, Chicago, Ill.

ASCE (2016), *Minimum Design Loads and Associated Criteria for Buildings and Other Structures*, ASCE/SEI 7–16, American Society of Civil Engineers, Reston, Va.

ASTM (2018), *Standard Specification for Cold-Formed Welded and Seamless Carbon Steel Structural Tubing in Rounds and Shapes*, ASTM A500/A500M-18, ASTM International, West Conshohocken, Pa.

AWS (2015), *Structural Welding Code—Steel,* AWS D1.1/D1.1M:2015, American Welding Society, Miami, Fla.

Callele, L.J., Driver, R.G., and Grondin, G.Y. (2009), "Design and Behaviour of Multi-Orientation Fillet Weld Connections," *Engineering Journal*, AISC, Vol. 46, No. 4, pp. 257–272.

Caulkins, D.W. (1968), *Parameter Study for FRAMETI Elastic Stress in Tubular Joints*, CDG Report 15, Shell Oil Company, Houston, Tex.

Fisher, J.W., Galambos, T.V., Kulak, G.L., and Ravindra, M.K. (1978), "Load and Resistance Factor Design Criteria for Connectors," *Journal of the Structural Division,* ASCE, Vol. 104, No. 9, pp. 1,427–1,441.

Franchuk, C.R., Driver, R.G., and Grondin, G.Y. (2002), "Block Shear Failure of Coped Steel Beams," *Proceedings of the Annual Conference of the Canadian Society for Civil Engineering*, Montréal, QC, pp. 1,000–1,009.

Lesik, D.F. and Kennedy, D.J. (1990), "Ultimate Strength of Fillet Welded Connections Loaded in Plane," *Canadian Journal of Civil Engineering*, CSCE, Vol. 17, No. 1, pp. 55–67.

Marshall, P.W. (1992), *Design of Welded Tubular Connections—Basis and Use of AWS Code Provisions*, Elsevier, Amsterdam, The Netherlands.

McFadden, M.R. and Packer, J.A. (2014), "Effective Weld Properties for Hollow Structural Section T-Connections under Branch in-Plane Bending," *Engineering Journal*, AISC, Vol. 51, No. 4, pp. 247–266.

Packer, J.A., Sun, M. and Tousignant, K. (2016), "Experimental Evaluation of Design Procedures for Fillet Welds to Hollow Structural Sections," *Journal of Structural Engineering*, ASCE, Vol. 142, No. 5, pp. 04016007:1–04016007:12.

Ravindra, M.K. and Galambos, T.V. (1978), "Load and Resistance Factor Design Criteria for Connectors," *Journal of the Structural Division*, ASCE, Vol. 104, No. 9, pp. 1,337–1,353.

Tousignant, K. and Packer, J.A. (2015), "Weld Effective Lengths for Rectangular HSS Overlapped K-Connections," *Engineering Journal,* AISC, Vol. 52, No. 4, pp. 259–281.

Tousignant, K. and Packer, J.A. (2016), "Experimental Evaluation of the Directional Strength-Enhancement Factor for Fillet Welds to CHS," *Proceedings of the 8th International Workshop on Connections in Steel Structures*, Boston, Mass., pp. 295–304.

Tousignant, K. and Packer, J.A. (2017a), "Numerical Investigation of Fillet Welds in HSS-to-Rigid End-Plate Connections," *Journal of Structural Engineering*, ASCE, Vol. 143, No. 12, pp. 04017165:1–04017165:16.

Tousignant, K. and Packer, J.A. (2017b), "Fillet Weld Effective Lengths in CHS X-Connections. I: Experimentation," *Journal of Constructional Steel Research*, Vol. 138, pp. 420–431.

Tousignant, K. and Packer, J.A. (2018), "Fillet Weld Effective Lengths in CHS X-Connections. II: Finite Element Modelling, Parametric Study and Design," *Journal of Constructional Steel Research*, Vol. 141, pp. 77–90.

Tousignant, K. and Packer, J.A. (2019), "Fillet Welds around Circular Hollow Sections," *Welding in the World*, IIW, Vol. 63, pp. 421–433.

Guide for Authors

Scope

Engineering Journal is dedicated to the improvement and advancement of steel construction. Its pages are open to all who wish to report on new developments or techniques in steel design, research, the design and/or construction of new projects, steel fabrication methods, or new products of significance to the uses of steel in construction. Only original papers should be submitted.

General

Papers intended for publication should be submitted by email Margaret Matthew, editor, at **matthew@aisc.org**.

The articles published in the *Engineering Journal* undergo peer review before publication for (1) originality of contribution; (2) technical value to the steel construction community; (3) proper credit to others working in the same area; (4) prior publication of the material; and (5) justification of the conclusion based on the report.

All papers within the scope outlined above will be reviewed by engineers selected from among AISC, industry, design firms, and universities. The standard review process includes outside review by an average of three reviewers, who are experts in their respective technical area, and volunteers in the program. Papers not accepted will not be returned to the author. Published papers become the property of the American Institute of Steel Construction and are protected by appropriate copyrights. No proofs will be sent to authors. Each author receives three copies of the issue in which his contribution appears.

Manuscripts

Manuscripts must be provided in Microsoft Word format. Include a PDF with your submittal so we may verify fonts, equations and figures. View our complete author guidelines at **aisc.org/ej**.

Smarter. Stronger. Steel.

American Institute of Steel Construction
130 E Randolph St, Ste 2000, Chicago, IL 60601
312.670.2400 | aisc.org/ej